ACOUSTIC TRANSDUCTION – MATERIALS AND DEVICES

Period 1 January 1998 to 31 December 1998

Annual Report

VOLUME VI

OFFICE OF NAVAL RESEARCH
Contract No: N00014-96-1-1173

Kenji Uchino

PENNSTATE

1855

THE MATERIALS RESEARCH LABORATORY
UNIVERSITY PARK, PA

REPORT DOCUMENTATION PAGE

Form Approved
OMB No. 0704-0188

1. AGENCY USE ONLY (Leave blank)	2. REPORT DATE	3. REPORT TYPE AND DATES COVERED
	04/05/99	ANNUAL REPORT 01/01/98-12/31/98

4. TITLE AND SUBTITLE

ACOUSTIC TRANSDUCTION -- MATERIALS AND DEVICES

5. FUNDING NUMBERS

ONR CONTRACT NO:
N00014-96-1-11173

6. AUTHOR(S)

KENJI UCHINO

7. PERFORMING ORGANIZATION NAME(S) AND ADDRESS(ES)

Materials Research Laboratory
The Pennsylvania State University
University Park PA 16802

8. PERFORMING ORGANIZATION REPORT NUMBER

9. SPONSORING/MONITORING AGENCY NAME(S) AND ADDRESS(ES)

Office of Naval Research
ONR 321SS
Ballston Centre Tower One
800 N Quincy Street
Arlington VA 22217-5660

Office of Naval Research
Regional Office Chicago
536 S Clark Str., RM 208
Chicago IL 60605-1588

10. SPONSORING/MONITORING AGENCY REPORT NUMBER

11. SUPPLEMENTARY NOTES

12a. DISTRIBUTION/AVAILABILITY STATEMENT

12b. DISTRIBUTION CODE

13. ABSTRACT *(Maximum 200 words)*

14. SUBJECT TERMS

15. NUMBER OF PAGES

16. PRICE CODE

17. SECURITY CLASSIFICATION OF REPORT	18. SECURITY CLASSIFICATION OF THIS PAGE	19. SECURITY CLASSIFICATION OF ABSTRACT	20. LIMITATION OF ABSTRACT

ABSTRACT

This report documents work performed over the period 1 January 1998 to 31 December 1998 on a MURI under the Office of Naval Research Contract N00014-96-1-1173. The topic "Acoustic Transduction Materials and Devices" brings together groups in the Materials Research Laboratory (MRL), the Applied Research Laboratory (ARL), and the Center for Acoustics and Vibrations (CAV) at Penn State.

Research on the program is adequately represented in the 80 technical appendices.

Outstanding accomplishments include:

Exploration of several new relaxor ferroelectric perovskite solid solution with morphotropic phase boundaries. New evidence of the onset of nonlinearity in soft donor doped PZTs at surprisingly low (1V/cm) fields. Confirmation of the relaxor phase induced by electron irradiation in PVDF:TrFE copolymers, and a processing method which permits very high (4%) electrostrictive strain in the transverse direction, vital for the practical use in actuator systems. In composite transducer, "first fruits" of the cooperative program are cymbal arrays which form most effective acoustic projectors, and a new "dog bone" design which permits deeper submergence for the cymbal. Agile transducers, the 3-D acoustic intensity probe and high force high strain torsional and step and repeat systems continue to make excellent progress. In actuator studies true acoustic emission is proving to be an excellent tool in reliability studies and a new design of small-scale (mini) piezoelectric motor shows outstanding performance. Thick thin film studies and are now "gearing up" for the development of the mini tonpilz arrays. New combinations of ultrasonic and resonance methods appear to offer unique capability for complete characterization of ferroelectric piezoelectric materials.

The mode of presentation of the report emphasis the outstanding progress made in published research. It is important to also document that the slower and more painstaking development of practical transducer systems in the cymbal and mini tonpilz arrays is progressing very favorably.

APPENDICES

VOLUME I

GENERAL SUMMARY PAPERS

1. Cross, L.E., "Recent Developments in Piezoelectric Ferroelectric Materials and Composites," Proceedings of the 4th European Conference on Smart Structures and Materials in Conjunction with the 2nd International Conference on Micromechanics, Intelligent Materials and Robotics, Harrogate, UK (6-8 July 1998).
2. Newnham R.E., "Functional Composites for Sensors and Actuators," Chapter in *The Era of Materials*, edited by S. Majumdar, R. Tressler, and E. Miller, 259-275, Pennsylvania Academy of Science (1998).
3. Uchino, K., "Piezoelectric Ultrasonic Motors: Overview," Smart Mater. Struct. **7**, 273-285 (1998).
4. Newnham, R.E., "Phase Transformations in Smart Materials," Acta Cryst. A**54**, 729-737 (1998).

2.0 MATERIALS STUDIES

2.1 Polycrystal Perovskite Ceramics

5. Liu, S.F., I.R. Abothu, S. Komarneni, P. Poosanaas, D.S. Paik, Y. Ito, and K. Uchino, "PLZT Ceramics from Conventional and Microwave Hydrothermal Powders," Proceedings in Asian Meeting on Ferroelectrics (AMF2), Singapore (December 8-11, 1998).
6. Abothu, I.R., P. Poosanaas, S. Komarneni, Y. Ito, and K. Uchino, "Nanocomposite Versus Monophasic Sol-Gel Processing of PLZT Ceramics," Proceedings in Asian Meeting on Ferroelectrics (AMF2), Singapore (December 8-11, 1998).
7. Kim, J.S., Y.H. Chen, and K. Uchino, "Dielectric and Piezoelectric Properties of Fe_2O_3-Doped 0.57PSN-0.43PT Ceramics, "J. Korean Phys. Soc. **32** [2], S1248-1250 (1998).
8. Alberta, E.F. and A.S. Bhalla, "Electrical Property Diagram and Morphotropic Phase Boundary in the $Pb(In_{1/2}Ta_{1/2})O_3$-$PbTiO_3$ Solid Solution System," Ferroelectric Letters (1998). [accepted]
9. Meng, J.F., Z-Y. Cheng, B.K. Rai, R.S. Katiyar, E. Alberta, R. Guo, and A.S. Bhalla, "Photoluminescence in $PbMg_{1/3}Nb_{2/3}O_3$-$PbIn_{1/2}Nb_{1/2}O_3$ Systems," J. Mater. Res. **13** (7), 1861 (1998).
10. Alberta, E.F. and A.S. Bhalla, "Investigation of the Lead Indium Niobate-Lead Magnesium Niobate Solid Solution," Materials Letters (1998). [accepted]
11. Alberta, E.F., A.S. Bhalla, and T. Takenaka, "Large Hydrostatic Piezoelectric Constant and Temperature Dependence of the Piezoelectric Properties of $Bi(NiTi)_{1/2}O_3$:$PbTiO_3$ Ceramics," Ferroelectrics Letters (1998). [accepted]
12. Zhang, Q.M. and J. Zhao, "Electromechanical Properties of Lead Zirconate Titanate Piezoceramics Under the Influence of Mechancial Stress, IEEE Trans. UFFFC (acccepted).
13. Kugel, V.D. and L.E. Cross, "Behavior of soft Piezoelectric Ceramics under High Sinusoidal Electric Fields," J. Appl. Phys. **84** (5), 2815-2830 (1998).

VOLUME II

2.0 MATERIALS STUDIES

2.1 Polycrystal Perovskite Ceramics (continued)

14. Du, X-H., Q.M. Wang, U. Belegundu, and K. Uchino, "Piezoelectric Property Enhancement in Polycrystalline Lead Zirconate Titanate by Changing Cutting Angle," J. Ceram. Soc. Jpn. (1999). [accepted]
15. Mueller, V. and Q.M. Zhang, "Nonlinearity and Scaling Behavior in Donor Doped Lead Zirconate Titanate Piezoceramic," Appl. Phys. Lett. **72**, 2692 (1998).
16. Uchino, K and H. Aburatani, "Field Induced Acoustic Emission in Ferroelectric Ceramics," Proc. IEEE Ultrasonic Symp., Sendai, Japan (October 1998). [in press]
17. Newnham, R.E. and S. Trolier-McKinstry, "Size Effects in Ferroics" Integrated Ferroelectrics **20**, 1-13, Gordon & Breach Science Publishers (March 1998).

2.2 Relaxor Ferroelectric Single Crystal Systems

18. Uchino, K., "High Electromechanical Coupling Piezoelectrics: Relaxor and Normal Ferroelectric Solid Solutions," Solid State Ionics 108, 43-52 (1998).
19. Wada, S. S.E. Park, L.E. Cross, and T.R. Shrout, "Domain Configuration and Ferroelectric Related Properties of Relaxor Based Single Crystals," J. Korean Phys. Soc. **32**, S1290-S1293 (1998).
20. Belegundu, U., X. H. Du, and K. Uchino, "In-Situ Observation of Domain Orientation in $Pb(Zn_{1/3}Nb_{2/3})O_3$-$PbTiO_3$ Single Crystals," Proc. 5th Intl. Symp. Ferroic Domains and Mesoscopic Structures, University Park, PA (April 1998).
21. Du, X.H., J. Zheng, U. Belegundu, and K. Uchino, "Crystal Orientation Dependence of Piezoelectric Properties of Lead Zirconate Titanate Near the Morphotropic Phase Boundary," J. Appl. Phys. Ltrs. **72** (19), 2421-2423 (1998).
22. Rehrig, P.W., S.-E. Park, S. Trolier-McKinstry, G.L. Messing, B. Jones, and T.R. Shrout, "Piezoelectric Properties of Zirconium-Doped Barium Titanate Single Crystals Grown by Templated Grain Growth," submitted to J. Appl. Phys.
23. Du, X., Q.M. Wang, U. Belegundu, A. Bhalla, and K. Uchino, "Crystal Orientation Dependence of Piezoelectric Properties of Single Crystal Barium Titanate," Mat. Ltr. (1999) [accepted].
24. Guo, R., H.T. Evans, Jr., and A.S. Bhalla, "Crystal Structure Analysis and Polarization Mechanisms of Ferroelectric Tetragonal Tungsten Bronze Lead Barium Niobate," Ferroelectrics **206/207**, 123-132 (1998).

2.3 New High Strain Polymer Materials

25. Zhao, X., V. Bharti, Q.M. Zhang, T. Ramotowski, F. Tito, and R. Ting, "Electromechanical Properties of Electrostrictive P(VDF-TrFE) Copolymer," Appl. Phys. Ltrs. **73**, 2054 (1998).
26. Bharti, V., G. Shanthi, H. Xu, Q.M. Zhang, and K. Liang, "Evolution of Transitional Behavior and Structure of Electron Irradiated Poly(vinylidene fluoride-trifluorethylene) Copolymer Films," Appl. Phys. Ltrs. [accepted].
27. Cheng, Z.-Y., V. Bharti, T.B. Xu, S. Wang, and Q.M. Zhang, "Transverse Strain Responses in Electrostrictive Poly (vinylidene fluoride-trifluoroethylene) Films and Development of a Dilatometer for the Measurement," J. Appl. Phys. [accepted]

VOLUME III

2.0 MATERIALS STUDIES

2.3 New High Strain Polymer Materials (continued)

28. Bharti, V., X.Z. Zhao, Q.M. Zhang, T. Ramotowaski, F. Tito, and R. Ting, "Ultrahigh Field Induced Strain and Polarized Response in Electron Irradiated Poly(vinylidene fluoride-trifluoroethylene) Copolymer," Mat. Res. Innovat. **2**, 57-63 (1998).
29. Su, J., P. Moses, and Q.M. Zhang, "A Bimorph Based Dilatometer for Field Induced Strain Measurement in Soft and Thin Free Standing Polymer Films," Rev. Sci. Instruments **69** (6), 2480 (1998).

3.0 TRANSDUCER STUDIES

3.1 Composite Structures

30. Hughes, W.J., "Transducers, Underwater Acoustic," Encyclopedia of Applied Physics, Vol. 22, 67 (1998).
31. Tressler, J.F., W.J. Hughes, W. Cao, K. Uchino, and R.E. Newnham, "Capped Ceramic Underwater Sound Projector."
32. Zhang, J., W.J. Hughes, A.C. Hladky-Hennion, and R.E. Newnham, "Concave Cymbal Transducers."
33. Wang, Q.M., X.-H. Du, B. Xu, and L.E. Cross, "Theoretical Analysis of the Sensor Effect of Cantilever Piezoelectric Benders," J. Appl. Phys. **85** (3), 1702-1712 (1998).
34. Fernandez, J.F., A. Dogan, J.T. Fielding, K. Uchino, and R.E. Newnham, "Tailoring the Performance of Ceramic-Metal Piezocomposite Actuators, 'Cymbals'," Sensors and Actuator A**65**, 228-237 (1998).
35. Wang, Q.M. and L.E. Cross, "A Piezoelectric Pseudoshear Multilayer Actuator," Appl. Phys. Ltrs. **72** (18), 2238 (1998).
36. Geng, X. and Q.M. Zhang, "Resonance Modes and Losses in 1-3 Composites for Ultrasonic Transducer Applications," J. Appl. Phys. **85** (3), 1342 (1999).

3.2 Frequency Agile Transducers

37. Hebert, C.A. and G. A. Lesieutre, "Flexural Piezoelectric Transducers with Frequency Agility Obtained Via Membrane Loads," J. Intel. Mat. Sys. & Str. (1998). [accepted].
38. Davis, C.L. and G.A. Lesieutre, "An Actively Tuned Solid State Vibration Absorber Using Capacitive Shunting of Piezoelectric Stiffness," J. Sound & Vibration (1998). [accepted]
39. Bernard, J., G.A. Lesieutre, and G.H. Koopmann, "Active Broadband Force Isolation using a Flexural Piezoelectric Inertial Actuator," J. Sound & Vibration (1999). [submitted]

VOLUME IV

3.0 TRANSDUCER STUDIES

3.3 3-D Acoustic Intensity Probes (continued)

40. Lauchle, G.C. and A.R. Jones, "Unsteady Lift Force on a Towed Sphere," J. Fluids and Structures **112** (1998).
41. Lauchle, G.C., A.R. Jones, J.J. Dreyer, and J. Wang, "Flow-Induced Lift Forces on a Towed Sphere," Proc. Of ASME Noise Control and Acoustics Division ASME 1998, **NCA-28**, 103-111 (1998).
42. Brungart, T.A. G.C. Lauchle, S. Deutsch, and E. Riggs, "Outer-Flow Effects on Turbulent Boundary Layer Wall Pressure Fluctuations," J. Acoust. Soc. Am. **105** (4) (April 1999).
43. Brungart, T.A., G.C. Lauchle, and R.K. Ramanujam, "Installation Effects of Fan Acoustic and Aerodynamic Performance," Noise Control Eng. J. **47** (January/February 1999).

4.0 ACTUATOR STUDIES

4.1 Materials : Designs : Reliability

44. Uchino, K., "New Trend in Ceramic Actuators," Proc. 6th Intl. Aerospace Symp. '98, Nagoya, Japan, p. S1-2, 1-10 (July 14-15, 1998).
45. Uchino, K., "Materials Issues in Design and Performance of Piezoelectric Actuators: An Overview," Acta. Mater. 46 (11), 3745-3753 (1998).
46. Yao, K., W. Zhu, K. Uchino, Z. Zhang, and L.C. Lim, "Design and Fabrication of a High Performance Multilayer Piezoelectric Actuator with Bending Deformation."
47. Aburatani, H. and K. Uchino, "Acoustic Emission in Damaged Ferroelectric Lead Zirconate Titanate Ceramics," Jpn. J. Appl. Phys. **37**, L553-L555 (1998).
48. Atherton, P.D. and K. Uchino, "New Developments in Piezo Motors and Mechanisms," Proc. 6th Intl. Conf. On New Actuators (Actuator 98) , Bremen, Germany, p. 164-169 (June 17-19, 1998).
49. Uchino, K. and B. Koc, "Compact Piezoelectric Ultrasonic Motors," 2nd Asian Meeting on Ferroelectrics (AMF-2), Singapore (December 7-11, 1998).
50. Koc, B., Y. Xu, and K. Uchino, "Ceramic/Metal Composite Piezoelectric Motors," IEEE Ultrasonic Symposium, Sendai, Japan (October 1998).
51. Koc, B., Y. Xu, and K. Uchino, "Roto-Linear Ultrasonic Motors," Proc. 6th Intl. Conf. On New Actuators (Actuator 98), Bremen, Germany, p. 349-352 (June 17-19, 1998).
52. Koc, B., A. Dogan, Y. Xu, R.E. Newnham, and K. Uchino, "An Ultrasonic Motor Using a Metal-Ceramic Composite Actuator Generating Torsional Displacement," Jpn. J. Appl. Phys. **37**, 5659-5662 (1998).

4.2 Photostrictive Actuators

53. Poosanaas, P. and K. Uchino, "Photostrictive Effect in Lanthanum-Modified Lead Zirconate Titanate Ceramics Near The Morphotropic Phase Boundary," J. Mat. Chem. & Phys. (October 1998). [submitted]
54. Uchino, K. and P. Poosanaas, "Photostriction in PLZT and Its Applications," Proc. CIMTEC '98, Florence, Italy (June 14-19, 1998).

VOLUME V

4.0 ACTUATOR STUDIES

4.3 Torsional and High Force Actuators (continued)

55. Glazounov, A.E., Q.M. Zhang, and C. Kim, "Torsional Actuator Based on Mechanically Amplified Shear Piezoelectric Response," Sensors and Actuators (1998). [submitted]
56. Frank, J., G.H. Koopmann, W. Chen, and G.A. Lesieutre, "Design and Performance of a High Force Piezoelectric Inchworm Motor."

5.0 MODELING and CHARACTERIZATION

5.1 Finite Element and Other Methods

57. Qi, W. and W. Cao, "Finite Element and Experimental Study of Composite and 1-D Array Transducers," SPIE **3341** (1998).
58. Wang, H., W. Jiang, and W. Cao, "Characterization of Lead Zirconate Titanate Piezoceramic Using High Frequency Ultrasonic Spectroscopy," J. Appl. Phys. (1998). [accepted]
59. Zhu, S.N., B. Jiang, and W. Cao, "Characterization of Piezoelectric Materials Using Ultrasonic and Resonant Techniques," Proceedings of SPIE Imaging '98, **3341**, 154-162 (1998).
60. Cao, W., "Virtual Design of Medical Transducers," Proceedings of SPIE Imaging '98, **3341**, 56-63 (1998).
61. Cao, W., "Elastic Property Characterization in Thin Samples of Sub-Wavelenght in Thickness," Ferroelectrics **206/207**, 355-363 (1998).
62. Cao, W., S.N. Zhu, and B. Jiang, "Analysis of Shear Modes in A Piezoelectric Resonantor," J. Appl. Phys. **83**, 4415-4420 (1998).

5.2 Relaxor Ferroelectrics

63. Giniewicz, J.R., A.S. Bhalla, and L.E. Cross, "Variable Structural Ordering in Lead Scandium Tantalate-Lead Titanate Materials," Ferroelectrics **211**, 281-297 (1998).
64. Pan, X., W.D. Kaplan, M. Rühle, and R.E. Newnham, "Quantitative Comparison of Transmission Electron Microscopy Techniques for the Study of Localized Ordering on a Nanoscale," J. Am. Ceram. Soc. **81** (3), 597-605 (1998).
65. Zhao, J., A.E. Glazounov, and Q.M. Zhang, "Change in Electromechanical Properties of 0.9PMN:0.1PT Relaxor Ferroelectric Induced by Uniaxial Compressive Stress Directed Perpendicular to the Electric Field," Appl. Phys. Ltrs. **74**, 436 (1999).
66. Zhao, J., V. Mueller, and Q.M. Zhang, "The Influence of the External Stress on the Electromechanical Response of Electrostrictive $0.9Pb(Mg_{1/3}Nb_{2/3})O_3$-$0.1PbTiO_3$ in the dc Electrical Field Biased State," J. Mat. Res. **14**, 3 (1999).

VOLUME VI

5.0 MODELING and CHARACTERIZATION

5.3 Thin and Thick Thin Films

67. Maria, J.P., W. Hackenberger, and S. Trolier-McKinstry, "Phase Development and Electrical Property Analysis of Pulsed Laser Deposited $Pb(Mg_{1/3}Nb_{2/3})O_3$-$PbTiO_3$ (70/30) Epitaxial Films," J. Appl. Phys. **84** (9), 5147-5154 (1998).
68. Shepard, J.F., Jr., P.J. Moses, and S. Trolier-McKinstry, "The Wafer Flexure Technique for the Determination of the Transverse Piezoelectric Coefficient (d_{31}) of PZT Thin Films," Sensors and Actuators A **71**, 133-138 (1998).
69. Zavala, G. J.H. Fendler, and S. Trolier-McKinstry, "Stress Dependent Piezoelectric Properties of Ferroelectric Lead Zirconate Titanate Thin Films by Atomic Force Microscopy," J. Korean Phys. Soc. **32**, S1464-S467 (1998).
70. Wasa, K., Y. Haneda, T. Satoh, H. Adachi, I. Kanno, K. Setsune, D.G. Schlom, S. Trolier-McKinstry, C.-B. Eom, "Continuous Single Crystal $PbTiO_3$ Thin Films Epitaxially Grown on Miscut (001) $SrTiO_3$," J. Korean Phys. Soc. **32**, S1344-S1348 (1998).
71. Xu, B., Y. Ye, L.E. Cross, J.J. Bernstein, and R. Miller, "Dielectric Hysteresis from Transverse Electric Fields in Lead Zirconate Titanate Thin Films," Appl. Phys. Ltrs. (1998). [submitted]
72. Xu. B., N.G. Pai, Q.-M. Wang, and L.E. Cross, "Antiferroelectric Thin and Thick Films for High Strain Microactuators," Integrated Ferroelectrics **22**, 545-557 (1998).

5.4 Domain Studies

73. Erhart, J. and W. Cao, "Effective Material Properties in Twinned Ferroelectric Crystals," J. Appl. Phys. (1999). [submitted]
74. Belegundu, U., M. Pastor, X.H. Du, L.E. Cross, and K. Uchino, "Domain Formation in $0.90Pb(Zn_{1/3}Nb_{2/3})O_3$-$0.10PbTiO_3$ Single Crystals under Electric Field along [111] Direction," IEEE '98, Sendai, Japan (1998).
75. Zhu, S.N. and W. Cao, "Pyroelectric and Piezoelectric Imaging of Ferroelectric Domains in $LiTaO_3$ by Scanning Electron Microscopy," Phys. Status Solidi (1998). [submitted]
76. Hatch, D.M. and W. Cao., "Determination of Domain and Domain Wall Formation at Ferroic Transitions," Ferroelectric (1998). [submitted]
77. Mueller, V. and Q.M. Zhang, "Threshold of Irreversible Domain Wall Motion in Soft PZT-Piezoceramic. Ferroelectrics **206/207**, 113-122 (1998).
78. Aburatani, H., J.P. Witham, and K. Uchino, "A Fractal Analysis on Domain Related Electric Field Induced Acoustic Emission in Ferroelectric Ceramics," Jpn. J. Appl. Phys. **37**, 602-605 (1998).

5.5 Electrostriction

79. Newnham, R.E., V. Sundar, R. Yimnirun, J. Su, and Q.M. Zhang, "Electrostriction in Dielectric Materials," in *Advances in Dielectric Ceramic Materials*, eds. K. Nair and A. Bhalla. Ceramic Trans. **88**, 154-39 (1998).

80. Sundar, V., R. Yimnirun, B.G. Aitken, and R.E. Newnham, "Structure Property Relationships in the Electrostriction Response of Low Dielectric Permittivity Silicate Glasses," Mat. Res. Bull. **33**, 1307-1314 (1998).

MODELING
and
CHARACTERIZATION

Thin and Thick
Thin Films

APPENDIX 67

JOURNAL OF APPLIED PHYSICS VOLUME 84, NUMBER 9 1 NOVEMBER 1998

Phase development and electrical property analysis of pulsed laser deposited $Pb(Mg_{1/3}Nb_{2/3})O_3$–$PbTiO_3$ (70/30) epitaxial thin films

J.-P. Maria,[a] W. Hackenberger, and S. Trolier-McKinstry
Materials Research Laboratory, Materials Science and Engineering Department, The Pennsylvania State University, University Park, Pennsylvania 16802

(Received 18 March 1998; accepted for publication 20 July 1998)

(001)-oriented heterostructures consisting of $LaAlO_3$ substrates, $SrRuO_3$ bottom electrodes, and $Pb(Mg_{1/3}Nb_{2/3})O_3$–$PbTiO_3$ (PMN-PT) (70/30) films were deposited by pulsed laser deposition from Pb-enriched ceramic targets. The epitaxial growth of all layers was confirmed by four-circle x-ray diffraction. Film growth was carried out over a wide range of processing space where substrate temperature, ambient pressure, and laser parameters were varied in order to determine suitable conditions for producing high quality crystals with good electrical properties. In general, strong similarities were observed between thin film and ceramic processing of the same compositions. The associated pyrochlore phase was very difficult to avoid and, in the absence of excess Pb-containing second phases, could only be done at very high temperatures and high oxygen/ozone pressures for films on $LaAlO_3$ substrates. When deposited at temperatures below approximately 640 °C, PMN-PT films grown from lead-enriched targets exhibited depressed ferroelectric transition temperatures. For depositions at or above 660 °C, the electrical properties approached those of bulk single crystals. In particular, films showed room temperature dielectric constants greater than 1500, well developed Curie–Weiss behavior, and remanent polarization values between 13 and 20 $\mu C/cm^2$. © *1998 American Institute of Physics*. [S0021-8979(98)08520-X]

I. INTRODUCTION

Recently, ultralarge piezoelectric responses have been observed in single crystal solid solutions of relaxor-ferroelectric perovskites and $PbTiO_3$: the specific systems being $Pb(Mg_{1/3}Nb_{2/3})O_3$–$PbTiO_3$ (PMN-PT) and $Pb(Zn_{1/3}Nb_{2/3})O_3$–$PbTiO_3$ (PZN-PT). Optimized electromechanical properties are observed for compositions just on the rhombohedral side of the morphotropic phase boundary. Piezoelectric d_{33} coefficients of 2500 pC/N and unipolar strains as large as 1.7% have been observed when PZN-0.09 PT crystals were measured along ⟨100⟩ type directions, even though the polar axis of these compositions lies along [111].[1,2] Given this measurement orientation and the low strain-field hysteresis, it is believed that domain wall motion does not contribute extensively to the large field-induced strains. This is in contrast to soft piezoelectric PZT ceramics in which more than 50% of the room temperature piezoelectric response is of extrinsic origin.[3]

For the case of ferroelectric microelectromechanical systems (MEMS), it is desirable to generate large strains, or sense very small ones, in thin constrained piezoelectric layers. For $Pb(Zr, Ti)O_3$ (PZT) thin films, the most widely studied piezoelectric composition, when thicknesses are less than 1 μm, it has been demonstrated that the piezoelectric response due to non-180° domain wall motion is limited.[4] Given the ferroelastic nature of domains in PZTs, it is likely that, at least in part, this limitation results from local residual stresses that act to clamp the overall response.[4] Other possibilities include very fine grain size (typically ≤0.2 μm) and high defect concentrations. As a result of these factors, the piezoelectric coefficients (d_{ij}) measured for PZT thin films are limited to those values typical of hard PZT ceramics.[5–7] Since it appears that alternate mechanisms not involving non-180° domain wall motion are responsible for the piezoelectric activity in ⟨001⟩-oriented relaxor-PT single crystals, it is possible that substrate clamping will have a much less pronounced effect on the thin film electromechanical properties. For a well-poled (001)-oriented rhombohedral crystal measured normal to the face, no driving force exists for non-180° domain wall motion as a result of the crystal symmetry.

With these considerations in mind, a study of relaxor-PT epitaxial films for MEMS applications has been performed. The composition $Pb(Mg_{1/3}Nb_{2/3})O_3$–$PbTiO_3$ (70/30) was chosen over the Zn-containing phase since the latter contains two volatile atomic species. In single crystal studies, the PZN composition is favored because its morphotropic composition contains only ~9% $PbTiO_3$; lower $PbTiO_3$ concentrations facilitate more homogeneous crystal growth. The (70/30) ratio was chosen because it lies about 5 mole % to the rhombohedral side of the morphotropic phase boundary where the composition dependence of the electrical properties is the least dramatic.[1]

There are several previous reports concerning the deposition and measurement of PMN and PMN-PT thin films. Deposition methods include sol–gel, rf sputtering, pulsed laser deposition, and chemical vapor deposition.[8–12] For polycrystalline PMN-PT compositions near the morphotropic phase boundary, maximum dielectric constant values near 2000 with low loss tangents were observed.[8,9,12] Remanent polarizations as large as 8 $\mu C/cm^2$ have been measured for morphotropic sol–gel derived (001)-oriented material.[8] To

[a]Electronic mail: jpm133@email.psu.edu

0021-8979/98/84(9)/5147/8/$15.00

TABLE I. Processing conditions for $SrRuO_3$ and PMN-PT epitaxial thin films.

Parameters	$SrRuO_3$	PMN-PT
Temperature (°C)	680	620–700
Atmosphere	10% O_3, 90% O_2	10% O_3 90% O_2
Pressure (mTorr)	200	100–700
Laser power (mJ)	250	250
Laser energy density (J/cm^2)	1.5	1.8–2.2
Target	Stoichiometric	15%–40% excess PbO
Target to substrate distance	7.5 cm	5.5 cm

the best of the authors' knowledge, the deposition of epitaxial relaxor-PT solid solutions has not been previously reported. In addition, there have been few conclusive demonstrations of true relaxor behavior (i.e., dispersive dielectric permittivity below T_m) for any thin film PMN-PT composition.

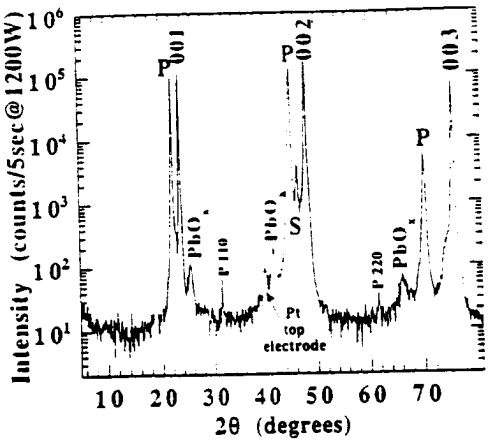

FIG. 1. θ–2θ diffraction pattern of a PMN-PT thin film containing excess PbO_x. Peaks indexed with P indicate perovskite PMN-PT, while those indexed with S denote $SrRuO_3$. 001 indices correspond to substrate reflections.

II. EXPERIMENTAL PROCEDURE

PMN-PT (70/30) epitaxial thin films with $SrRuO_3$ bottom electrodes were prepared on (001) $LaAlO_3$ substrates (Lucent Technologies) by pulsed laser deposition. The specific processing conditions for both materials are given in Table I. Substrates were heated by fixing them to a stainless steel block-style hot stage using silver paint (Demetron). The temperatures given refer to readings taken from a *K*-type thermocouple embedded in the heater block. The 10% O_3 atmosphere refers to the undistilled output of a commercially available ozone generator (PCI). The laser used was a Lambda Physik Compex 102, operating at 248 nm. The PMN-PT samples were cooled in an atmosphere of 250 Torr oxygen/ozone mix immediately after deposition.

PMN-PT laser targets were fabricated by first processing stoichiometric PMN-PT powder of the desired 70/30 ratio; the columbite method was followed.[13] The desired mass percent of PbO was added to the PMN-PT powder and ball milled in ethanol for 4 h to insure homogeneous distribution. Pellets 1 in. in diameter were uniaxially pressed without binder. The samples were placed on Pt foil in an alumina crucible and covered with a Pb source (a 5:1 mixture of PbO and $PbZrO_3$ powders), and an alumina lid was placed on top (no cement was used). The samples were sintered at 950 °C for 1 h. Using this method, less than 1% mass loss occurred in the pellet during the temperature cycle. The $SrRuO_3$ target was purchased from Target Materials Inc. After each deposition, the targets were resurfaced using SiC abrasive paper.

Samples were then characterized to determine the phase assemblage, the crystalline quality, and the low- and high-field electrical properties. Structural analysis was performed on a Picker four-circle diffractometer equipped with a Cu target and a graphite monochromator. Electrical measurements were made through the film thickness using Pt top electrodes 300 μm in diameter prepared by pulsed laser deposition (PLD) through a shadow mask in vacuum. Hysteresis measurements were made using a Radiant Technologies RT66A standard ferroelectrics tester. For low temperature analysis of the polarization hysteresis, the samples were immersed in liquid nitrogen. Dielectric constant and loss values were measured with an HP4284A LCR meter as a function of temperature (−170 °C–200 °C) and frequency (100 Hz–100 kHz) at an excitation field of 0.05 kV/cm. High and low temperature measurements were made using a laboratory oven with both refrigerating and heating capabilities. Contacts to the samples for room temperature measurements were made using point probes, while contacts for temperature dependent analysis were made by aluminum ultrasonic wire bonding.

III. RESULTS AND DISCUSSION

A. Structural analysis

Initially, deposition parameters for PMN-PT were chosen which afforded growth with reasonable rates, smooth morphologies, and uniform thicknesses over 0.5 cm^2 wafers. In general, temperatures between 620 °C and 640 °C, pressures of 200 mTorr, and a target to substrate distance of ~6 cm were found to be appropriate. Using these conditions, the temperature and laser frequency were adjusted so that a film rich in lead was grown, i.e., a mixture of epitaxial perovskite and polycrystalline PbO_x. Once these conditions were achieved, the processing parameters were adjusted to provide increased lead volatility during growth. Figure 1 gives a θ–2θ pattern for a Pb-rich PMN-PT epitaxial film. In this pattern, peaks corresponding to both perovskite and PbO_x are present. In addition to the epitaxial perovskite, a small peak corresponding to the (110) orientation is present at 31.5°. When large quantities of excess PbO_x are present in the films, small volumes of nonepitaxial perovskite (typically <1 vol %) were unavoidable. Although not shown in any of the figures, azimuthal scans and rocking curves were taken for all the samples discussed. All samples were oriented in plane with peak widths between 0.6° and 0.8° in ϕ and between 0.4° and 0.7° in ω. Representative ϕ and ω scans are given in Fig. 2.

The next step in structural optimization was to remove the excess lead-containing phases and arrive at a globally

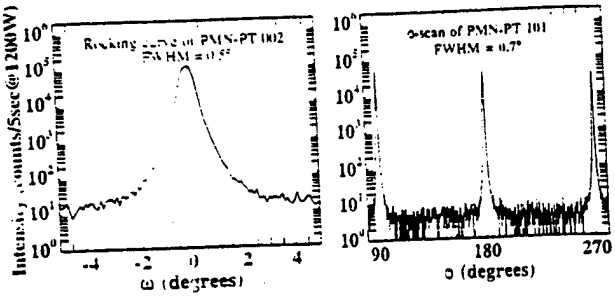

FIG. 2. Rocking curve and ϕ scan for typical PMN-PT epitaxial films.

stoichiometric epitaxial film. To systematically increase the sublimation rate of a volatile element during deposition, the best laser parameters to change are laser pulse frequency and substrate temperature. Reducing the laser frequency increases the amount of time between pulses during which sublimation can occur, while increasing the temperature exponentially increases the sublimation rate of the solid.[14] Adjustments in the thin film Pb stoichiometry may also be accomplished by changing other parameters, i.e., laser fluence, pressure, and target to substrate distance. These parameters, however, are coupled to other aspects of the deposition such as instantaneous growth rate, energetic bombardment, and phase stability. To avoid these cross-coupled effects, when possible, these parameters were fixed. Figure 3 is a θ–2θ pattern for a PMN-PT film deposited at a reduced laser frequency (by ~20%) in reference to the film in Fig. 1. It is clear in this pattern that the quantity of excess PbO_x is reduced; however, before it is completely removed, a significant amount of pyrochlore has evolved. The observed pyrochlore phase has an x-ray pattern similar to that of $Pb_{1.83}Nb_{1.71}Mg_{0.29}O_{6.39}$, however, many phases with nearly identical x-ray signatures and plausible stoichiometries exist, thus an unambiguous phase assignment is not possible. This coexistence of stoichiometric, Pb-rich, and Pb-deficient phases occurs in bulk processing of ceramics as well, and is

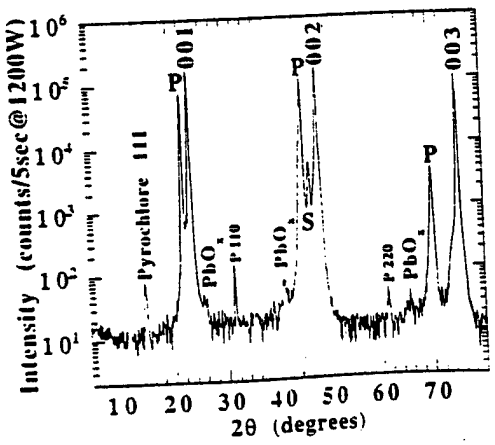

FIG. 3. θ–2θ diffraction pattern of a PMN-PT thin film deposited under conditions favoring increased PbO_x volatility compared to that shown in Fig. 1. The coexistence of perovskite, PbO_x, and pyrochlore is demonstrated.

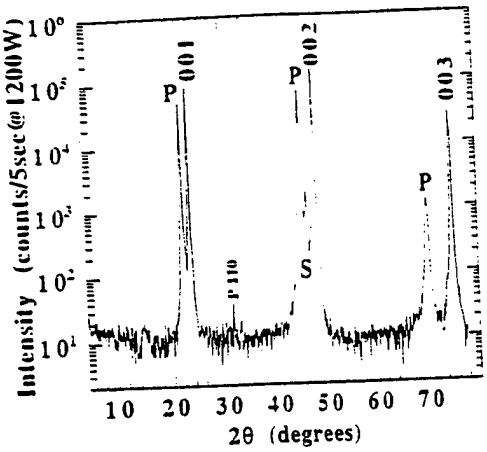

FIG. 4. θ–2θ diffraction pattern of a PMN-PT thin film deposited at 700 °C and 700 mTorr O_2/O_2. To the detection limits of x-ray diffraction, the material is single phase and epitaxial.

a result of the relatively similar thermodynamic stabilities of the perovskite and pyrochlore phases of PMN-PT at the temperatures of interest.[13]

From the ceramic processing and single crystal growth literature it is known that increased temperature and oxygen partial pressures will favor the perovskite phase.[13,15] Thus, the deposition pressures and temperatures were raised to 710 °C and 700 mTorr, and the Pb content was again optimized. Figure 4 shows a θ–2θ pattern for a structurally optimized film deposited under these conditions. In addition to the increased pressure and temperature, the target to substrate distance was reduced to 3.5 cm. This was necessary to increase the instantaneous deposition rate in order to supply enough Pb to the growing film. To the detection limits of our diffractometer, no pyrochlore or Pb-rich phases are present. Intermediate oxygen pressures and temperatures (~400 mTorr and ~680 °C) were also attempted with improved results over the initial case.

A mild dependence of the lattice constants on Pb stoichiometry was observed (this assumes that the ratio of the other elements remained constant with changing laser frequency). In samples containing excess quantities of lead, the lattice parameter reflected bulk values (4.03 Å), while for samples showing no excess lead, that is, either phase pure or pyrochlore containing, the lattice constant was consistently reduced by approximately 0.02 Å. A limited number of films were deposited using $SrTiO_3$ substrates. When used, these epitaxial templates widened the processing window for phase-pure PMN-PT films. Most likely, the superior lattice match improved the stability of the PMN-PT phase.

B. Electrical property analysis

Initially, phase-pure samples were electrically characterized, and were found to have insufficient resistivity for any meaningful dielectric analysis to be performed. Since these samples showed lattice constants which were slightly smaller than what is observed in the bulk, it was assumed that lead deficiency was responsible for the high leakage. Thus the deposition conditions were modified to reduce the lead defi-

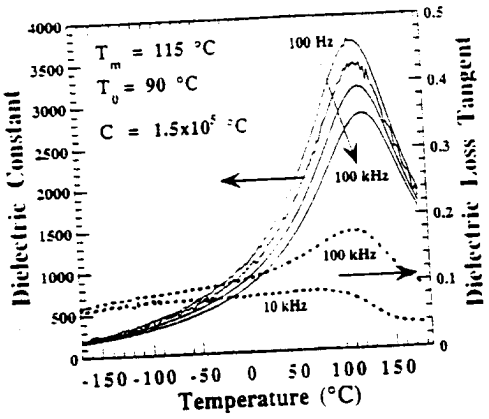

FIG. 10. Temperature dependence of the dielectric constant and dielectric loss of a PMN-PT thin film deposited at 660 °C containing excess PbO_x. T_m refers to the temperature of the maxima in the dielectric constant at 100 Hz. T_0 refers to the extrapolated Curie–Weiss temperature, and C refers to the Curie–Weiss constant.

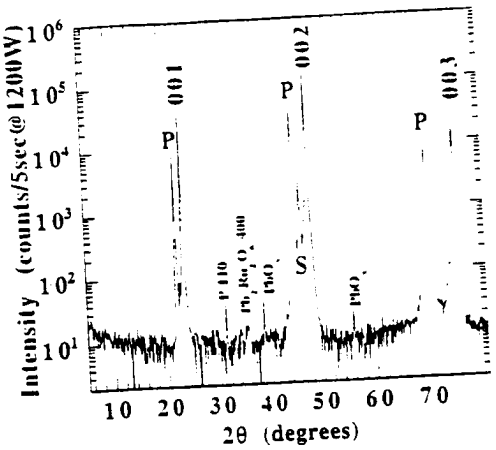

FIG. 12. θ–2θ diffraction pattern of a PMN-Pt thin film deposited at 660 °C. The peak corresponding to lead ruthenate is a result of reaction with the underlying $SrRuO_3$ electrode.

Because of the difficulty in reproducing high quality samples at elevated temperatures (a result of increased lead and lead oxide volatility), a target containing 2% Ba doping was introduced. Ba was chosen because of its ability to stabilize the perovskite phase with respect to the associated lead-deficient pyrochlore. The addition of Ba into the PMN-PT increases the tolerance factor (a calculated quantity indicative of the thermodynamic stability of the perovskite structure) of the crystal.[26] For Ba-substituted PMN and PT, a decrease in T_m of approximately 20 °C/mol % has been reported.[27,28] Although it has never not been demonstrated for the specific PMN-PT composition investigated here, it is likely that the Ba addition will have a similar effect. Indeed, reports on the substitution of La and Sr into the morphotropic composition show very similar transition shifts, i.e., approximately 20 °C/mol %.[27–29] Since T_m for undoped (70/30) single crystals is 150 °C,[25] with 2% Ba doping, the T_m value would be expected to fall to approximately 110 °C. Figures 10 and 11 give the temperature dependence of the dielectric constant and the polarization hysteresis for a PMN-PT film deposited under the optimized deposition conditions. As is shown in Figs. 10 and 11, the T_m value is 115 °C and the remanent polarization is 17 μC/cm^2. This remanent polarization value is about 75% of that measured in undoped single crystals of the same composition.[25] Extrapolation of the saturation polarization gives the single crystal value. The temperature dependence of the capacitance in the paraelectric region was fitted to Curie–Weiss behavior using

$$\epsilon = \frac{C}{(T - T_0)}.$$

A Curie–Weiss constant, C, of 1.5×10^5 °C was calculated. This value is on the same order as other relaxor-PT solid solutions in the vicinity of the morphotropic composition and was found to be frequency independent.[25] Figure 12 gives a θ–2θ pattern for the higher temperature deposited material. Again, this sample contains a small amount of PbO_x.

Upon comparison of the x-ray patterns for the low and higher temperature deposited PMN-PT films, only subtle differences in the structure are observed. In general, for the lower temperature deposited samples, the x-ray linewidths are approximately 10% greater and peak intensities are nearly 30% larger. The differences in the electrical property temperature dependencies of the PMN-PT samples grown at 620 °C and those deposited at or above 660 °C are attributed to the sample crystallinity.

In a very straightforward manner, the x-ray analysis indicates that the high temperature grown samples have a larger coherent x-ray scattering dimension. Using a Williamson–Hall analysis, a dimension of ~500 Å is calculated.[30] In comparison, with the same treatment, the scattering size for the lower temperature deposited samples was found to be ~100 Å. This analysis gives a semiquantitative picture of the sub-grain structure. Combining this data with the permittivity temperature dependence one finds that the smaller scattering regions are accompanied by the temperature shifted transition, the broadened and more dispersive dielectric maxima, and the deviation from Curie–

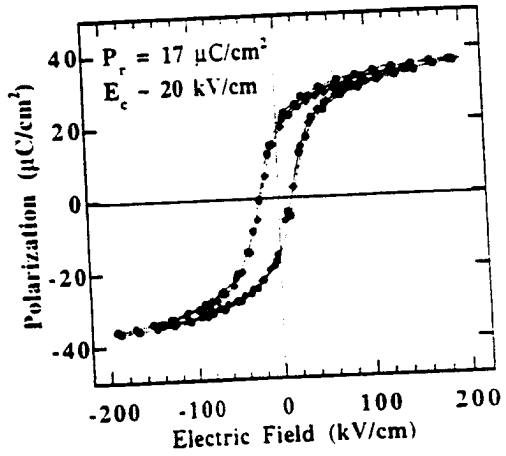

FIG. 11. Room temperature polarization hysteresis of a PMN-PT thin film deposited at 660 °C containing excess lead.

Weiss behavior. Interestingly, the 100 Å dimension is consistent with the 100 Å diameter ordered regions observed in ceramic relaxors of several compositions.[16]

The broadened x-ray reflections in the lower temperature deposited sample are produced by two factors: (i) larger variations in interplanar spacings in the crystal and (ii) a mosaic subgrain structure. The more pronounced mosaic structure of the lower temperature deposited sample would result in greater concentrations of dislocations which occur at the interfaces of the slightly misoriented subgrains.[31] The higher defect concentrations are believed to interrupt the long-range order of the lattice, and to produce electrical behavior more consistent with that of relaxor ferroelectrics. It is likely that if deposition temperatures could be further increased, or if a better lattice matched substrate/electrode/film system were used, electrical properties more similar to those of single crystals could be realized.

The optimized samples deposited at temperatures greater than 660 °C still contained lead-rich second phases, which, if removed, would be expected to further improve the film properties. In particular, the presence of a low K second phase may be responsible for the comparatively low dielectric constant values observed (approximately a factor of 2 smaller than expected). Samples with excess lead oxide in the x-ray patterns were etched for 5 min in concentrated acetic acid in an attempt to remove PbO_x from the film surface. Postetching x-ray analysis revealed no changes in the structure or phase assemblage. It was thus concluded that the excess lead oxide does not reside principally on the film surface. This information, coupled with the high film resistivities, suggests that the excess lead oxide must exist as a noncontiguous second phase.

Ex situ annealing was also performed in an attempt to improve the film properties. Three specific experiments were performed: (i) annealing of a lead-rich film in air, (ii) annealing of a Pb-rich film in the presence of a Pb-compensated atmosphere, and (iii) annealing a phase-pure film in a Pb-compensated atmosphere. The Pb-compensated atmosphere was provided by a loosely covered crucible partially filled with a $PbO-PbZrO_3$ powder, into which the sample was placed. The samples were introduced and removed from a preheated tube furnace to minimize the amount of time spent at high temperatures.

A film similar in structure to that shown in Fig. 1 (i.e., containing excess Pb) was introduced to the 750 °C furnace in a closed, empty crucible for 30 min. X-ray analysis of the crystal after annealing indicated that PbO_x was still present in the film, in addition to a newly formed pyrochlore. This situation is analogous to the phase development observed during growth at 200 mTorr oxygen/ozone pressure: under these conditions as well, three phases can exist simultaneously, perovskite, pyrochlore, and PbO_x. Following this result, no other samples were annealed in a non-Pb atmosphere. In the postanneal x-ray pattern, a peak corresponding to $Pb_2Ru_2O_{6.5}$ appeared and was attributed to reaction with the bottom electrode. For this reason, the annealing temperatures were dropped to 650 °C.

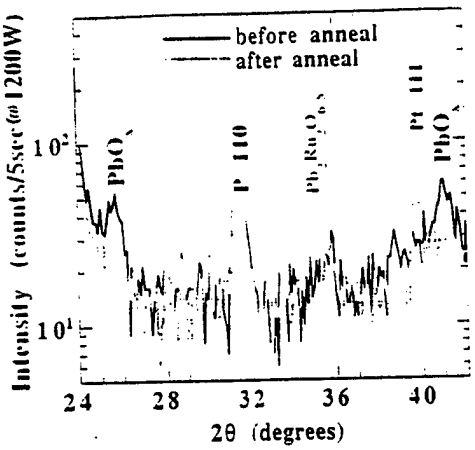

FIG. 13. θ–2θ pattern of a PMN-PT thin film containing excess lead before and after a 30 min anneal in a lead-compensated atmosphere.

The next experiment involved annealing films in a Pb-rich environment. In the previously described crucible system, three volatile components existed, perovskite, the Pb source, and PbO_x (listed in order of expected decreasing stability at high temperatures). During the anneal, ideally, the most volatile component, the PbO_x, would evaporate initially, leaving the remaining Pb source and phase-pure perovskite behind. A film synthesized with a large amount of excess lead was heat treated in this fashion: the result is shown in Fig. 13, an x-ray diffraction pattern of the film before and after heat treatment. This sample contains some (110)-oriented material as a result of the large initial amount of excess PbO_x. After annealing, it is apparent that much of the PbO_x has sublimed without the formation of pyrochlore. At $2\theta = 35.1°$, however, a $Pb_2Ru_2O_{6.5}$ 400 reflection is again observed. Several samples containing slightly different amounts of excess Pb were annealed in this manner and characterized. Structurally, the PMN-PT x-ray patterns were unchanged with annealing; however, the amount of reacted $Pb_2Ru_2O_{6.5}$ was directly related to the amount of excess lead oxide prior to heat treatment. Annealed films with the smallest amounts of $Pb_2Ru_2O_{6.5}$ showed resistivities increased by as much as a factor of 100, and slight increases of the permittivity. Polarization hysteresis measurements, however, gave misshapen hysteresis loops which may be associated with the newly formed ruthenate.

The annealing experiments indicate that, in the presence of a lead source with a stability between that of perovskite and PbO_x, excess Pb can be extracted without the formation of a pyrochlore type phase. In the present case, the inability to do so completely was a result of reaction between the $SrRuO_3$ bottom electrode and Pb. Quite possibly, with a more stable electrode, phase-pure perovskite films with good electrical properties can be achieved. Pt and $LaNiO_3$ are possible choices.

Finally, those films deposited at temperature and pressure combinations high enough to promote phase-pure perovskite growth were annealed in a lead-rich atmosphere. X-ray analysis of the annealed films indicated no appreciable differences in film structure, and electrical property measure-

ments revealed that the resistivities remained unacceptably low. It appears that, under the annealing conditions examined, sufficient amounts of lead could not be driven into the films for improved electrical properties to be observed.

IV. CONCLUSIONS

To the authors' knowledge, this is the first report of epitaxial films of the relaxor-$PbTiO_3$ solid solution $Pb(Mg_{1/3}Nb_{2/3})O_3$–$PbTiO_3$ (70/30) deposited by PLD. Avoiding the occurrence of the pyrochlore phase was found to be very difficult, and was only possible in a narrow processing window. In general, the trends observed in ceramic processing of PMN-PT were analogous to those observed in this study. In one PMN-PT film, it was possible to simultaneously observe perovskite, pyrochlore, and, PbO_x. As in bulk processing work, higher temperatures and oxygen pressures favored the perovskite phase. The epitaxial effect of the $LaAlO_3$ substrate during growth was insufficient to avoid pyrochlore. Phase-pure material could be deposited at temperatures in excess of 700 °C and oxygen pressures approaching 1 Torr, however, electrically, these samples were typified by unacceptably low resistivities. In general, films with excess PbO_x showed good electrical properties (large resistivities and low loss tangent values). Electrically, samples deposited at temperatures near 620 °C resembled relaxors in the vicinity of T_m: the T_m value of these samples was found to be decreased by ~100 °C. This behavior was attributed to high defect densities. When the deposition temperatures were increased to 660 °C or higher, electrical properties more similar to those of bulk single crystals were observed. X-ray analysis of these films confirmed improved crystallinity. In samples deposited in the lower temperature regime, true relaxor behavior was observed, i.e., a frequency dependent permittivity and loss tangent in the ferroelectric region, and converging values in the paraelectric state. Post-deposition annealing in a Pb-rich atmosphere was attempted in order to produce phase-pure films. This annealing strategy was found to be effective in removing excess Pb without nucleation of pyrochlore; however complete removal was limited by an unavoidable reaction of Pb with the $SrRuO_3$ bottom electrode.

ACKNOWLEDGMENTS

The authors would like to acknowledge the National Science Foundation for providing the financial support for this research under Contract Nos. NSF DMR-9223847 and NSF DMR-9502481. The authors also wish to recognize Dr. T. R. Shrout and Dr. S. E. Park for their technical support.

[1] S. Park and T. R. Shrout, IEEE Trans. Ultrason. Ferroelectr. Freq. Control 44, 1140 (1997).
[2] S. E. Park and T. R. Shrout, J. Appl. Phys. 82, 1804 (1997).
[3] X. L. Zhang, Z. X. Chen, L. E. Cross, and W. A. Schulze, J. Mater. Sci. 18, 968 (1983).
[4] S. Trolier-McKinstry, J. F. Shepard, Jr., T. Su, J. L. Lacey, G. Zavala, and J. Fendler, Ferroelectrics 206–207, 381 (1997).
[5] P. Muralt, A. Kholkin, M. Kohli, T. Maeder, and N. Setter, Microelectron. Eng. 29, 67 (1995).
[6] I. Kanno, S. Fujii, T. Kamada, and R. Takayama, Appl. Phys. Lett. 70, 1378 (1997).
[7] S. Watanabe, T. Fujiu, and T. Fujii, Appl. Phys. Lett. 66, 1481 (1995).
[8] M. Shyu, T. Hong, and T. Wu, Mater. Lett. 23, 221 (1995).
[9] T. Nakamura, A. Masuda, A. Morimoto, and T. Shimizu, Jpn. J. Appl. Phys., Part 1 35, 4750 (1996).
[10] M. C. Jiang, T. Hong, and T. B. Wu, Jpn. J. Appl. Phys., Part 1 33, 6301 (1994).
[11] Y. Takeshima, K. Shiratsuyu, H. Takagi, and K. Tomono, Jpn. J. Appl. Phys., Part 1 34, 5083 (1995).
[12] M. C. Jiang and T. B. Wu, J. Mater. Res. 9, 1879 (1994).
[13] S. L. Swartz and T. R. Shrout, MRS Bull. 17, 1245 (1982).
[14] D. L. Smith, *Thin Film Deposition* (McGraw–Hill, New York, 1995).
[15] N. Wakia, A. Sakai, N. Ishizawa, K. Shinosaki, and N. Mizutani, MRS Bull. 28, 137 (1993).
[16] L. E. Cross, Ferroelectrics 151, 305 (1993).
[17] J. F. M. Cillessen, M. W. J. Prins, and M. R. Wolf, J. Appl. Phys. 81, 2777 (1997).
[18] A. K. Tagantsev, M. Landivar, E. Colla, K. G. Brooks, and N. Setter, Integr. Ferroelectr. 6, 309 (1995).
[19] J. P. Zheng, Z. Q. Huang, D. T. Shaw, and H. S. Kwok, Appl. Phys. Lett. 54, 280 (1989).
[20] P. W. Forsbergh, Jr., Phys. Rev. 93, 686 (1954).
[21] G. A. Samara, Phys. Rev. 151, 378 (1966).
[22] Y. S. Touloukian, *Thermophysical Properties of Matter*, TPRC Data Series Vol. 13 (IFI/Plenum, New York, 1979).
[23] H. M. O'Bryan, P. K. Gallagher, G. W. Berkstresser, and C. D. Brandle, J. Mater. Res. 5, 183 (1990).
[24] S.-J. Jang, Ph.D. thesis, The Pennsylvania State University, 1979.
[25] S. Park and T. R. Shrout (unpublished data).
[26] T. R. Shrout and A. Halliyal, Am. Ceram. Soc. Bull. 66, 704 (1987).
[27] S. J. Butcher and N. W. Thomas, J. Phys. Chem. Soc. 52, 595 (1991).
[28] B. Jaffe, W. R. Cook, and H. Jaffe, *Piezoelectric Ceramics* (Academic, Marrietta, OH, 1971).
[29] N. Kim, M.S. thesis, The Pennsylvania State University, 1990.
[30] G. K. Williamson and W. H. Hall, Acta. Metall. 1, 22 (1953).
[31] B. D. Cullity, *Elements of X-ray Diffraction*, 2nd ed. (Addison–Wesley, Reading, MA, 1978).

APPENDIX 68

ELSEVIER

Sensors and Actuators A 71 (1998) 133–138

SENSORS AND ACTUATORS A PHYSICAL

The wafer flexure technique for the determination of the transverse piezoelectric coefficient (d_{31}) of PZT thin films

J.F. Shepard Jr. *, P.J. Moses, S. Trolier-McKinstry

Materials Research Laboratory, The Pennsylvania State University, University Park, PA 16802, USA

Received 9 June 1997; received in revised form 3 April 1998; accepted 3 April 1998

Abstract

This paper describes a simple and inexpensive method for evaluating the transverse piezoelectric coefficient (d_{31}) of piezoelectric thin films. The technique is based upon the flexure of a coated substrate which imparts an ac two-dimensional stress to the piezoelectric film. The surface charge generated via the mechanical loading is converted to a voltage by an active integrator. Plate theory and elastic stress analyses are used to calculate the principal stresses applied to the film. The d_{31} coefficient can then be determined from knowledge of the electric charge produced and the calculated mechanical stress. For 52/48 sol–gel lead zirconate titanate (PZT) thin films, the d_{31} coefficient was found to range from −5 to −59 pC/N and is dependent on poling field.

Keywords: Transverse piezoelectric coefficient; Thin films; PZT

1. Introduction

The design and development of novel microelectromechanical systems (MEMS) which utilize piezoelectric thin films [1,2] require explicit knowledge of the material's longitudinal (d_{33}) and transverse (d_{31} or d_{32}) piezoelectric coefficients. When prepared in bulk ceramic form, piezoelectric coefficients are characterized by numerous methods, the most common of which are resonance and dynamic load techniques (Belincourt meter). Those techniques, however, are inadequate for the piezoelectric characterization of thin film materials and for that reason a number of alternative techniques (e.g., laser beam interferometry and normal load methods) have been proposed [3,4].

Laser interferometers are the most well-established method for the characterization of both the longitudinal and transverse piezoelectric coefficients of piezoelectric thin films [3,5–7]. Interferometers can be configured as either single- or double beam setups and are based upon the interference of monochromatic laser light in response to a piezoelectrically-induced strain (which results in a change of the optical path length). The wavelength of the laser and the intensity of the interference signal produced are input to a simple mathematical model from which the electric-field induced strains are determined. The ultimate resolution of interferometric technique(s) is limited by extraneous displacements (e.g., sample flexure, thermal drift) and environmental noise (electrical and mechanical) to 10^{-4} Å for the best double-beam instruments [3] and 10^{-5} Å for certain single beam instruments [7]. This method requires careful optical alignment, meticulous operation, and in the case of a d_{31} measurement, appropriate sample preparation (cantilever beam construction).

There are alternatives to interferometric characterization and reports have been published on a number of designs which utilize the direct piezoelectric effect. The normal load method, as was described in the work of Lefki and Dormans [4], is analogous to the common Belincourt meter; however, the measured d_{33} values (400 pC/N for undoped sol–gel PZT with compositions near the morphotropic phase boundary) appear improbable in light of the limited twin wall motion in PZT thin films [8,9]. Transverse piezoelectric characterization (d_{31}) has also been attempted [10] and work was based upon the controlled bending of a small cantilever beam. Reasonable d_{31} values were obtained [11]; however, the necessary construction of cantilever test samples is a drawback to the technique.

The wafer flexure technique described in this paper is an alternative method for the characterization of the transverse piezoelectric coefficient (d_{31}) which eliminates a number of the complexities associated with other designs. Experiments conducted have produced d_{31} values comparable to those measured with more established methods (e.g., interferometric). However, the speed with which the measurement is

* Corresponding author. Tel.: +1-814-865-9931; Fax: +1-814-865-2326.

0924-4247/98/$ - see front matter
PII S0924-4247(98)00161-7

made. the relative cost of the hardware, and the utilization of complete silicon substrates makes the wafer flexure technique an attractive alternative for the d_{31} characterization of thin films.

2. Principle of operation

The wafer flexure technique for measuring d_{31} is based upon the direct piezoelectric effect. The controlled bending of a PZT coated substrate imposes a planar two-dimensional mechanical stress upon the film. The strained film responds by developing a surface charge which is monitored electronically. The principle stresses applied to the film are then calculated using small deflection plate theory [12] and the piezoelectric coefficient is determined as

$$D_3 = d_{31}(\sigma_1 + \sigma_2) \quad (1)$$

where d_{31} is the transverse piezoelectric coefficient (C/N), D_3 is the induced dielectric displacement (C/m^2), and σ_1 and σ_2 are the principal stresses applied to the film (N/m^2).

3. Experimental design

The wafer flexure apparatus consists of three discrete components (see Fig. 1): (1) the uniform pressure rig, (2) the charge integrator, and (3) the peripheral electronics. Each of these components will be described in the subsections which follow.

3.1. Uniform pressure rig

The uniform pressure rig consists of two aluminum parts, the housing and the retention ring, between which is placed a 3 in. (76.2 mm) test wafer. The inner radius of both portions measures 1.25 in. (31.75 mm) and at points of contact with the sample, the aluminum has been polished to 5 μm roughness (to improve the pressure seal and to reduce the risk of substrate fracture). The pneumatic pressure in the cavity behind the wafer is oscillated periodically with a 60 cm^3 plastic syringe. Pressure changes are monitored with a piezoresistive pressure transducer (Omega PX236, 30 psig full scale) excited and monitored with an EG&G 7260 lock-in amplifier. Fig. 2 shows a blown-up schematic of the design.

3.2. Charge integrator

The charge integrator used to monitor the change in the film's dielectric displacement as a function of mechanical stress is shown in Fig. 3. Charge from the piezoelectric film is directed to an operational amplifier integrator. The input to this circuit is a virtual ground so the film is held in a zero field state (to within a few millivolts). Charge is collected on a polypropylene internal reference capacitor which provides good temperature stability and low dielectric absorption. Since the op amp integrator circuit is in an inverting configuration, a second op amp is used to invert the output voltage from the first op amp. The output from the device is then reported as a voltage which is proportional to the amount of charge collected on the reference capacitor.

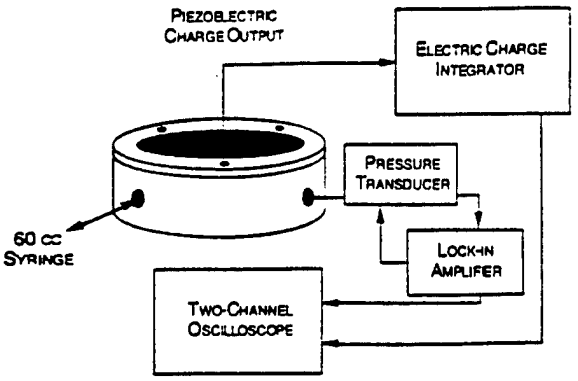

Fig. 1. Experimental setup.

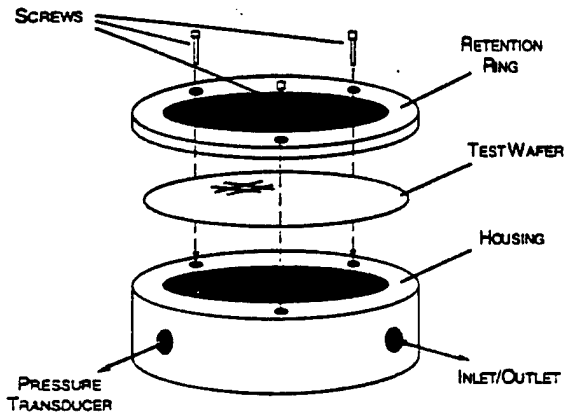

Fig. 2. Uniform pressure rig.

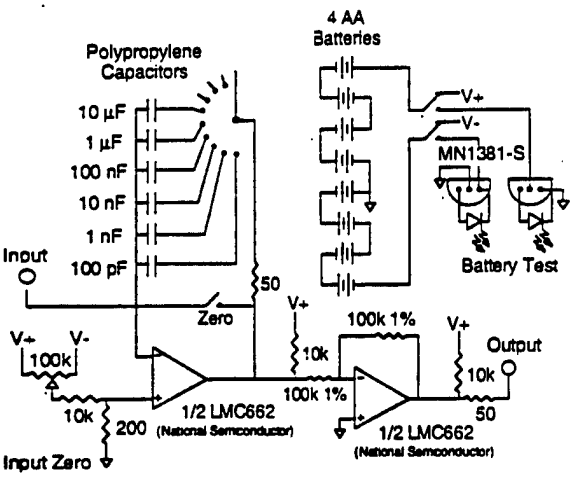

Fig. 3. Electric charge integrator.

3.3. Peripheral electronics

The pressure transducer used in our experiments is constructed in a Wheatstone bridge configuration where the out-

put voltage across the bridge is proportional to the change in pressure within the rig housing. Electromagnetic noise was minimized by using a lock-in technique to both excite the bridge and monitor the change in the output signal. Signals from both the lock-in amplifier and the charge integrator were input to a Hewlett-Packard 54600 oscilloscope and the two traces produced were used to calculate (1) the piezoelectric charge created and (2) the change in mechanical load.

4. Stress analysis and the calculation of d_{31}

The determination of the film's transverse piezoelectric coefficient requires knowledge of the mechanical stress applied to the film. Small deflection plate theory was used together with the pressure applied to the wafer, the support radius, the substrate thickness, and the test capacitor location to calculate the principle stresses at a specific location on the silicon substrate. The bending stresses which result from a uniform pressure on a clamped circular plate are [12]:

$$\sigma_r = \frac{3p_0 z}{4t^3}[(1+\nu)a^2-(3+\nu)r^2] \tag{2}$$

$$\sigma_t = \frac{3p_0 z}{4t^3}[(1+\nu)a^2-(1+3\nu)r^2] \tag{3}$$

where σ_r and σ_t are the radial and tangential stresses on the plate. z is the distance from the neutral axis, t is the plate thickness, ν is Poisson's ratio, a is the support radius, and r is the distance from the center of the plate.

Because the mechanical properties of the silicon substrate and the piezoelectric films differ, wafer stresses calculated from plate theory must be corrected to determine film stress. The assumption was made that all strain applied to the substrate was transferred to the film. Knowing the stresses applied to the substrate (Eqs. (2) and (3)), the strains are calculated via generalized Hooke's law as:

$$\varepsilon_1^{Si} = \frac{\sigma_1^{Si}}{E_{Si}} - \nu_{Si}\frac{\sigma_2^{Si}}{E_{Si}} \tag{4}$$

$$\varepsilon_2^{Si} = \frac{\sigma_2^{Si}}{E_{Si}} - \nu_{Si}\frac{\sigma_1^{Si}}{E_{Si}} \tag{5}$$

where σ_1^{Si} is applied stress in the 1 direction (1 and 2 are the principal in-plane directions corresponding to the tangential or radial orientation), ε_1^{Si} is the strain in the 1 direction, ν_{Si} is the Poisson's ratio of the silicon, and E_{Si} is Young's modulus of the silicon. Because of the conservation of strain, Hooke's law may be written in a similar manner for the PZT film where:

$$\varepsilon_1^{PZT} = \frac{\sigma_1^{PZT}}{E_{PZT}} - \nu_{PZT}\frac{\sigma_2^{PZT}}{E_{PZT}} \tag{6}$$

$$\varepsilon_2^{PZT} = \frac{\sigma_2^{PZT}}{E_{PZT}} - \nu_{PZT}\frac{\sigma_1^{PZT}}{E_{PZT}} \tag{7}$$

The equations for σ_1^{PZT} and σ_2^{PZT} can be derived explicitly by setting $\varepsilon_1^{PZT} = \varepsilon_1^{Si}$ and $\varepsilon_2^{PZT} = \varepsilon_2^{Si}$ which yields

$$\sigma_1^{PZT} = \varepsilon_1^{Si}E_{PZT} + \nu_{PZT}\sigma_2^{PZT} \tag{8}$$

and

$$\sigma_2^{PZT} = \frac{E_{PZT}}{(1-\nu_{PZT}^2)}(\varepsilon_2^{Si} + \nu_{PZT}\varepsilon_1^{Si}) \tag{9}$$

The expansion of Eq. (9) yields a more fundamental form of the equation written in terms of the elastic properties of the silicon and the elastic properties of the PZT film where:

$$\sigma_2^{PZT} = \frac{E_{PZT}}{(1-\nu_{PZT}^2)}\left[\frac{\sigma_1^{Si}}{E_{Si}}(\nu_{PZT}-\nu_{Si}) + \frac{\sigma_2^{Si}}{E_{Si}}(1-\nu_{PZT}\nu_{Si})\right] \tag{10}$$

The expressions derived are appropriate for small deflections of a coated wafer if the ratio of the PZT film thickness to the silicon substrate thickness is small. For the case of a PZT film on a silicon substrate, the thickness ratios are much less than 1% and deformation of the composite wafer will be governed by the elastic properties of the silicon substrate. Furthermore, because small deflection plate theory is used, the maximum deflection of the coated wafer may not exceed 20% of the thickness of the plate [12,13]. For deflections beyond that point, membrane (i.e., stretching) stresses are no longer negligible and use of the small deflection equations would result in significant error.

5. Numerical considerations

5.1. Elastic modulus of PZT Film

Eqs. (9) and (10) show that the stress on the film is dependent upon both the elastic properties of the silicon and the PZT. Inaccuracies in those quantities will carry through the stress analysis and to the subsequent d_{31} calculation. It is important to note that although the mechanical properties of silicon are well characterized [14,15] the properties of thin film PZT are not. That observation is important because at present all methods (converse [3], direct [10], or values derived from low-field measurements [16]) for the determination of the transverse piezoelectric coefficient require explicit knowledge of the material's elastic moduli. Published values have ranged from 37 [17] to 400 GPa [2] and it should therefore be noted that the disparities among d_{31} values reported in the literature could result from the different elastic moduli used in their calculation. The Young's modulus used in this investigation was taken as 101 GPa [18] and was selected in order to yield a lower limit for the d_{31} coefficient (i.e., calculated stress increases and d_{31} decreases).

5.2. Anisotropy of the silicon substrate

The anisotropy of the silicon substrate can complicate the calculation of applied stress, however, strain gauge measure-

Table 1
Elastic properties used in the elastic stress analysis

Material	Young's modulus (GPa)	Poisson's ratio
{100} Silicon substrate [14]	150	0.172
PZT thin film [18]	101	0.3

ments along the ⟨100⟩ and ⟨110⟩ directions of a bare wafer showed no significant difference in the mechanical response [19]. That result suggests that the elastic properties which govern deformation of the substrate can be represented with single values of Poisson's ratio and Young's modulus. A comparison of the experimental and theoretical strains (as calculated from plate theory) gave the best agreement when the average of the maximum and minimum in-plane elastic constants (the ⟨100⟩ and ⟨110⟩ directions) were used in the calculation. For that reason the silicon was treated as an isotropic plate and the averages of both the Young's modulus and Poisson's ratio were used in the d_{31} calculations presented here. Table 1 summarizes the mechanical properties of both the silicon substrate and the PZT film.

6. Preliminary results

Initial characterization experiments were conducted with lead zirconate titanate (PZT) thin films. The films used were synthesized on 3-in. platinized silicon substrates using a conventional sol–gel procedure [20]. Solutions with 52/48 compositions (zirconium to titanium ratio) were diluted to 0.5 M concentrations and spin coated at 3000 rpm for 30 s. Individual PZT layers were pyrolyzed at 300°C and amorphous films were rapid thermal annealed at 650°C for 60 s in air. The thickness of films measured were on the order of 0.4 μm.

6.1. Strength of poling field

Table 2 shows the variation of d_{31} with the magnitude of the applied poling field for two samples at different locations on the same wafer. Results were obtained within 5 min after poling the sample for less than 1 min and suggest that above the coercive field (typically about 50–60 kV/cm for these 52/48 sol–gel films) the d_{31} value is independent of field strength.

Table 2
d_{31} coefficients as a function of poling field

Poling field (kV/cm)	d_{31} (pC/N)	
	Sample 1	Sample 2
50	−7	−5
100	−15	−13
150	−16	−14
200	−16	−15
250	na	−13

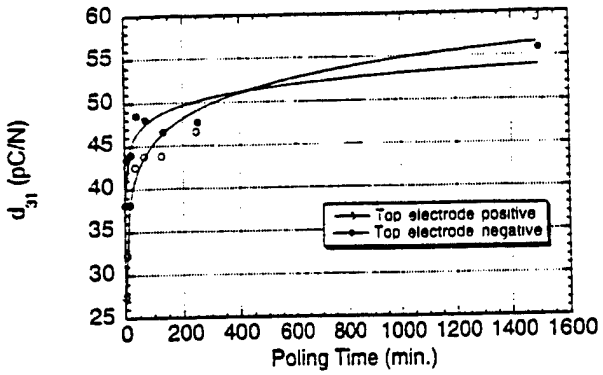

Fig. 4. The variation of d_{31} with poling time for an applied field of 150 kV/cm.

6.2. Poling time

The effect of poling time at 150 kV/cm on the measured d_{31} value of a 52/48 sol–gel PZT film is presented in Fig. 4. The data indicate a rapid increase of the piezoelectric coefficient for increased poling times from 1 to 20 min. For exposure times greater than 20 min the rate of change of d_{31} slows. The maximum value achieved was −59 pC/N for a poling time of ~21 h with the top electrode as the positive terminal. Data are also included in the plot for the same sample poled in the opposite direction. The trends reported are similar for both poling scenarios and indicate that the magnitude of the d_{31} coefficient is independent of the direction of the poling field for long poling times.

6.3. Amplitude of applied stress

The transverse coefficient was also measured as a function of the amplitude of the applied mechanical stress from ~10 to ~50 MPa (sum of the principal stresses) for a sample poled with an electric field of ÷150 kV/cm for less than 1 min. In a bulk ceramic, the increase of applied stress would be expected to result in the reorientation of non-180° domain walls, which would change the d_{31} coefficient from its original value. Prior experiments on the relation between stress and low-field dielectric response have indicated, however, that ferroelastic domain reorientation is negligible [8,9] in these films and, as a result, the piezoelectric coefficients should remain constant. That was in fact the case, and the results from the two experiments conducted (given in Fig. 5) serve to further illustrate: (1) the limited twin wall motion in sol–gel films, and (2) the validity of the wafer flexure technique.[1]

6.4. Variation of d_{31} over the surface of a 3 in. wafer

The d_{31} coefficient was monitored as a function of position over the surface of a coated wafer. This was done to evaluate

[1] It should be noted that Fig. 5 is expressed as a function of the amplitude of the applied air pressure and not the biaxial stress applied to the PZT film.

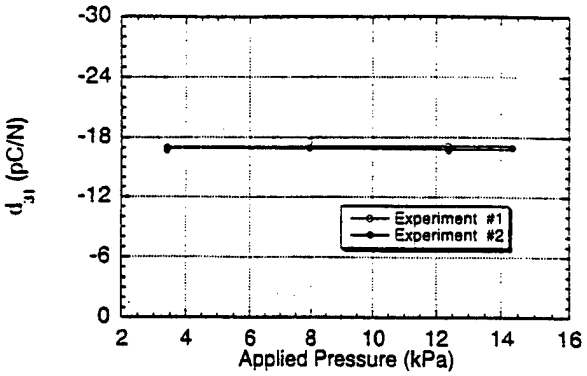

Fig. 5. d_{31} as a function of the amplitude of applied air pressure.

Table 3
d_{31} coefficients as a function of radial location on the surface of a wafer

Radius (mm)	d_{31} (pC/N)	P_r (ave.) (μC/cm^2)
2.4	−43	24
11.3	−40	21
11.3	−40	20
14.0	−44	20
16.4	−40	23
17.6	−46	21
19.5	−36	22

the consistency of the stress analysis for the wafer flexure technique. Different test capacitors on the surface of a 3 in. wafer were poled with +10 V for 10 min and allowed to stabilize for 10 min after removal of the poling field. Data collected were then correlated to the average remanent polarization (calculated from $+P_r$ and $-P_r$) for each capacitor tested. Results are given in Table 3 as a function of distance from the center of the wafer. From the data it is apparent that measured d_{31} values are independent of surface location.

7. Comments on the wafer flexure technique

The wafer flexure technique described is amenable to the rapid characterization of the transverse piezoelectric coefficient (d_{31}) of PZT thin film materials. Empirical results are in good agreement with other published values. In particular this method results in a significant reduction of cost, complexity, and the time needed to make d_{31} measurements. Furthermore, samples used are uncut silicon substrates, which eliminates the need to fashion millimeter-sized cantilever beams or diaphragms. A drawback to the uniform pressure method is its reliance on mathematical models which, to yield correct results, require explicit knowledge of the dimensions of the substrate, support housing, and test capacitor location. These factors, when coupled with the lack of data on the Young's modulus and Poisson's ratio for PZT thin films, limit the accuracy with which the transverse piezoelectric coefficient might be characterized. Additional details on calibration of this technique will be reported in a forthcoming paper [19].

Acknowledgements

The authors would like to acknowledge Tao Su for his assistance in depositing the PZT films used in this study. The work presented here was funded under DARPA contract DABT63-95-C-0053.

References

[1] P. Muralt, A. Kholkin, M. Kohli, T. Maeder, N. Setter, Characterization of PZT thin films for micromotors, Microelectron. Eng. 29 (1995) 67–70.
[2] D.L. Polla, L.F. Francis, Ferroelectric thin films in microelectromechanical applications, MRS Bull., July, 1996, pp. 59–65.
[3] A.L. Kholkin, C. Wutchrich, D.V. Taylor, N. Setter, Interferometric measurements of electric field-induced displacements in piezoelectric thin films, Rev. Sci. Instr. 67 (1996) 1935–1941.
[4] K. Lefki, G.J.M. Dormans, Measurement of piezoelectric coefficients of ferroelectric thin films, J. Appl. Phys. 76 (1994) 1764–1767.
[5] Q.M. Zhang, W.Y. Pan, L.E. Cross, Laser interferometer for the study of piezoelectric and electrostrictive strains, J. Appl. Phys. 63 (1988) 2492–2496.
[6] W.Y. Pan, L.E. Cross, A sensitive double beam laser interferometer for studying high-frequency piezoelectric and electrostrictive strains, Rev. Sci. Instr. 60 (1989) 2701–2704.
[7] J.F. Li, P. Moses, D. Viehland, Simple, high-resolution interferometer for the measurement of frequency-dependent complex piezoelectric responses in ferroelectric ceramics, Rev. Sci. Instr. 66 (1995) 215–221.
[8] M.O. Eatough, D. Dimos, B.A. Tuttle, W.L. Warren, A study of switching behavior in Pb(Zr,Ti)O_3 thin films using X-ray diffraction, Mater. Res. Soc. Symp. Proc. 361 (1995) 111–116.
[9] J.F. Shepard Jr., S. Trolier-McKinstry, M.A. Hendrickson, R. Zeto, Properties of PZT thin films as a function of in-plane biaxial stress, Proceedings of the 10th International Symposium on Applications of Ferroelectrics, New Brunswick, NJ, 1996, Vol. 1, pp. 161–165.
[10] M. Sakata, S. Wakabayashi, H. Goto, H. Totani, M. Takeuchi, T. Yada, Sputtered high-d_{31}-coefficient PZT thin film for micro actuators, Proceedings of the 9th Annual International Workshop on Micro Electro Mechanical Systems, San Diego, CA, 1996, pp. 263–266.
[11] M. Toyama, R. Kubo, E. Takam, K. Tanaka, K. Ohwada, Characterization of piezoelectric properties of PZT thin films deposited on Si by ECR sputtering, Sensors and Actuators A 45 (1994) 125–129.
[12] A. Ugural, Stresses in Plates and Shells, McGraw-Hill, 1981.
[13] R.J. Roark, W.C. Young, Formulas for Stress and Strain, 6th edn., McGraw-Hill, New York, 1989.
[14] W.A. Brantley, Calculated elastic constants for stress problems associated with semiconductor devices, J. Appl. Phys. 44 (1973) 534–535.
[15] J. Schweitz, Mechanical characterization of thin films by micromechanical techniques, MRS Bull., July, 1992, pp. 34–45.
[16] P. Luginbuhl, G.-A. Racine, P. Lerch, B. Romanowicz, K.G. Brooks, N.F. de Rooij, P. Renaud, N. Setter, Piezoelectric cantilever beams actuated by PZT sol–gel thin film, Sensors and Actuators A 54 (1996) 530–535.
[17] S. Watanabe, T. Fujiu, T. Fujii, Effect of poling on piezoelectric properties of lead zirconate titanate thin films formed by sputtering, Appl. Phys. Lett. 66 (1995) 1481–1483.
[18] T. Tuchiya, T. Itoh, G. Sasaki, T. Suga, Preparation and properties of

piezoelectric lead zirconate titanate thin films for microsensors and microactuators by sol–gel processing, J. Ceram. Soc. Jpn. 104 (1996) 159–163.
[19] J.F. Shepard Jr., S. Trolier-McKinstry, to be submitted to Sensorsand Actuators (1998).
[20] K.D. Budd, S.K. Dey, D.A. Payne, Sol–gel processing of $PbTiO_3$, $PbZrO_3$, PZT and PLZT thin films, Br. Ceram. Proc. 36 (1985) 107–121.

Biographies

Joseph F. Shepard Jr. is a doctoral candidate in Materials Science and Engineering at the Pennsylvania State University. He received his bachelor's degree in Mechanical Engineering from Syracuse University in 1992 and a masters degree in Materials Science from Penn State in 1995. His current research interests include the deposition and characterization of piezoelectric/ferroelectric thin films for utilization in microelectromechanical systems.

Paul Moses is a senior research assistant in the Materials Research Laboratory of the Pennsylvania State University. His focus is the construction of electronic equipment for the fabrication and characterization of ferroelectric materials. He holds a bachelor's degree in Mathematics from Penn State and has worked for universities and private companies in countries as far west as China and as far east as Switzerland.

Susan Trolier-McKinstry is an assistant professor in the Materials Science and Engineering Department at the Pennsylvania State University with a joint appointment with the Intercollege Materials Research Laboratory. Her main research interests include ferroelectric thin films for actuator applications, the development of texture in bulk ceramic piezoelectrics, and spectroscopic ellipsometry. She is a member of the American Ceramic Society, the Materials Research Society, and the IEEE. In the past few years she has helped organize MRS symposia on Materials for Smart Systems and the International Symposium on Applications of Ferroelectrics.

APPENDIX 69

Journal of the Korean Physical Society, Vol. 32, February 1998, pp. S1464~S1467

Stress-dependent Piezoelectric Properties of Ferroelectric Lead Zirconate Titanate Films Studied by Atomic Force Microscopy

Genaro ZAVALA
Dept. of Physics, ITESM, Campus Monterrey, Monterrey 64849, Mexico

Janos H. FENDLER
Dept. of Chemistry, Clarkson University, Potsdam, NY 13676, USA

Susan TROLIER-MCKINSTRY
Mat. Res. Lab., The Pennsylvania State University, University Park, PA 16802, USA

Atomic force microscopy (AFM) has been used for the determination of piezoelectric properties of lead zirconate titanate (PZT) films in the morphotropic phase boundary composition. An AFM tip was used, in the contact mode, as a top electrode to apply a voltage to polarize the film and to apply an oscillating field to obtain piezoelectric coefficients and piezoelectric loops from the inverse piezoelectric effect induced on the film. The piezoelectric coefficient in nanoregions was measured as a function of stress by changing the applied force with the AFM tip. The piezoelectric coefficient was found to decrease monotonically as the stress was increased. It was additionally found that as the stress was decreased to its initial value, the effective piezoelectric coefficient approximately followed the same trace on increasing the stress. These results suggested that non-180° domains did not contribute to the measured piezoelectric coefficient for the stress levels applied and that the mobility of ferroelastic domain walls is very low for these PZT films.

I. INTRODUCTION

The research on ferroelectric thin films receives substantial support from industries which hope to exploit them in applications in diverse areas such as computer memories [1], phones [2] and electromechanical devices [3]. Ferroelectric films are interesting per se, since their behavior is not completely understood and their properties, given their sub-micron thickness, are size dependent [4]. An understanding of the size-dependence of ferroelectric materials may result in the improvement of their properties to be similar to the bulk ferroelectrics.

The present work study the characterization of lead zirconate titanate (PZT) films by the AFM. PZT was chosen as the focus of study since this material has been one of the most studied in the ferroelectric field. It has excellent ferroelectric properties and those properties can be controlled by changing the ratio of composition between lead titanate and lead zirconate.

II. EXPERIMENTAL PROCEDURES

Lead zirconate titanate, $Pb(Zr_{0.52}Ti_{0.48})O_3$ (PZT), films were prepared by using a modified [5] version of the sol-gel process described by Budd, Dey, and Payne [6].

The AFM system was supplemented by an EG&G PARC 5301 lock-in amplifier, a Hewlett Packard PS116A pulse/function generator, a Mitsubishi 386 microprocessor computer, and a Hewlett Packard 54510A digitizing oscilloscope to perform piezoelectric measurements (see Fig. 1). Grounded silicon tips (with a spring constant

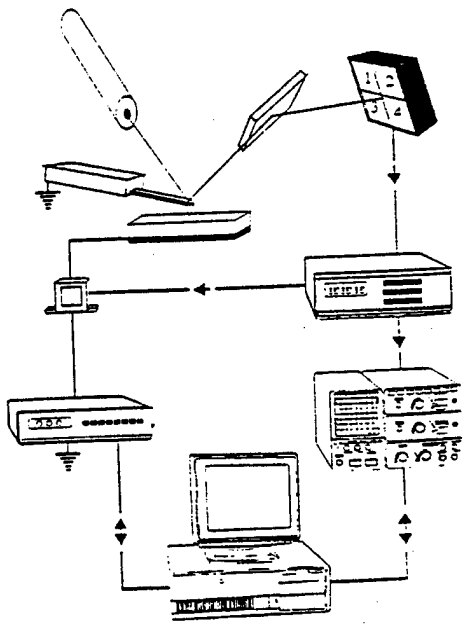

Fig. 1. The AFM system was supplemented by a lock-in amplifier, a pulse/function generator, a computer, and a digitizing oscilloscope to perform piezoelectric measurements. The internal reference signal of the lock-in amplifier is used as ac signal and is applied to the substrate.

of 50 N/m were used. The tip was brought into feedback position in the contact mode. The position of the reflected beam on the cantilever surface was detected by a four-segment detector. The signal (1–2)-(3+4) which detected any vertical movement, was taken to the lock-in amplifier. The amplifier internal signal reference (at 5 kHz) was applied to the bottom electrode of the film through a transformer to drive mechanical movements (i.e., from piezoelectric response) on the film. The signal applied to the bottom electrode from the transformer was 0.5 Vrms. The frequency (5 kHz) was fast enough not to interfere with the feedback loop and smaller than the resonance frequency of the cantilever. To polarize the film, a signal either from the function generator or a dc power supply was applied to the bottom electrode.

A piezoelectric loop was obtained in a computer controlled experiment. The computer controlled the magnitude of a step voltage signal produced by the generator (see Fig. 1). This signal was applied to polarize the film. The magnitude was changed in each cycle by two volts from -16 V to −16 V and from −16 V to -16 V. In each step, when the voltage was zero, the computer saved the magnitude and phase of the piezoelectric response. The results were plotted in a ferroelectric-loop style curve.

The area of interaction between the tip and the film was assessed by sensing the piezoelectric behavior as a function of distance from the polarization point. After applying the polarization voltage, the piezoelectric response was measured at different distances from the polarization point.

The effect of stress was determined by changing the force applied by the silicon tip on the surface. The tip was brought into the contact mode and a dc voltage was applied to polarize the area. Then an ac signal was applied to drive mechanical movements of the film. As the piezoelectric response was measured, the force applied to the film by the tip was changed from 2.5 to 28.5×10^{-6} N. In addition, the piezoelectric response was measured as the force was decreased to its original value.

III. RESULTS AND DISCUSSION

In the experiment, the AFM tip was used as a top electrode. The film was positively and negatively polarized in different regions. When the ac signal was applied, the tip oscillated following the change in film thickness. In a positive polarization region, the positive part of the ac signal increased the thickness, so the detected signal was in phase with the ac signal. In a negatively polarized region, the positive part of the ac signal decreased the thickness, so the detected signal was 180° out of phase with respect to the ac signal.

The piezoelectric response was measured for different polarization voltages (see Fig. 2). For each measurement, the piezoelectric constant (d) was set to be negative when the phase obtained was 180° and positive when the phase obtained was 0°, indicating the main orientation of the domains. The resulting curve had all the features of a hysteresis loop: d-values came to a saturation point around 13 V and the coercive voltage (V_c) was around 3-4 V. The difference between the present measurements and a similar loop obtained elsewhere [7] was that the present loop was taken with no dc voltage applied. It is important to point out that all piezoelectric measurements using the AFM tip were taken with just the ac signal applied. A dc voltage was applied to polarize the film but it was reduced to zero for each piezoelectric measurement. Therefore, the actual remanent piezoelectricity was measured since this experiment did not have any additional interactions produced by a dc field, such as an additional stress [8].

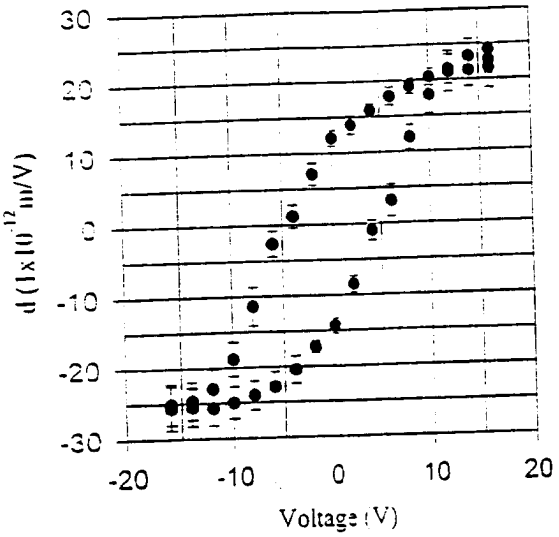

Fig. 2. Piezoelectric loop taken by measuring the vibration of the tip at a frequency of an applied ac signal. The loop was taken at least three times to obtain the average value with error bars.

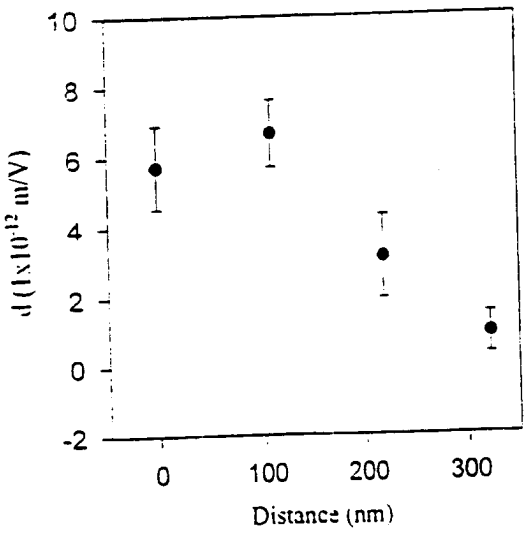

Fig. 3. Piezoelectric response as a function of distance from the point of polarization. Note that d increases to a maximum and then decreases to zero.

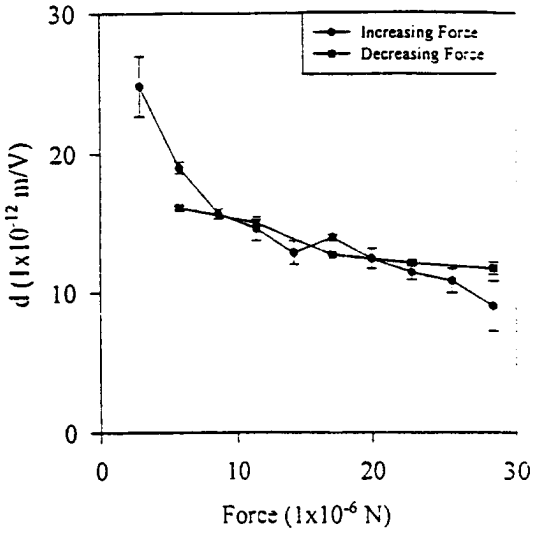

Fig. 4. Piezoelectric response change with force applied by the tip. As the force is increased, d decreases monotonically. As the force is decreased back, d increases approximately the same way it decreased.

The size of the interaction area accessed by the AFM tip was established by determining the piezoelectric constant as a function of distance from the polarization point (see Fig. 3). The area of interaction was found to have a radius of around 250 nm. This area can be related either to the effective tip radius or to the film thickness [9]. An interesting behavior in Fig. 3 was that the d-value first increased and then decreased to zero as the tip was moved away from the poling position. This behavior could be related to stress. At the point of polarization, where the dc voltage was applied, the stress exerted was greater than that on areas nearby where the contact was made just for the measurement of the piezoelectric response. This greater stress was due to the applied additional stress on the film produced by the dc voltage [8].

In order to investigate the role of stress in the piezoelectric response, the effective piezoelectric coefficient d was measured at different values of the contact force. A silicon tip was used to perform these measurements. The tip was brought to the contact mode and -16 volts was applied to polarize the film. Once the film was polarized, the piezoelectric response was measured. The AFM system has the capability to change the force applied with the tip to the surface.

Measuring d for different forces and plotting all the results in one graph, Fig. 4 was obtained. The data in Fig. 4 show a monotonic decrease in the measured d-values with increasing stress over the range measured. It was found that increasing the constant force from 4 N to 28 N leads to an approximately 60% drop in the measured effective d value.

It is interesting to compare these data to similar work on bulk ceramics exposed to uniaxial stresses. To do so, as a first approximation it was assumed that the contact force was applied over an area of ~400 - 500 nm in diameter (see Fig. 3), and that the loading could be treated as roughly uniaxial. The resulting compressive stress for the higher contact force is thus ~140 - 220 MPa. The film was also assumed to behave much like a hard PZT ceramic, as it is undoped. Many publications on the stress dependence of piezoelectric properties have been reported; the work of Zhang *et al.* [10], was chosen here for comparison. These authors report that for hard PZT compositions the d-value initially increases as uniaxial pressure is applied, it then goes through a maximum, and subsequently decreases for stress levels of 150 MPa. The enhanced d observed at modest stress levels was attributed to deaging the ceramic sample, so that non-180° domain walls were freed to contribute to the observed response. The fact that this was not observed in the thin undoped PZT films measured in this study implies that it was not possible to engender appreciable non-180° domain wall motion for the stress levels applied. The observed decrease in the piezoelectric response of the material under load could then be attributed to either a shift in the morphotropic phase boundary composition with stress or to clamping of the response by the applied stress.

Another interesting point apparent in Fig. 4 is that on decreasing the load, the effective piezoelectric coefficient of the films approximately retraces the curve measured on increasing load. In soft PZT ceramics loaded parallel to the poling direction, there is appreciable hysteresis in the piezoelectric coefficients on unloading after application of a large uniaxial stress due to domain reorientation [10,11]. That is, domains which were originally parallel to the applied load can be reoriented ferroelastically under stress. On removing the stress, there is little driving force to restore these domains to their original configuration. As a result of the decrease in the remanent polarization, the measured d value also decreases hysteretically. Hard PZT ceramics show less ferroelastic depoling and hysteresis, since the local defect dipoles act to stabilize the domain structure. In this work, even accounting for the approximations inherent in the stress calculations for the AFM measurements on films, the observed non-hysteretic film response measured here strongly suggests that twin walls are immobile in these films. This is in agreement with measurements made on similar sol-gel PZT films exposed to large in-plane biaxial stresses [12]. It is also interesting that a decrease in the twin wall mobility is observed in bulk PZT ceramics as the grain size is reduced below 1 μm [13,14]. Thus, in the thin films, where the grain size is typically under 0.1 μm, it is not surprising that low domain wall mobilities are observed. In any event, it is clear that in order to measure the effective d coefficient of films using the AFM, it is preferable to use minimal loading conditions. This is consistent with the observation of Gruverman *et al.* [15], that piezoelectric coefficients measured by AFM should be performed at low loads.

IV. CONCLUSION

The piezoelectric coefficient of ferroelectric films was

measured by the AFM tip. Piezoelectric loops provided information on saturation voltages and coercive voltages which agreed well with values measured in the macroscopic scale.

The areas of piezoelectric interaction were measured in this study. These areas, related to the size of the tip and the thickness of the film, were in the submicron range.

A study of piezoelectric coefficient as a function of applied stress was performed. The piezoelectric coefficient decreased monotonically as the stress was increased. As the stress was decreased, the piezoelectric coefficient did not show hysteresis. Therefore, the following conclusions can be inferred from these results:

It was proven in the present work that piezoelectric measurements can be performed by AFM on nanodomains and piezoelectric measurements by AFM should be performed at low loads.

It was also shown that non-180° domain walls do not contribute appreciably to the measured piezoelectric response at any level of applied stress and that the mobility of the domain walls is low.

REFERENCES

[1] H. Koike, T. Otsuki, T. Kimura, M. Fukuma, Y. Hayashi, Y. Maejima, K. Amamuma, N. Tanabe, T. Matsuki, S. Salto, T. Takeuchi, S. Kobayashi, T. Kunio, T. Hase, Y. Miyasaka, N. Shomata and M. Takada, Proceedings of the ISSCC (1996).

[2] C. Paz de Araujo, J. F. Scott and G. W. Taylor, in *Ferroelectric Thin Films: Synthesis and Basic Properties*, edited by C. Paz de Araujo, J. F. Scott and G. W. Taylor (Gordon and Breach Publishers, 1996), p. 1.

[3] W. Tjhen, T. Tamagawa, C. -P. Ye, C. -C. Hsueh, P. Schiller and D. L. Polla, Proceedings of the 4th IEEE Workshop on Micro-Electro-Mechanical Systems (MEMS '91) (Nara, Japan, 1991), p. 114.

[4] R. E. Newnham, K. R. Udayakumar and S. Trolier-McKinstry, in *Chemical Processing of Advanced Materials* (John Wiley and Sons, Inc., 1992), p. 379.

[5] The process was modified by Dr. Susan Trolier-McKinstry's group, at the Pennsylvania State University and the films were made by Dr. Pavadee Aungkavattana.

[6] K. D. Budd, S. K. Dey and D. A. Payne, Electrical Ceramics, British Ceram. Soc. Proc. **36**, 107 (1985).

[7] H. Birk, J. Glatz-Reichenbach, Li-Jie, E. Schreck and K. Dransfeld, J. Vac. Sci. Technol. B **9**, 1162 (1991).

[8] K. Franke, Ferroelectrics Lettters, Section 19, 35 (1995).

[9] P. Guthner and K.Dransfeld, Appl. Phys. Lett. **61**, 1137 (1992).

[10] Q. M. Zhang, J. Z. Zhao, K. Uchino and J. H. Zheng, J. Mat. Res. **12**, 226 (1997).

[11] H. A. Krueger, J. Am. Acous. Soc. **42**, 636 (1967).

[12] J. F. Shepard Jr., S. Trolier-McKinstry, M. A. Hendrickson and R. Zeto, to be published in Proceedings of the International Symposium on the Applications of Ferroelectrics (East Brunswick, NJ, 1996).

[13] W. Cao and C. A. Randall, J. Phys. Chem. Sol. **57**, 1499 (1996).

[14] N. Kim, Ph. D. Thesis (The Pennsylvania State University, 1994).

[15] A. Gruverman, O. Auciello and H. Tokumoto, J. Vac. Sci Technol. B **14**, 602 (1996).

APPENDIX 70

Journal of the Korean Physical Society, Vol. 32, February 1998, pp. S1344~S1348

Continuous Single Crystal $PbTiO_3$ Thin Films Epitaxially Grown on Miscut (001)$SrTiO_3$

Kiyotaka WASA and Yoko HANEDA
Research Institute of Innovative Technology for the Earth (RITE), Kyoto 619-02, Japan

Toshifumi SATOH, Hideaki ADACHI, Isaku KANNO and Kentaro SETSUNE
Central Research Laboratories, Matsushita Electric Co. Ltd., Kyoto 619-02, Japan

Darrell G. SCHLOM and S. TROLIER-MCKINSTRY
Materials Research Institute, Pennsylvania State Univ., University Park, PA 16802, USA

Chang-Beom EOM
Department of Mechanical Engineering and Materials Science, Duke Univ., Durham, NC 27708-0300, USA

Continuous single crystal (001)$PbTiO_3$ (PT) thin films, 5 to 300 nm in thickness, were epitaxially grown on miscut (001)$SrTiO_3$ (ST), miscut angle 1.7 degree, by rf-planar magnetron sputtering. The surface of the miscut substrates comprised periodic striped patterns with periodic step lines and terraces; the step height was 0.4 nm and terrace width was 14 nm. The surface of PT thin films also comprised periodic striped patterns; the step height was 1 to 3 nm and the terrace width was 50 to 150 nm. The film growth was governed by a step-flow growth with step-bunching. The layer growth mode of Frank-van der Merwe type was predominant and the surface was extremely flat on an atomic scale. The resultant epitaxial films showed a single crystal/single c-domain structure. Epitaxial growth on miscut substrate is essential to fabricate perovskite thin films with controlled microstructure.

I. INTRODUCTION

Thin films of perovskite ceramics (ABO_3) have been extensively studied, since compound perovskite, $(A1,A2)(B1,B2)O_3$, shows a series of interesting and useful properties associated with the structural system [1]. Several deposition processes have been used for the deposition of perovskite ceramics including thermal evaporation, sputtering, laser ablation, and chemical vapour deposition. Among these deposition processes, sputtering is now widely used for the deposition of perovskite ferroelectric ceramics. Continuous single crystal/single domain thin films of perovskite materials are important not only for the fabrication of layered perovskite thin film devices but also understanding of their physical and/or chemical properties. However, most of the perovskite thin films include non-homogeneous microstructures, even if the films show three-dimensional epitaxy. Systematic studies on a deposition of basic perovskite such as PT are essential for an achievement of a fine control of the microstructure [2]. This paper will describe the basic deposition parameters for the control of microstructure and overview recent experiments on the sputtering deposition of PT thin films with controlled microstructures to achieve a deposition of continuous single crystal/single domain PT thin films.

II. BASIC DEPOSITION PARAMETERS

Thin films of perovskite structure are provided by a heteroepitaxial growth on foreign single crystal substrates. The epitaxial films essentially include dislocation and/or microstructures due to the thermal and/or lattice mismatch between thin films and the substrates.

Table 1 shows typical substrates for the epitaxial growth. The ST substrate shows a small lattice mismatch for the growth of c-domain perpendicular to the substrate (lattice mismatch, 0.05%). Large lattice mismatch for the growth of c-domain, i.e. PT on MgO (lattice mismatch, 7%) will induces a growth of dislocation and/or multi-domains above a critical film thickness in order to release the stress in the epitaxial films [3]. The critical

Table 1. Lattice parameters of PT and substrtes.

	Crystal system	Structure	Lattice constant at RT (Å)	Thermal expansion (1/K)
				ppm
$PbTiO_3$	tetra.	perovskite	a=3.903 c=4.152	16.1 54.2
MgO	cubic	NaCl	a=4.203	13.8
$SrTiO_3$	cubic	perovskite	a=3.905	10.8
$LaAlO_3$	pseudo cubic	perovskite	a=3.792	10
Sapphire	trigonal	corundum	a=4.763	7.7-8

film thickness is about 100 nm [4]. The non-uniformity of initial crystal growth also induces the microstructures including multi-domain growth [5]. Uniform layer growth with a small lattice mismatch under stoichiometric composition will be essential for the deposition of continuous single crystal perovskite thin films with single domain [6].

The epitaxial temperature of perovskite thin films is typically 500 to 600 °C. The lattice deformation accompanied by the growth of microstructures will be enhanced during the cooling period from the epitaxial temperature to a room temperature after a film deposition, when the epitaxial temperature T_e is higher than the Curie temperature T_c (PT: $T_e > T_c$, T_c=490 °C). The cooling rate will change the populations of a-domain and/or c-domain in the films [7].

III. DEPOSITION AND MEASUREMENTS

PT thin films were epitaxially grown on (001)ST substrate by rf-planar magnetron sputter. PT powder target was used for the deposition. The chemical composition of the sputtered films is controlled by the composition of the powder target. Miscut ST substrates with miscut angle of 0.2 to 10 degrees were used for the epitaxial growth. Typical sputtering conditions are shown in Table 2. Sputtered thin films were cooled down to 200 °C within 30 minutes. Microstructures were evaluated by XRD (X-ray diffraction), SEM (scanning electron microscopy), TEM (transmission electron microscope) along with SAD (selective area diffraction) analysis, and AFM (atomic force microscope) [8]. The dielectric properties of PT thin films were evaluated at the sandwich structure, Au/PT/$SrRuO_x$/ST, using conducting $SrRuO_x$ (SRO) layer. The dielectric measurements were conducted by sine wave at 1 kHz with the Au counter electrode of 0.3 mm in diameter deposited by vacuum evaporation. The SRO layer was epitaxially deposited on the ST substrates by off-axis sputtering [9].

IV. RESULTS AND DISCUSSION

1. Microstructures

a. PT Films on (001)ST

Table 2. Sputtering conditions.

Sputter system	Rf-planar magnetron
Target	$PbTiO_3$ powder
Target diameter	80 mm
Target-substrate spacing	30 mm
Substrate	(001)$SrTiO_3$, miscut (001)$SrTiO_3$
Substrate position	on axis
Substrate temperature	600 °C
Sputtering gas	Ar/O_2=20/1-2/1 (0.5 Pa)
Growth rate	3 nm/min
Film thickness	5-300 nm

Below a critical thickness, thin films could exhibit uniform crystal growth without any microstructure, if the thin films will uniformly grow on an atomic scale. The critical thickness is around 100 nm. To confirm this consideration first we tried to deposit ultra-thin films of PT on the well-oriented ST substrate under epitaxial growth conditions. Stoichiometric composition was kept throughout the experiments so as to suppress the formation of secondary phases during film growth. X-ray diffraction analysis suggests that the films exhibit highly c-axis oriented single crystals with the epitaxial relation, (001) PT/(001) ST. The surface SEM image indicates the presence of microstructures comprising island structure at the initial stage of film growth probably due to the three-dimensional nucleation. The microstructures have grown as the film thickness increases under Volmer-Weber mode. When the film thickness reached a critical value, i.e., 100 nm, a sharp crack was developed. The formation of the microstructures may result from the release of stress in the thin films. Two-dimensional nucleation will be essential for making uniform film growth.

b. PT Thin Films on Miscut (001)ST

The miscut substrate will provide uniform nucleation centers. Typical value of miscut angle was 1.7 degree. The direction of miscutting was parallel to <010> ST. Surface model of the miscut ST is shown in Fig. 1. Surface crystal steps will act as a nucleation center. The surface comprises step lines and terraces. The height of the steps is around 0.4 nm corresponding to a crystal unit of ST substrate [10]. The average terrace width is 14 nm for the miscut angle of 1.7 degree. Figure 2 shows typical surface SEM images of sputtered PT thin films on the miscut ST substrates for various miscut angles. The surface comprises periodic striped patterns. The spacing of the periodic patterns decrease with increasing the miscut angles. Typical spacing for the miscut angle of 1.7 degree was 50 to 150 nm. X-ray diffraction analysis suggests that these PT thin films on miscut ST substrates are highly c-axis oriented single crystal. The cross sectional TEM image of the sputtered PT thin film on the miscut ST substrate with SAD pattern and sur-

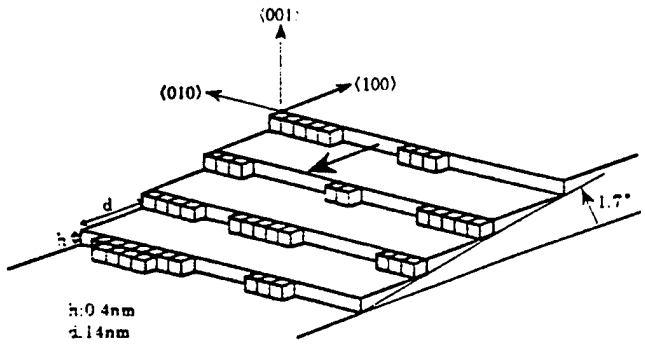

Fig. 1. Typical surface model of miscut (001)ST substrate; miscut angle, 1.7 degree.

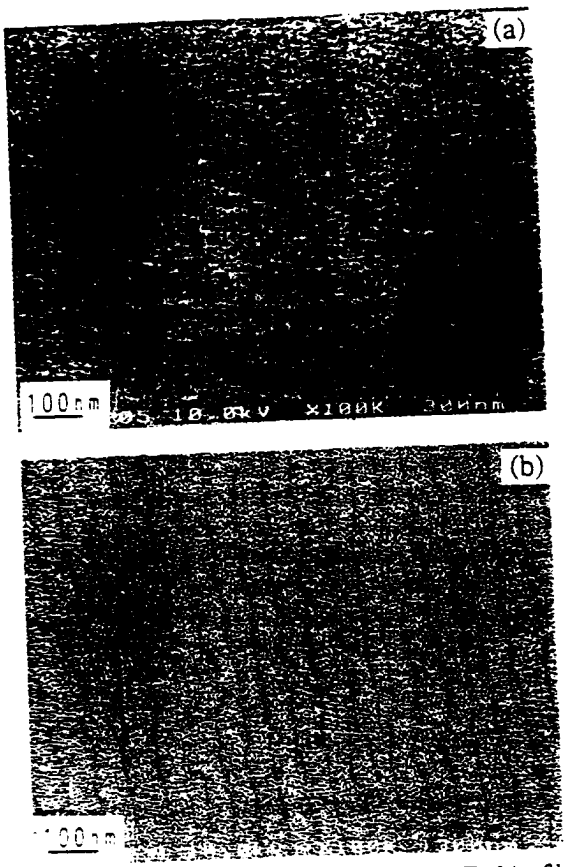

Fig. 2. Typical SEM images of sputtered PT thin films on miscut (001)ST for various miscut angles; (a) 1.7 degree, (b) 5.0 degree. Pt thin films, 100 nm in thickness.

face lattice image of the PT thin film are shown in Fig. 3. The surface of the terrace was atomically smooth. The step height was 1 to 3 nm. These results suggested that the film growth on the miscut ST substrates was governed by a layer growth of step-flow growth mode. At the initial stage of film growth, film thickness <10 nm, step bunching was observed. Both terrace width and step height increased with film thickness [11]. The SAD pattern shows the films epitaxially grown with the epitaxial relation of (001)PT // (001)ST. The PT thin films comprise c-domain structure and are coherent to the substrates.

Domain stability has been studied in detail by Speck *et al.*. Population of a-domain and c-domain are governed by the substrate lattice and thermal mismateh, cooling rate, and depolarizing field [7]. The present experiments suggest that the control of initial film growth is effective to make uniform PT thin films with single crystal/single domain structure.

The step-flow growth mode is essentially governed by the surface diffusion of adatoms on the terrace. Higher mobility of adatoms and/or narrow width of terrace will stabilize the step-flow growth mode. The commercially available well-oriented ST substrates also include crystal steps and terraces, since the error of crystal cutting angle is generally ±0.3 degree which corresponding the terrace width of >80 nm. At present deposition condition the terrace width, >80 nm, will be so long that the step-flow growth mode could not be stabilized. The critical miscut angle, i.e. minimum miscut angle, 0.9 to 1.7 degree [12]. The stability of the layer growth of step-flow growth mode was affected by the partial oxygen pressure during film growth. The higher oxygen partial pressure during the sputtering will prevent the two-dimensional nucleation accompanied by layer growth and induces the three-dimensional crystal growth as shown in the SEM images of Fig. 4: (a) Ar/O_2=20/5, two-dimensional crystal growth, (b) Ar/O_2=20/6, (c) Ar/O_2=20/7, three-dimensional crystal growth. A critical partial oxygen pressure was present for the layer growth.

2. Lattice Structures

Heteroepitaxial films show three types of lattice deformation: relaxed, strained, and/or dislocated lattice deformation. Thick films usually show relaxed and/or dislocated type. Ultrathin films, thickness less than a critical thickness, show strained lattice deformation. At the growth temperature cubic PT (a=0.397 nm) films are epitaxially grown on ST (a=0.393 nm) under a compres-

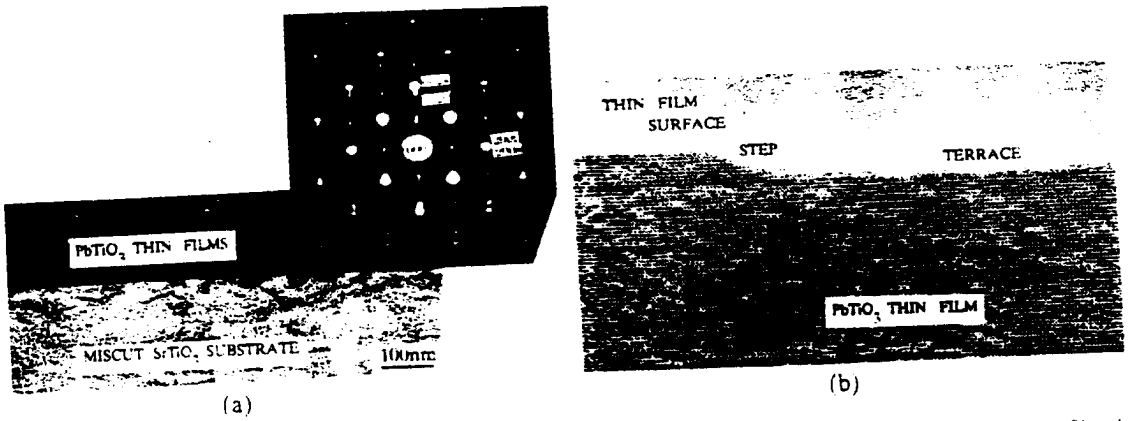

Fig. 3. Cross sectional TEM image of sputtered PT thin films on miscut (001)ST with SAD pattern at film/substrate interface (a), lattice image of film surface (b). PT thin film, 160 nm in thickness.

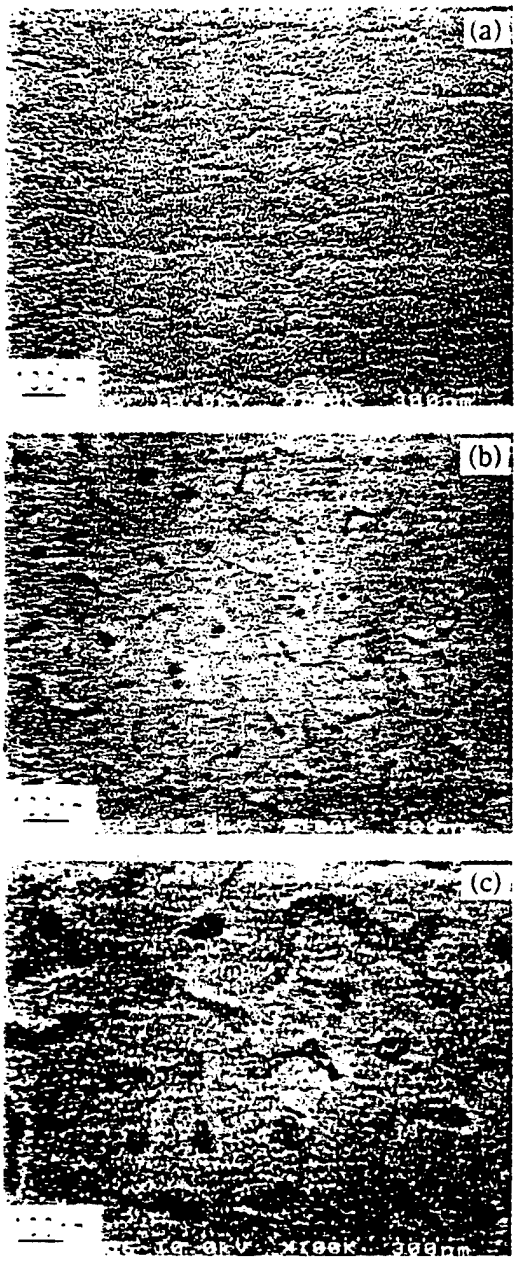

Fig. 4. Surface SEM images of sputtered PT thin films on miscut (001) ST for various oxygen partial pressure during the sputtering deposition: (a) Ar/O_2=20/5, (b) Ar/O_2=20/6, (c) Ar/O_2=20/7. PT thin films, 120 nm in thickness.

sive force due to the lattice mismatch. The unit cell of PT thin films will be prolonged. The compressive force will be maximum at the growth temperature, since a-lattice mismatch will decrease due to the difference of thermal expansion coefficient. During the cooling stage c-domain stabilization will be further enhanced due to the intrinsic phase transition from cubic to tetragonal phase at T_c, resulting in large tetragonal deformation c/a=1.06 to 1.1 at room temperature [13].

X-ray analysis suggested that the thin films comprise a single c-domain structure, even if the film thickness increases up to 300 nm. The PT thin films are continuous structure without any grain boundary. The PT thin films are extremely smooth. The X-ray diffraction patterns include satellite oscillation due to Pendellosung Fringes. The PT thin films will be tightly bonded onto the substrate, so the PT thin films show a small variation of c- and/or a-lattice parameters over Curie temperature [14]. The PT thin films showed excellent dielectric properties with low loss factor; room temperature dielectric constant ε_r=70, loss factor tanδ <1%, remanent polarization P_r=30 $\mu C/cm^2$, and pyroelectric coefficient $\gamma=3\times10^{-8}$ C/cm^2K. The large pyroelectric coefficient indicates that the PT thin films comprise mono-polar c-domain without 180 degree domain [15].

V. CONCLUSION

Deposition of PT on a miscut ST substrate induces step-flow growth mode and realizes a layer growth. The resultant PT thin films show a continuous single crystal/single c-domain structure, although the films show strained deformation. The thickness of the continuous single crystal films is up to 300 nm. The PT thin films do not include 90 and/or 180 degree domain. It is confirmed that the epitaxial growth on miscut substrates is essential to fabricate perovskite thin films with controlled microstructures. It is also noted that a basic planar rf-diode magnetron sputtering is available for the deposition of perovskite thin films with controlled microstructures on an atomic scale.

ACKNOWLEDGMENTS

The authors thank Prof. E. Cross, R. Roy, R. E. Newnham, K. Uchino (Penn State Univ.) for their helpful discussion, Dr. J. Kondo (RITE) for his continuous encouragement.

REFERENCES

[1] G. H. Haertling and C. E. Land, J. Am. Ceram. Soc. **54**, 1 (1971).
[2] K. Wasa, H. Adachi and M. Kitabatake, Proc. of IMF-8 (Washington DC, 1993), in Ferroelectrics **151**, 1 (1994).
[3] B. S. Kwak, A. Erbil, B. J. Wilkens, J. D. Budai, M. F. Chisholm and L. A. Boatner, Phys. Rev. Lett. **68**, 3733 (1992).
[4] C. D. Theis, *Thesis for Master of Science* (Penn State Univ., 1996), p. 104.
[5] K. Wasa, T. Sato, K. Tabata, H. Adachi, Y. Yabuuchi and K. Setsune, J. Mater. Res. **9**, 2959 (1994).
[6] K. Wasa, H. Adachi, Y. Ichikawa, K. Hirochi, T. Matsushima, A. Enokihara, K. Mizuno, H. Higashino and K. Setsune, *Science and Technology of Thin Film Superconductor 2*, ed. by R. D. McConnel and R. Noufi (Prenum, N. Y., 1990), p. 1.
[7] J. S. Speck and W. Pompe, J. Appl. Phys. **76**, 466 (1994).
[8] T. Sato, K. Wasa, K. Tabata, H. Adachi, Y. Ichikawa

and K. Setsune, J. Vac. Sci. Technol. **A13**, 1022 (1995).

[9] C. B. Eom, R. J. Cava, R. M. Fleming, J. M. Phillips, R. B. van Dover, J. H. Marshall, J. W. P. Hsu, J. J. Krajewski and W. F. Peck Jr, Science **258**, 1766 (1992).

[10] K. Wasa, T. Sato, H. Adachi, K. Setsune and S. Trolier-McKinstry, Proc. of 3rd ISSP, 1995, Tokyo (unpublished), p. 85.

[11] K. Wasa, T. Sato, H. Adachi, K. Setsune, S. Trolier-McKinstry and Darrell G. Schlom, Mater. Res. Soc. Symp. Proc. **401**, 151 (1996).

[12] K. Wasa, Y. Haneda, T. Satoh, H. Adachi and K. Setsune, Proc. of 4th ISSP. 1997, Kanazawa (unpublished), p. 145.

[13] K. Wasa, T. Satoh, H. Adachi and K. Setsune, Intergated Ferroelectrics **12**, 93 (1996).

[14] K. Wasa, Y. Haneda, T. Satoh, H. Adachi and K. Setsune, J. Vac. Sci. Technol. **A15**, 1185 (1997).

[15] Eric Cross, private communication.

APPENDIX 71

Dielectric Hysteresis from Transverse Electric Fields in Lead Zirconate Titanate Thin Films

Baomin Xu[a)], Yaohong Ye, and L. Eric Cross

Materials Research Laboratory, Pennsylvania State University,

University Park, PA 16802

Jonathan J. Bernstein and Raanan Miller

The Charles Stark Draper Laboratory, 555 Technology Square,

Cambridge, MA 02139

[a)]Corresponding author. Electronic mail: bxx2@psu.edu

Abstract

Excellent symmetric dielectric hysteresis is observed from lead zirconate titanate (PZT) thin films using transverse electric fields driven by interdigitated surface electrodes. The 1 μm-thick PZT films with Zr/Ti ratio of 52/48 are prepared on ZrO_2 buffered, 4-inch diameter silicon wafers with a thermally grown SiO_2 layer. Both the ZrO_2 buffer layer and PZT film are deposited by using a similar sol-gel processing. Remanent polarization of about 20 $\mu C/cm^2$ with coercive field less than 40 kV/cm is obtained as measured using a triangle wave at 50 Hz. Thicker films are being developed and retention for the transversely polarized state is currently under study. One of the objectives of this study is to develop a large array of d_{33} driven unimorph sensing elements for a high resolution acoustic imaging system.

Because the d_{33} and k_{33} values of most ceramics are almost two times of the d_{31} and k_{31} values respectively,[1] recent studies in macroscopic systems have highlighted the strong advantages for unimorph bending actuators with transversely polarized PZT layer which can be driven electromechanically through the piezoelectric d_{33} mode rather than the conventional d_{31} mode.[2,3] Here the d_{33} mode means that both the polarization and applied field are along the surface of the piezoelectric layer (that is, transverse direction). This d_{33} unimorph structure should also be significant for MEMS (microelectromechnical systems) applications because many micromachined unimorph transducers for various MEMS devices have been developed by combining silicon microelectronics technology and on-chip ferroelectric lead zirconate titanate (PZT) films.[4,5,6] In addition, we believe the transverse polarization configuration will be more attractive for micromachined unimorph diaphragm pressure sensors, since diaphragm thickness and electrode spacing are now independent variables. Particularly important is the fact that newer field effect transistors are available with ultralow input capacitance, matching well the very low self-capacitance of the unimorph structures with wider electrode separation and consequently higher intrinsic voltage sensitivity. As a first step towards producing d_{33}-mode unimorph bending transducers on silicon substrates, ferroelectric PZT films have to be deposited on an insulating buffer layer with low dielectric constant instead of the conventional platinum buffer layer. In this letter we report that PZT thin films can be prepared on ZrO_2-buffered silicon substrates and strong symmetric hysteresis is observed for transverse fields generated from interdigitated surface electrodes, indicating the excellent ferroelectric properties of the films.

Both the ZrO_2 and PZT films were deposited by multiple sol-gel spin-on procedures, and their solutions were prepared using an acetic acid process modified from the former

reports in the literature.[7,8] To prepare ZrO_2 solution, zirconium n-propoxide was added to the glacial acetic acid and the mixture was refluxed at 105°C for 1 hour. Ethylene glycol and deionized water were also added during the reflux to control the viscosity and concentration of the solution. To prepare PZT (52/48) solution, lead acetate trihydrate, with 20 mol% excess lead content, was initially dissolved in acetic acid and the associated water was removed during a period of distillation at 150°C. After cooling to room temperature, zirconium n-propoxide and titanium isopropoxide were added to the solution and the mixture was refluxed at 80°C for 1 hour. Again ethylene glycol and deionized water were added during the reflux process. The concentrations of the final solutions were adjusted to be 0.75 M for the ZrO_2 solution and 0.90 M for the PZT solution. The substrate was 4 inch-diameter, n-type, (100) oriented silicon wafers with a 0.4 μm-thick thermally grown SiO_2 layer. For the preparation of ZrO_2 film, the samples were pyrolyzed at 600°C for 0.1 hour after the deposition of each layer and annealed at 700°C for 3 hours after the 5th layer deposition. After the annealing of ZrO_2 film, another 5 layers of PZT solution were coated layer by layer in the same way but the final annealing condition was changed to 700°C for 1 hour.

The phase structures of the films were analyzed by using an X-ray diffractometer and the results are shown in Fig. 1. It can be seen that the ZrO_2 film is mainly amorphous after annealing but the PZT film is well-formed perovskite structure phase. The peak with the highest intensity in the X-ray diffraction pattern of the PZT film is indexed as (101) plane, indicating that the film is mostly random-oriented. This is not surprising considering the PZT film was grown on an amorphous surface. The surface and cross-section microstructures of the films were studied under scanning electron microscopy (SEM) and the results are given in Fig. 2. The SEM surface micrograph of the PZT film

suggests a grain aggregate structure of 3 to 5 μm scale. but obvious sub-structure, and x-ray line broadening indicate that the true grain size is significantly smaller. The SEM cross-sectional microstructure (Fig. 2 (b)) shows the clear multilayer PZT, ZrO_2, SiO_2, Si structure and the very sharp interface between PZT and ZrO_2 films. The thicknesses of the PZT and ZrO_2 films are about 1 and 0.4 μm respectively. These results have verified that the ZrO_2 film can work as an effective buffer layer preventing the reaction and inter-diffusion between the PZT film and silicon substrate.

In order to measure the hysteresis loops under transverse electric field, the Ti/Pt/Au interdigitated electrodes were sputtered on the surface of the PZT film and a sketch map of the electrode patterns is shown in Fig. 3. A conventional photo-resister liftoff process was used to define the finger width of 10 μm and electrode separations (finger gaps) of 5, 10 and 20 μm respectively. The electrode arrays with various patterns were written within the outline of about 1.55 × 1.33 mm as shown in Fig. 3 (a).

The hysteresis loops of the films were measured using a modified Sawyer-Tower circuit with 50 Hz, triangle waveform driving signals. Direct electrical hysteresis between induced charge and applied voltage in the 5 μm-gap electrode system is given in Fig. 4 (a). If it is assumed that the area switched is the product of the length of electrode fingers and film thickness and that the field is uniform across the electrode gap, the data may be converted to a P (polarization) vs E (field) scale. Fig 4 (b) shows the loops superposed for 5, 10, and 20 μm finger gaps under such assumptions. Clearly there will be fringing fields associated with the finger terminations which will affect the calculated polarization and electric field values. However, it is encouraging to find the remanent polarization (P_r) of order 20 $\mu C/cm^2$ and the coercive field (E_c) of order 40 kV/cm, which are close to the

corresponding values of PZT films deposited on platinum-buffered silicon substrates using similar sol-gel processing.[8]

In summary, PZT (52/48) films with the thickness of about 1 μm have been prepared on ZrO_2 buffered silicon substrates. Both the ZrO_2 and PZT films were deposited using a similar sol-gel processing. The results indicate that the deposited ZrO_2 film can work effectively as a buffer layer. The strong symmetric hysteresis loops measured by using interdigitated electrodes on the surface of PZT film suggest very good transverse coherence in the film. Current work is concerned with studying the retention of polarization along transverse direction and the related piezoelectric effect, and developing PZT films with thickness up to 5 μm in order to construct micromachined unimorph transducer arrays with the working frequency at MHz range for hand-held underwater 3-D imaging system.

References

1. A. J. Moulson and J. M. Herbert, *Electroceramics* (Chapman & Hall. London, 1990), Chapter 6.

2. V. D. Kugel, S. Chandran, and L. E. Cross. Appl. Phys. Lett., **69**, 2021 (1996).

3. V. D. Kugel, S. Chandran, and L. E. Cross, Proc. SPIE, **3040**, 9 (1997).

4. D. L. Polla and L. F. Francis, MRS Bulletin, **21** (7), 59 (1996).

5. J. J. Bernstein, S. L. Finderg, K. Houston, L. C. Niles, H. D. Chen, L. E. Cross, K. K. Li, and K. R. Udayakumar, IEEE Trans. Ultrason., Ferroelect., Freq. Contr., **44**, 960 (1997).

6. S. Watanabe and T. Fulii, Rev. Sci. Instrum., **67**, 3898 (1996).

7. G. Yi, Z. Wu, and M. Sayer, J. Appl. Phys., **64**, 2717 (1988).

8. H. D. Chen, K. R. Udayakumar, C. J. Gaskey, L. E. Cross, J. J. Bernstein, L. C. Niles, J. Am. Ceram. Soc., **79**, 2189 (1996).

Figure Captions

Figure 1. X-ray diffraction patterns of the films.

Figure 2. SEM micrographs of the sample.

(a) Surface microstructure of the PZT film (b) Cross-sectional microstructure

Figure 3. Schematic map of the surface interdigitated electrode patterns.

(a) Top view (b) Cross-sectional morphology

Figure 4. Field-induced charge and polarization of the PZT film using the surface interdigitated electrodes.

(a) Direct voltage-charge relationship for the 5 μm gap electrode system

(b) Field-induced polarization for the electrode patterns with various finger gaps.

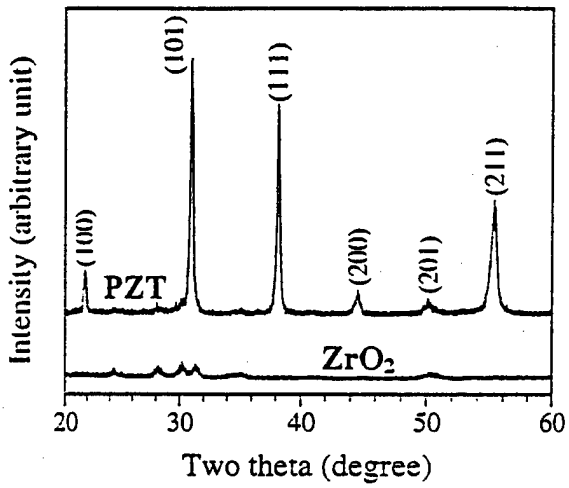

Fig. 1 of 4

B. Xu et al

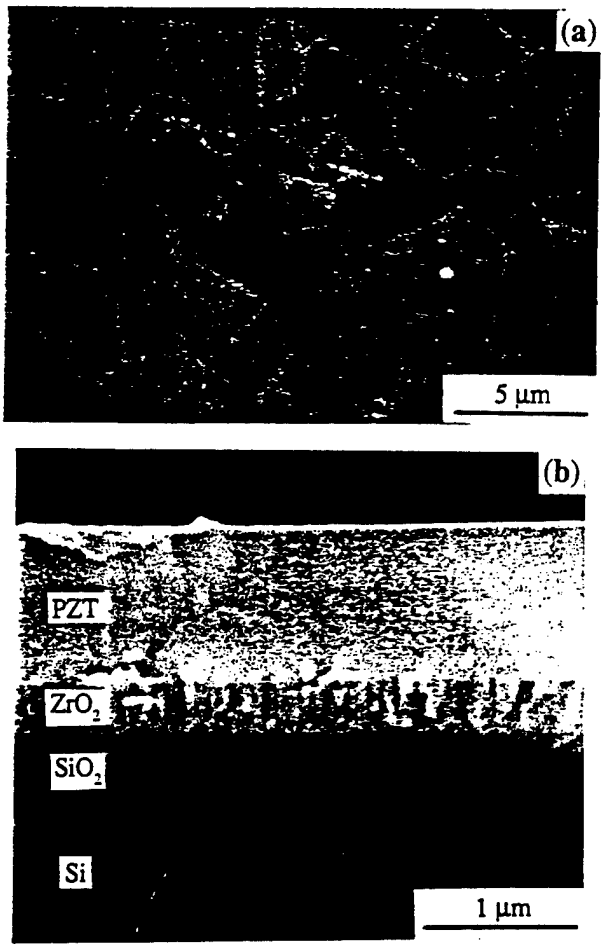

Fig. 2 of 4

B Xu et al

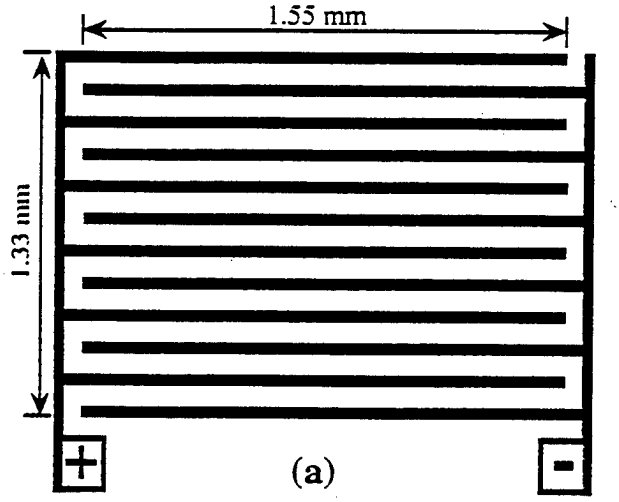

(a)

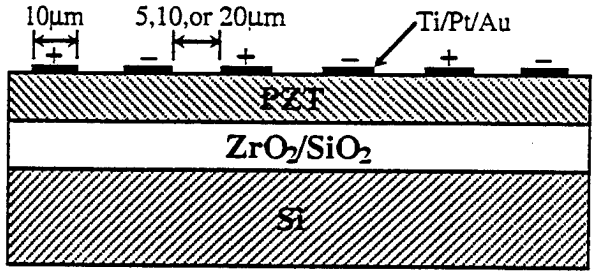

(b)

Fig. 3. of 4

B. Xu et al

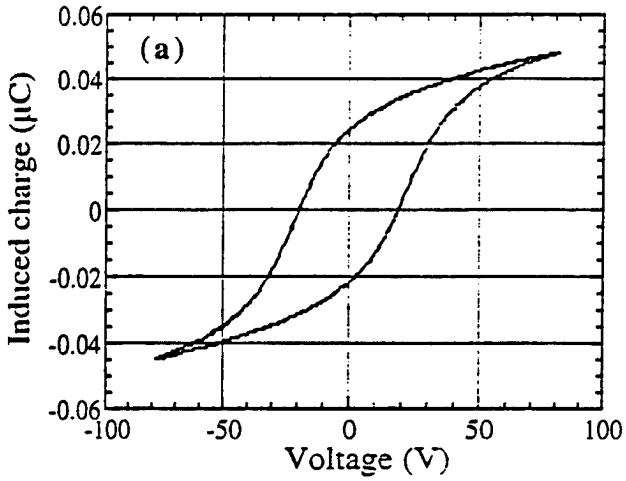

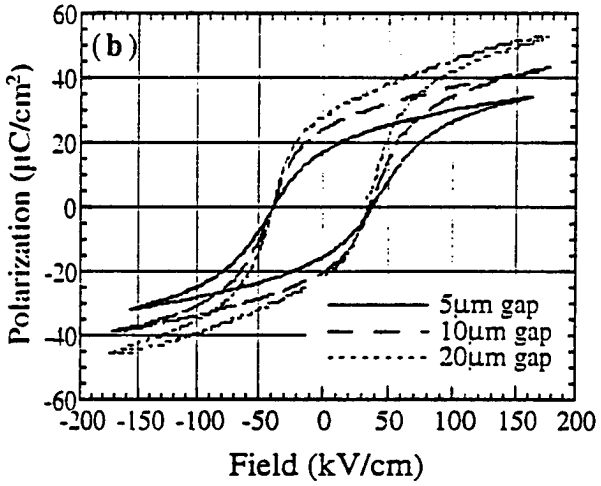

Fig. 4 of 4

B. Xu et al

APPENDIX 72

Integrated Ferroelectrics, 1998, Vol. 22, pp. 545–55
Reprints available directly from the publisher
Photocopying permitted by license only

ANTIFERROELECTRIC THIN AND THICK FILMS FOR HIGH-STRAIN MICROACTUATORS

BAOMIN XU*, NEELESH G. PAI, QING-MING WANG,
and L. ERIC CROSS
Intercollege Materials Research Laboratory, Pennsylvania State University,
University Park, PA 16802, USA

(Received 4 June 1998

Niobium-doped or lanthanum-doped lead zirconate titanate stannate antiferroelectric thin and thick films have been prepared on platinum-buffered silicon substrates by a modified sol-gel method and their electric properties were characterized, with emphasis on the field-induced phase transition strains. All the films demonstrate zero remanent polarization and a maximum polarization of more than 30 $\mu C/cm^2$. By choosing the appropriate compositions, the films can have either "square" hysteresis loops with very sharp phase transition or "slanted" hysteresis loops with gradual phase transition. The strain levels of the thin films can reach 0.32% with smaller hysteresis or 0.42% with moderate hysteresis. The thick films can either have a strain level of 0.38% with very small hysteresis or have a strain level of 0.48% with clear digital actuator response. Hence the strain levels of these antiferroelectric films are comparable to that of bulk materials and double that of PZT ferroelectric films, and they are very promising for actuation applications in microelectromechanical systems.

Keywords: antiferroelectrics; lead zirconate titanate stannate; thin films: thick films; microactuators; field-induced strain

* Corresponding author. Electronic mail: bxx2@psu.edu

INTRODUCTION

Antiferroelectric materials in the lead zirconate titanate stannate family have been studied for actuator applications during the past several decades because of the large strains concurrent with the antiferroelectric-to-ferroelectric phase transition[1-4]. It has been found that, depending on compositions and temperatures, the antiferroelectric-to-ferroelectric phase transition can occur as a step function of electric field or change gradually with electric field. These two types of transitions are characterized by "square" and "slanted" hysteresis loops, which allow for digital or analog actuator applications. For the materials with square hysteresis loops, strain levels of 0.4% can easily be reached and repeated[4] while strain levels as high as 0.85% have been reported[3]. Considering their strong actuation ability in the bulk form, thin (thickness < 1 μm) and thick (thickness > 1 μm) films in this system have been investigated since 1990s for the microactuation applications in microelectromechnical systems (MEMS)[5-7]. However, most of the reported antiferroelectric thin and thick films have some remanent polarization, which is believed to be due to the retention of the ferroelectric phase. The strain levels of the antiferroelectric thin films are less than 0.2%[5,6], which are much smaller than that in the bulk materials, and there are no strain data available about antiferroelectric thick films.

Recently, our group reported that both niobium-doped and lanthanum-doped lead zirconate titanate stannate antiferroelectric thin and thick films can be prepared from modified sol-gel spin-on techniques[8-10]. All these films demonstrate zero remanent polarization after the electric field is removed. By choosing appropriate compositions, the antiferroelectric films can either have

a typical square hysteresis loop or have a typical slanted hysteresis loop. In this work, the electrical properties of these antiferroelectric thin and thick films are characterized, with emphasis on the field-induced phase transition strains. The results show that the strain levels of these thin and thick films are comparable to that of bulk materials, and the highest value can reach 0.48% for the antiferroelectric thick films with square hysteresis loops. Therefore, these films are very promising for actuation applications as microactuators, micromotors, microvalves and other MEMS devices.

EXPERIMENTAL PROCEDURE

The compositions used in this work are $Pb_{0.99}Nb_{0.02}(Zr_{0.85}Sn_{0.13}Ti_{0.02})_{0.98}O_3$ (abbreviated as PNZST) and $Pb_{0.97}La_{0.02}(Zr_{0.65}Sn_{0.31}Ti_{0.04})O_3$ (abbreviated as PLZST), and the sample composition and preparation methods are listed in Table I. The thin film samples with the thickness of around 0.4 μm are prepared either from 2-methoxyethanol-based sol-gel method (for PNZST) or from acetic acid-based sol-gel method (for PLZST). By using a multi-step annealing process and suitable PbO coating layers, the thick film samples with the thickness of about 5 μm are prepared from acetic acid-based sol-gel method (for both PNZST and PLZST). The flow chart to make the thin films by 2-methoxyethanol-based method is given in Fig. 1, and the processing details are described in Ref. [8]. Lead acetylacetonate, titanium isopropoxide, zirconium n-propoxide, tin acetate, and niobium ethoxide were added to 2-methoxyethanol and the mixture was refluxed at 115°C for 12 h. The solution

TABLE I Sample compositions and preparation methods

Sample Notation	Compositions*	Preparation method	Remarks
N-1	PNZST	2-methoxyethanol-based	thin film
L-1	PLZST	acetic acid-based	thin film
N-2	PNZST	acetic acid-based	thick film
L-2	PLZST	acetic acid-based	thick film

* The PNZST is $Pb_{0.99}Nb_{0.02}(Zr_{0.85}Sn_{0.13}Ti_{0.02})_{0.98}O_3$ and the PLZST is $Pb_{0.97}La_{0.02}(Zr_{0.65}Sn_{0.31}Ti_{0.04})O_3$.

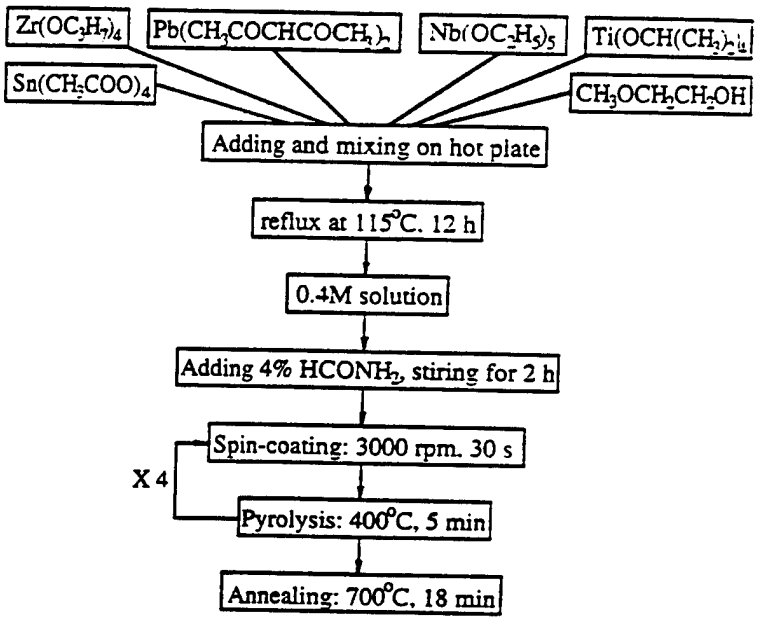

FIGURE 1 Flow chart to make thin films by 2-methoxyethanol-based method

was then cooled to room temperature and 4% formamide was added to promote proper drying and to adjust the concentration to be 0.4 M. The flow chart to make the PNZST thick films are shown in Fig. 2 and the processing details are described in Ref. [10]. Lead acetate trihydrate and tin acetate were initially dissolved in acetic acid and the mixture is distilled at 150°C to remove the associated water, then the solution was added with zirconium n-propoxide, titanium isopropoxide and niobium ethoxide and mixed at 105°C for 1 h. Ethylene glycol and deionized water were added during reflux to control the viscosity and to adjust the concentration to be 0.75 M. 0.70 M

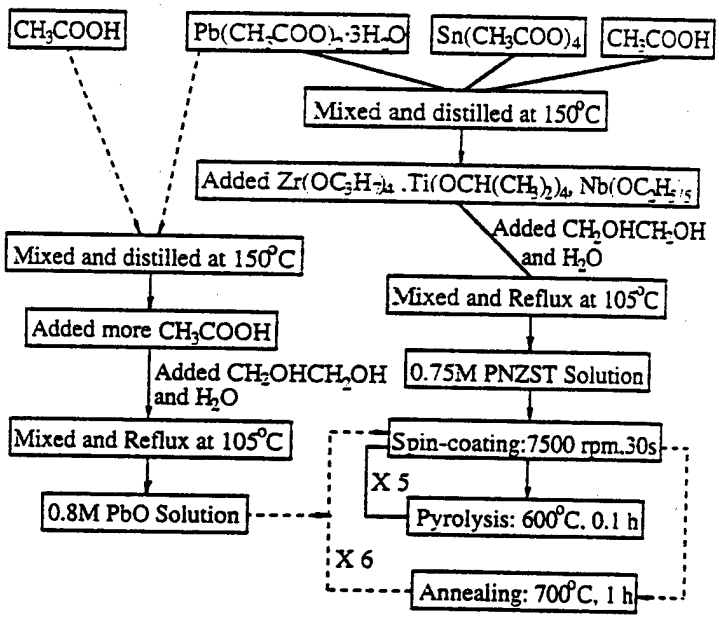

FIGURE 2 Flow chart to make thick films by acetic acid-based method

PLZST solution was prepared by using lanthanum ethoxide instead of niobium ethoxide and 0.80 M PbO cover solution was prepared using similar procedure. To make PLZST thin films, the PLZST solution was diluted to 0.40 M by adding more acetic acid.

All the films are deposited on platinum-buffered, n-type, (100) oriented silicon wafers. The thin films were prepared through a simple multi-step spin-on procedure. To make PNZST thin films from 2-methoxyethanol-based method, the films were pyrolyzed at 400°C for 5 min on a hot plate after the deposition of each layer and annealed at 700°C for 18 min after the 4th layer deposition. To prepare PLZST thin films from acetic acid-based method, the pyrolysis condition is 600°C for 0.1 h in a commercial box furnace and the annealing condition is 700°C for 1 h.

The procedure to deposit thick films is more complicated, which we named as multi-step annealing with multiple PbO coating layers. The films were first pyrolyzed at 600°C for 0.1 h after the deposition of each layer, then they were covered with PbO coating solution and annealed at 700°C after the deposition of 5 layers of PNZST solution or 6 layers of PLZST solution. This cycle is repeated until 30 layers of PNZST solution or 42 layers of PLZST solution are coated. The effects of multi-step annealing and PbO coatings are discussed in Ref [10] and beyond the scope of this paper.

The thickness of the films were determined from surface profilometer traces. Platinum top electrodes with a diameter of 1.6 mm were deposited by rf sputtering method for electrical property characterization. The low field dielectric properties were measured using an HP4274A LCR meter with an oscillating field of about 2 mV/μm and a frequency of 1 kHz. The hysteresis

loops were measured using a modified Sawyer-Tower circuit with a 50 Hz, triangular waveform driving field. The phase transition strains were determined by using the sensitive double beam laser interferometer. The description of the measurement system can be found in Refs. [11] and [12], but an oscilloscope is used as the final data output instead of lock-in amplifier because of the nonlinear relationship between the driving field and phase transition strain. A driving voltage with 100 Hz, triangular waveform was used.

RESULTS AND DISCUSSION

Dielectric and Ferroelectric Properties

The hysteresis loops of the thin and thick film samples are illustrated in Fig. 3 and Fig. 4 respectively, and their electric property data are summarized in Table II. It can be seen that all the samples have relatively low dielectric loss (lower than 2.0% for Samples N-1, N-2, and L-2 and lower than 3.0% for Sample L-1) and show zero remanent polarization after the electric field is removed. The maximum polarization of Samples N-1 and N-2 can reach 40 $\mu C/cm^2$. This value is much higher than the former reported 20 $\mu C/cm^2$ for the thin films[6] and 28 $\mu C/cm^2$ for the 2.4 μm-thick films[7] in the niobium-doped lead zirconate titanate stannate antiferroelectric system (The electric property data for the films thicker than 2.4 μm have not been found). All these PNZST samples possess rather square hysteresis loops, although the phase transition of Sample N-1 is not so sharp and its phase transition fields are determined by extrapolating the steepest sections of the hysteresis loop and obtaining their

intersections with the horizontal axis. Very sharp phase transition has been observed in the hysteresis loop of the 5 μm-thick PNZST sample (Sample N-1), which is almost perpendicular to the electric field axis. The PLZST samples show typical slanted hysteresis loops and have a maximum polarization of higher than 30 $\mu C/cm^2$. Although it has been reported that the maximum polarization can reach 30 $\mu C/cm^2$ in the lanthanum-doped lead

TABLE II Electrical properties of the films

Sample Notation	Thickness (μm)	ε_r	tanδ (%)	$E_{AF\rightarrow F}$ (kV/cm)	$E_{F\rightarrow AF}$ (kV/cm)	P_{max} ($\mu C/cm^2$)
N-1	0.43	280	1.97	160	75	41
L-1	0.36	360	2.75	----*	---*	30
N-2	4.98	283	1.7	150	97	40
L-2	5.04	434	2.0	----*	---*	35

*can not be given because of the slanted shape of the hysteresis loops.

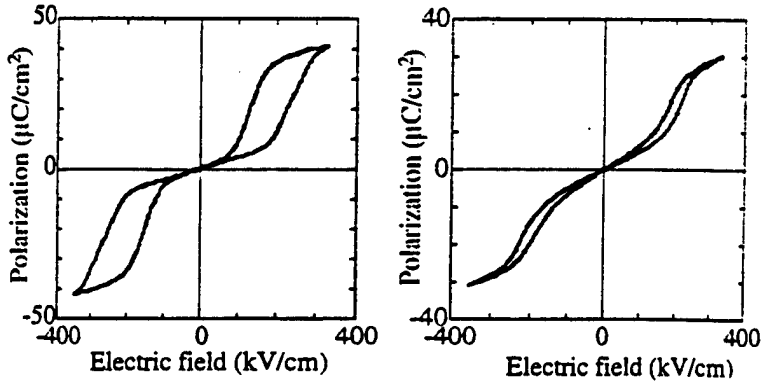

(a) Sample N-1 (b) Sample L-1

FIGURE 3 Hysteresis loops of the thin film samples

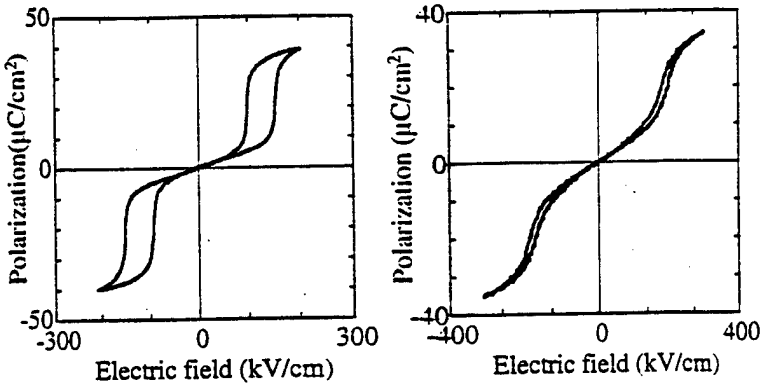

(a) Sample N-2 (b) Sample L-2

FIGURE 4 Hysteresis loops of the thick film samples

zirconate titanate stannate system, their samples have rather large remanent polarization[5] and there is no report on the thick films in the lanthanum-doped system.

Field-induced Phase Transition Strain

The phase transition strains of the thin and thick film samples are shown in Fig. 5 and Fig. 6 respectively. This is the first time that the strain data for antiferroelectric thick films have been reported. The maximum strain levels can reach 0.32% for Sample L-1, 0.42% for Sample N-1, 0.38% for Sample L-2, and 0.48% for Sample N-2. They are comparable to most bulk materials which have strain levels of around 0.4%. The thick films have higher strain levels than thin films even though the driving fields applied to them are lower than that for thin films. This may be due to the fact that thick films have less clamping effect at the film-substrate interface than thin films.

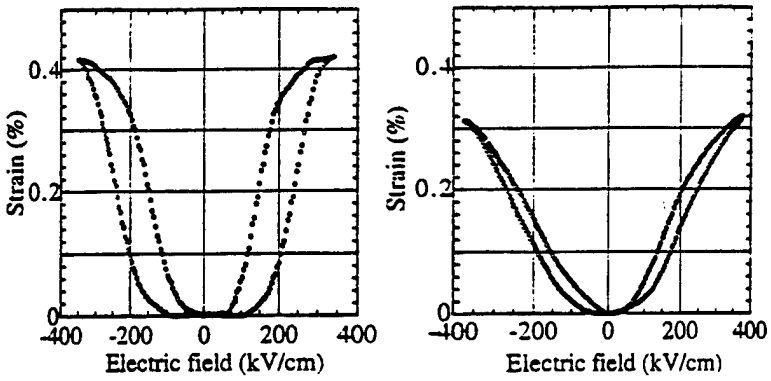

(a) Sample N-1 (b) Sample L-1

FIGURE 5 Field-induced strains of the thin film samples

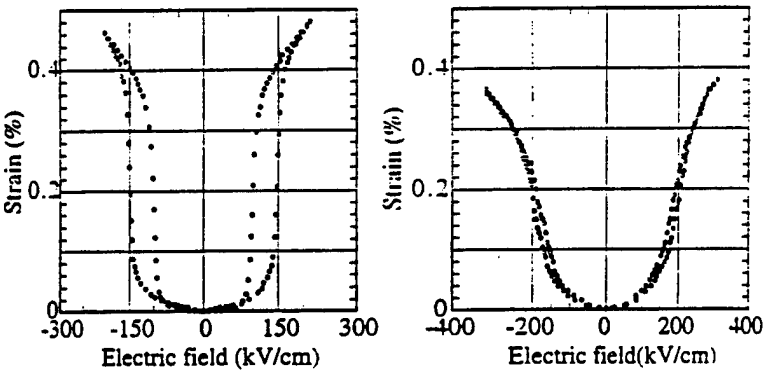

(a) Sample N-2 (b) Sample L-2

FIGURE 6 Field-induced strains of the thick film samples

As comparing to the strain level of about 0.16% reported before for antiferroelectric thin films[5,6], the strain levels for the thin films here are much higher, which can be attributed to several factors. First, the present samples have much larger maximum polarization, which greatly enhances their polarization strain. Secondly, the zero remanent polarization, implying no

retention of the ferroelectric phase in these samples, indicates that there is much less internal stress in the films, and this internal stress is a factor believed to retard the antiferroelectric-to-ferroelectric phase transition and reduce the phase transition strain. Thirdly, electric fields of more than 300 kV/cm are used here, which is larger than the electric fields used in the earlier reports (225 kV/cm in Ref. [5] and 160 kV/cm in Ref. [6]).

There is a strong correlation between the shape of the hysteresis loop and the nature of the strain curve. Corresponding to their slanted hysteresis loops, the strain curve for Sample L-1 has relatively smaller hysteresis and gradually increase with electric field, and the strain curve of Sample L-2 has very small hysteresis. These PLZST films are suitable for analog mechanical response applications. The strain curve of Sample N-1 shows a moderate hysteresis and the strain begins to be generated only when the electric field becomes larger than 100 kV/cm, showing a digital response character to some extent. In the strain curve of Sample N-2, there is a jump of about 0.3% around the antiferroelectric-to-ferroelectric phase transition field, demonstrating a very clear digital actuator response. Therefore, the microactuators made from these antiferroelectric thin and thick films can meet the requirements for various electro-mechanical responses.

CONCLUSIONS

Antiferroelectric thin and thick films in lead zirconate titanate stannate family have been prepared on platinum-buffered silicon substrates by modified sol-gel spin-on techniques and their electric properties were characterized. These

films can be niobium-doped or lanthanum-doped. The 0.4 μm-thick antiferroelectric thin films were prepared from 2-methoxyethanol-based method for Nb-doped samples and acetic acid-based method for La-doped samples. By using a multi-step annealing process with multiple PbO coating layers, the 5 μm-thick antiferroelectric thick films were prepared from the acetic acid-based method. All the films demonstrated zero remanent polarization and the maximum polarization values are larger than 30 $\mu C/cm^2$. By choosing the appropriate compositions, the films can be made to have either square hysteresis loops with sharp phase transition, which are suitable for digital mechanical response applications, or slanted hysteresis loops with gradual phase transition, which are suitable for analog mechanical response applications. The thin films can have field-induced phase transition strain of 0.32% with smaller hysteresis or 0.42% with moderate hysteresis. For the thick films, the field-induced phase transition strain can reach 0.38% for films with very small hysteresis or 0.48% for films with very clear digital actuator response. Therefore, these antiferroelectric thin and thick films are very promising for high-strain actuation applications in MEMS devices.

Acknowledgment

This work is supported by the Office of Naval Research and the Charles Stark Draper Laboratory.

References

[1.] D. Berlincourt, *IEEE Trans. Sonics Ultrason.*, **13**, 116 (1966).
[2.] K. Uchino and S. Nomura, Ferroelectrics, **50**, 517 (1983).
[3.] W. Y. Pan, C. Q. Dam, Q. M. Zhang, and L. E. Cross, *J. Appl. Phys.*, **66**, 6014 (1989).

[4.] K. Markowski, S. E. Park, S. Yoshikawa, and L. E. Cross, *J. Am. Ceram. Soc.*, **79**, 3297 (1996).
[5.] K. G. Brooks, J. Chen, K. R. Udayakumar, and L. E. Cross, *J. Appl. Phys.*, **75**, 1699 (1994).
[6.] S. S. Sengupta, D. Roberts, J. F. Li, M. C. Kim, and D. A. Payne, *J. Appl. Phys.*, **78** 1171 (1995).
[7.] Y. Akiyama, S. Kimura, and I. Fujimura, *Jpn. J. Appl. Phys.*, **32**, 4154 (1993).
[8.] C. J. Gaskey, K. R. Udayakumar, H. D. Chen, and L. E. Cross, *J. Mater. Res.*, **10**, 2764 (1995).
[9.] Baomin Xu, N. G. Pai, and L. E. Cross, to be published in *Mater. Lett.*, **34**, (1988).
[10.] Baomin Xu, L. E. Cross, and D. Ravichandran, submitted to *J. Am. Ceram. Soc.*
[11.] Q. M. Zhang, W. Y. Pan, and L. E. Cross, *J. Appl. Phys.*, **63**, 2492 (1988).
[12.] W. Y. Pan and L. E. Cross, *Rev. Sci. Instrum.*, **60**, 2701 (1989).

MODELING
and
CHARACTERIZATION

Domain Studies

APPENDIX 73

Effective material properties in twinned ferroelectric crystals

Jiří Erhart* and Wenwu Cao

Materials Research Laboratory

Pennsylvania State University, University Park, PA 16802, U.S.A.

(January 15, 1999)

Abstract

Without external fields, ferroelectric materials will have multi-domain configuration in the ferroelectric state. Detailed analysis found that twinning may not be treated as random since the number of orientations for the domain walls are limited in a given symmetry change during a ferroelectric phase transition. In each finite region of a large crystal or in small crystallites, a particular set of twins is favored under certain boundary conditions, which consists of only two of the low temperature variants. Statistic models of random distribution of domains do not apply for calculating the physical properties of such twin structures. However, one could derive the two domain twin properties by using the constitutive equations and appropriate mechanical boundary considerations. This paper presents a theoretical analysis on such a two-domain twin system, including its global symmetry and effective material properties resulting from different twinning configurations. Numerical results are derived for $LiNbO_3$ and $BaTiO_3$.

77.84.Fm, 62.20.-x, 62.20.Dc, 74.72.Lw

Typeset using REVTEX

---

*on leave from the Department of Physics, Technical University of Liberec, Liberec, Czech Republic

I. INTRODUCTION

The macroscopic material properties of a multi-domain ferroelectric system are collective average of individual domains. Traditionally, people took statistic average of the properties of all the low temperature variants and used the volume ratio as the weighting factor. However, in reality, different physical properties may follow different averaging rules depending on the geometric configuration. For many properties the contribution of each domain do not always coincides with their volume ratio. For example, the elastic constant of a fiber reinforced composite is much larger in the fiber length direction than in its radial direction, although the volume ratio can be the same. Similarly, in a multi-domain system the contribution of each domain not only depends on the volume ratio but also on the relative geometric configuration and to the orientation of the applied external fields. Experimental evidence showed that the domains often appear in a twin band with only two variants in the set[1,2]. Even for a ceramic system, domains observed in each given grain are mostly twin pair sets rather than all the available variants. Such limited variant twinning pattern is more pronounced in a single crystal system since all orientations must be coherently joined together. Each twin band often occupies a sizable volume in a large single crystal. Generally speaking, two-variant twinning is the basis of all multi-domain systems in ferroelectrics.

Recent development in domain engineering of relaxor based single crystal systems (e.g. for single crystals PZN-PT, PMN-PT) produced much enhanced piezoelectric and dielectric properties[3]. Experimental observation showed that many engineered crystal systems have only two variants[4]. Even those nonpoled samples are composed of large regions of two variants twin band structures. Experimental observation of these relaxor based single crystals revealed that the twinning mostly consists of two variant twins[5,6] (for PZN and for $BaTiO_3$). It is also found that the orientation of the two domain system and the selection of the variants can significantly influence the effective material properties of multi-domain systems. This means that the statistical model or models depend only on the volume ratio will not give proper prediction of the physical properties in these domain engineered crys-

tals. Roughly speaking, the volume ratio average scheme assumed isotropic distribution of domain walls and ignored the cross coupling between different quantities of the associated domains.

If we utilize the fact that the basic domain structure only consists of two variants and they have certain orientation relation in domain engineered crystal systems, it is possible to accurately derive the apparent macroscopic property by directly apply external loads to the system. Such a two-variant domain set can then serve as the building block to calculate properties of systems with more complex domain patterns.

The importance of calculating the effective properties of two domains lies in the fact that the macroscopic properties observed experimentally, no matter from ultrasonic method or from resonance technique, are actually a collective contribution of the *existing* domains, not all *possible* domains. In a given domain engineered single crystal, only some of the low temperature variants can appear.

Because of the importance of predicting the effective material properties, there are vast literatures on property averaging of multi-component systems. For example, the equivalent elastic constants were previously calculated for two layer elastic system[7] by using the volume ratio as the weighing factor for both the stress and strain. Their approach allows the calculation of elastic properties in two layer system for materials of any symmetry and any orientation between the two layers. This method was later extended to piezoelectric materials [8]. Dynamic approach for calculating the effective material properties of piezoelectric layered material of arbitrary orientation[9] was based on the nature of acoustic wave propagation in layered material in the long-wavelength limit. It allowed explicit calculation of complete set of all material properties. Another method for effective material property calculations is the method of effective medium which was applied to calculate the properties of polycrystalline ceramics[10-12] and piezoelectric composites[13,14]. The mechanical stress and electric field were assumed uniform in the matrix and in the inclusion (grains). The average was calculated under a number of assumptions about the space distribution and the shape of inclusions (spherical and elliptical shape). Effective material properties for 1-3 composites

were calculated for $6mm$ symmetry as a function of volume fraction[13]. While all of these techniques have advantages and disadvantages in certain aspects, they have provided guidance to many particular applications and to the proper characterization of multi-component systems of interest to certain accuracy.

However, it is not appropriate to use the volume ratio average if there are only limited number of domains in a system. In this paper we will try to eliminate some of those less convincing assumptions used in previous averaging methods and develop a systematic procedure particularly applicable to a two domain twin system. We will use different weighing factors for different physical properties based on the relative orientation to the external stress and electric field. Some quantities in each domain can be the same as in the combined twin system rather than all quantities being the weighted average. We will also give the macroscopic symmetry associated with twinning of different pairs of the low temperature variants resulting from cubic to rhombohedral and cubic to tetragonal ferroelectric phase transitions. Numerical applications of this averaging technique were performed on $LiNbO_3$ ($m3m \rightarrow 3m$) and $BaTiO_3$ ($m3m \rightarrow 4mm$) and the results were compared to that obtained by the method given in Ref. [8].

II. AVERAGING OF TENSOR PROPERTIES IN A TWIN CRYSTAL

For the twinned structure under study, we assume that the two variants have a volume ratio of $v^{(1)}$ and $v^{(2)}$ and the domain wall(DW) is perpendicular to the y-axis. Considering the unit cell of a twin structure as shown in Fig. 1, we can apply static stress and electric field to the system and use the response to derive the effective average property of this twin crystal. For generality, we allow the crystallographic symmetry of both materials to be arbitrary, however the material properties of both domains must be expressed in the same coordinate system before performing the average. For a ferroelectric system, the material properties are represented by the elastic compliance tensor $\mathbf{s}^{(i)}$, piezoelectric constant tensor $\mathbf{d}^{(i)}$ and dielectric constant tensor $\boldsymbol{\epsilon}^{(i)}$, which satisfy the constitutive relations.

$$\begin{pmatrix} \eta^{(i)} \\ \mathbf{D}^{(i)} \end{pmatrix} = \begin{pmatrix} \mathbf{S}^{(i)} & \mathbf{d}^{(i)\mathbf{T}} \\ \mathbf{d}^{(i)} & \epsilon^{(i)} \end{pmatrix} \begin{pmatrix} \mathbf{T}^{(i)} \\ \mathbf{E}^{(i)} \end{pmatrix}, i = 1, 2 \tag{1}$$

where the superscripts (1) and (2) represent the quantity for domain 1 and domain 2 respectively. $\eta^{(i)}$ and $\mathbf{D}^{(i)}$ are the elastic stain tensor and the electric displacement vector. $\mathbf{d}^{(i)}$ and $\mathbf{E}^{(i)}$ are the stress and electric field. respectively. The two domains can be of different thickness, which is represented by volume ratios $v^{(1)}$ and $v^{(2)}$ with $v^{(1)} + v^{(2)} = 1$. Components of elastic strain η are assumed to be symmetric. while the components of elastic stress do not have this symmetry due to the cross domain coupling and the simplified notation is related to the true tensor notation in the following form.

$$T_\lambda = \begin{Bmatrix} T_{ij} & i = j \\ T_{ij} + T_{ji} & i \neq j \end{Bmatrix}, \quad i, j = 1.2.3 \tag{2}$$

Since the material properties are similar in magnitude for the two domains. unlike the case of polymer-ceramic composite[15,16]. it is reasonable to assume that the mechanical stress. strain. electric field and electric displacement in both domains are homogeneous in the equilibrium state. At equilibrium. the effective stress and strain of the twin system is symmetric and the two domains are required to form a coherent non-separating boundary (DW) under external applied stresses. For convenience. we will use the shortened notation for all the tensor components of material properties defined by [17]

$$s_{\lambda\nu} = \begin{Bmatrix} s_{ijkl} & i = j, k = l \\ 2s_{ijkl} & i \neq j, k = l \\ 2s_{ijkl} & i = j, k \neq l \\ 4s_{ijkl} & i \neq j, k \neq l \end{Bmatrix}, \quad i, j, k, l = 1.2.3 \tag{3a}$$

$$d_{i\mu} = \begin{Bmatrix} d_{ijk} & j = k \\ 2d_{ijk} & j \neq k \end{Bmatrix}, \quad j, k = 1, 2. 3. \tag{3b}$$

The constitutive relations for each of the domains are

$$\eta_{ij}^{(n)} = d_{ijk}^{(n)} E_k^{(n)} + s_{ijkl}^{(n)} T_{kl}^{(n)}, \tag{4a}$$

$$D_i^{(n)} = \epsilon_{ij}^{(n)} E_j^{(n)} + d_{ijk}^{(n)} T_{jk}^{(n)}, \quad i,j,k.l = 1,2,3, \quad n = 1,2, \tag{4b}$$

where $T_{ij}^{(n)}$ and $E_k^{(n)}$ are the components of elastic stress tensor and electric field vector.

Volume ratio averaging conditions can be expressed as[8]

$$\eta_{ij}^{eff} = v^{(1)}\eta_{ij}^{(1)} + v^{(2)}\eta_{ij}^{(2)} \tag{5a}$$

$$T_{ij}^{eff} = v^{(1)}T_{ij}^{(1)} + v^{(2)}T_{ij}^{(2)}, i,j = 1,2,3. \tag{5b}$$

These relations can not hold true simultaneously for both the strain and stress as one can see from the twin structure in Fig. 1. We need to redefine the conditions for such a system for which the orientation and configuration are known. Mechanical equilibrium and non-separable boundary conditions. i.e.. the continuity of 3 normal components of stress $T_{22}^{(i)}, T_{23}^{(i)}, T_{21}^{(i)}$. 6 tangential components of strain $\eta_{11}^{(i)}, \eta_{33}^{(i)}, \eta_{32}^{(i)}, \eta_{13}^{(i)}, \eta_{31}^{(i)}, \eta_{12}^{(i)}$. 2 tangential components of electric field $E_1^{(i)}, E_3^{(i)}$ and normal component of electric displacement $D_2^{(i)}$, $(i = 1.2)$, lead directly to the following conditions:

$$\eta_{11}^{(1)} = \eta_{11}^{(2)} \tag{6a}$$

$$\eta_{33}^{(1)} = \eta_{33}^{(2)} \tag{6b}$$

$$\eta_{32}^{(1)} = \eta_{32}^{(2)} \tag{6c}$$

$$\eta_{13}^{(1)} = \eta_{13}^{(2)} \tag{6d}$$

$$\eta_{31}^{(1)} = \eta_{31}^{(2)} \tag{6e}$$

$$\eta_{12}^{(1)} = \eta_{12}^{(2)} \tag{6f}$$

$$D_2^{(1)} = D_2^{(2)} \tag{6g}$$

$$T_{22}^{(1)} = T_{22}^{(2)} \tag{6h}$$

$$T_{23}^{(1)} = T_{23}^{(2)} \tag{6i}$$

$$T_{21}^{(1)} = T_{21}^{(2)} \tag{6j}$$

$$E_1^{(1)} = E_1^{(2)} \tag{6k}$$

$$E_3^{(1)} = E_3^{(2)} \tag{6l}$$

These conditions provided new different averaging rules for some components of elastic stress, strain. electric field and electric displacement.

Equations (6a) - (6l) give the relations between the elastic stress and electric field in domain 2 and domain 1. For a prescribed stress or electric field to the twinned system, one can first represent the stress and field in domains 1 and 2 using the global quantities. Then, these tensor components can be substituted into the equations (5a) - (5b) and the effective material properties will be found. The system of linear equations (6a) - (6l) can be solved in matrix form

$$\mathbf{b}^{(1)}\tau^{(1)} = \mathbf{b}^{(2)}\tau^{(2)}, \tag{7}$$

where

$$\mathbf{b}^{(i)} = \begin{pmatrix} s_{11}^{(i)} & s_{12}^{(i)} & s_{13}^{(i)} & s_{14}^{(i)} & s_{14}^{(i)} & s_{15}^{(i)} & s_{16}^{(i)} & s_{16}^{(i)} & d_{11}^{(i)} & d_{21}^{(i)} & d_{31}^{(i)} \\ 0 & 1 & 0 & 0 & 0 & 0 & 0 & 0 & 0 & 0 & 0 \\ s_{13}^{(i)} & s_{23}^{(i)} & s_{33}^{(i)} & s_{34}^{(i)} & s_{34}^{(i)} & s_{35}^{(i)} & s_{36}^{(i)} & s_{36}^{(i)} & d_{13}^{(i)} & d_{23}^{(i)} & d_{33}^{(i)} \\ 0 & 0 & 0 & 1 & 0 & 0 & 0 & 0 & 0 & 0 & 0 \\ s_{14}^{(i)} & s_{24}^{(i)} & s_{34}^{(i)} & s_{44}^{(i)} & s_{44}^{(i)} & s_{45}^{(i)} & s_{46}^{(i)} & s_{46}^{(i)} & d_{14}^{(i)} & d_{24}^{(i)} & d_{34}^{(i)} \\ s_{15}^{(i)} & s_{25}^{(i)} & s_{35}^{(i)} & s_{45}^{(i)} & s_{45}^{(i)} & s_{55}^{(i)} & s_{56}^{(i)} & s_{56}^{(i)} & d_{15}^{(i)} & d_{25}^{(i)} & d_{35}^{(i)} \\ s_{16}^{(i)} & s_{26}^{(i)} & s_{36}^{(i)} & s_{46}^{(i)} & s_{46}^{(i)} & s_{56}^{(i)} & s_{66}^{(i)} & s_{66}^{(i)} & d_{16}^{(i)} & d_{26}^{(i)} & d_{36}^{(i)} \\ 0 & 0 & 0 & 0 & 0 & 0 & 0 & 1 & 0 & 0 & 0 \\ 0 & 0 & 0 & 0 & 0 & 0 & 0 & 0 & 1 & 0 & 0 \\ d_{21}^{(i)} & d_{22}^{(i)} & d_{23}^{(i)} & d_{24}^{(i)} & d_{24}^{(i)} & d_{25}^{(i)} & d_{26}^{(i)} & d_{26}^{(i)} & \epsilon_{12}^{(i)} & \epsilon_{22}^{(i)} & \epsilon_{23}^{(i)} \\ 0 & 0 & 0 & 0 & 0 & 0 & 0 & 0 & 0 & 0 & 1 \end{pmatrix}, \quad i = 1, 2. \tag{8}$$

and transposed vector $\tau^{(i)}$ is

$$\tau^{(i)T} = \left(T_{11}^{(i)}, T_{22}^{(i)}, T_{33}^{(i)}, T_{23}^{(i)}, T_{32}^{(i)}, T_{13}^{(i)} + T_{31}^{(i)}, T_{12}^{(i)}, T_{21}^{(i)}, E_1^{(i)}, E_2^{(i)}, E_3^{(i)}\right). \tag{9}$$

To find out the effective material properties of two-domain system. we can use matrix calculations. In the examples. however. we will solve them in steps in for convenience.

Nine simple loads for the two-domain system were applied to help us derive the independent effective constants. In each case. only one or two components of the load is non-zero.

- longitudinal stress

  1. $T_{11}^{eff} \neq 0$
  2. $T_{22}^{eff} \neq 0$
  3. $T_{33}^{eff} \neq 0$

  } All others are zero. i.e., $T_{ij}^{eff} = 0, E_i^{eff} = 0$

- shear stress

  4. $T_{23}^{eff} \neq 0, T_{32}^{eff} \neq 0$
  5. $T_{13}^{eff} \neq 0, T_{31}^{eff} \neq 0$
  6. $T_{12}^{eff} \neq 0, T_{21}^{eff} \neq 0$

  } All others are zero. i.e., $T_{ij}^{eff} = 0, E_i^{eff} = 0$

- electric field

  7. $E_1^{eff} \neq 0$
  8. $E_2^{eff} \neq 0$
  9. $E_3^{eff} \neq 0$

  } All others are zero. i.e., $T_{ij}^{eff} = 0, E_i^{eff} = 0$

The constitutive relations become relatively simple for these 9 independent loads for calculating the effective material properties. Usually only one kind of material constant for the effective material is involved in each equation.

Putting each of these 9 independent loads into the equations (6a)-(6l) and use the averaging rules (5a) - (5b) we obtain a system of linear equations

$$\mathbf{A}\vec{x}_i = \vec{y}_i, \tag{10a}$$

$$\mathbf{A} = \mathbf{A}^{(1)} + \frac{v^{(1)}}{v^{(2)}}\mathbf{A}^{(2)} \tag{10b}$$

$$\mathbf{A}^{(i)} = \begin{pmatrix} s_{11}^{(i)} & s_{13}^{(i)} & s_{14}^{(i)} & s_{15}^{(i)} & s_{16}^{(i)} & d_{21}^{(i)} \\ s_{13}^{(i)} & s_{33}^{(i)} & s_{34}^{(i)} & s_{35}^{(i)} & s_{36}^{(i)} & d_{23}^{(i)} \\ s_{14}^{(i)} & s_{34}^{(i)} & s_{44}^{(i)} & s_{45}^{(i)} & s_{46}^{(i)} & d_{24}^{(i)} \\ s_{15}^{(i)} & s_{35}^{(i)} & s_{45}^{(i)} & s_{55}^{(i)} & s_{56}^{(i)} & d_{25}^{(i)} \\ s_{16}^{(i)} & s_{36}^{(i)} & s_{46}^{(i)} & s_{56}^{(i)} & s_{66}^{(i)} & d_{26}^{(i)} \\ d_{21}^{(i)} & d_{23}^{(i)} & d_{24}^{(i)} & d_{25}^{(i)} & d_{26}^{(i)} & \epsilon_{22}^{(i)} \end{pmatrix}, i = 1, 2 \tag{10c}$$

$$\vec{t}_i = \begin{pmatrix} T_{11}^{(1)} \\ T_{33}^{(1)} \\ \frac{1}{2}T_{32}^{(1)} \\ \frac{1}{2}(T_{13}^{(1)} + T_{31}^{(1)}) \\ \frac{1}{2}T_{12}^{(1)} \\ E_2^{(1)} \end{pmatrix}, \quad i = 1, 2, \ldots, 9, \tag{10d}$$

$$\vec{y}_1 = \frac{1}{v^{(2)}} T_{11}^{eff} \begin{pmatrix} s_{11}^{(2)} \\ s_{13}^{(2)} \\ s_{14}^{(2)} \\ s_{15}^{(2)} \\ s_{16}^{(2)} \\ d_{21}^{(2)} \end{pmatrix}, \quad \vec{y}_2 = T_{22}^{eff} \begin{pmatrix} s_{12}^{(2)} - s_{12}^{(1)} \\ s_{23}^{(2)} - s_{23}^{(1)} \\ s_{24}^{(2)} - s_{24}^{(1)} \\ s_{25}^{(2)} - s_{25}^{(1)} \\ s_{26}^{(2)} - s_{26}^{(1)} \\ d_{22}^{(2)} - d_{22}^{(1)} \end{pmatrix}, \tag{10e}$$

$$\vec{y}_3 = \frac{1}{v^{(2)}} T_{33}^{eff} \begin{pmatrix} s_{13}^{(2)} \\ s_{33}^{(2)} \\ s_{34}^{(2)} \\ s_{35}^{(2)} \\ s_{36}^{(2)} \\ d_{23}^{(2)} \end{pmatrix}, \quad \vec{y}_4 = \frac{1}{2} T_{23}^{eff} \begin{pmatrix} (1 + \frac{1}{v^{(2)}}) s_{14}^{(2)} - s_{14}^{(1)} \\ (1 + \frac{1}{v^{(2)}}) s_{34}^{(2)} - s_{34}^{(1)} \\ (1 + \frac{1}{v^{(2)}}) s_{44}^{(2)} - s_{44}^{(1)} \\ (1 + \frac{1}{v^{(2)}}) s_{45}^{(2)} - s_{45}^{(1)} \\ (1 + \frac{1}{v^{(2)}}) s_{46}^{(2)} - s_{46}^{(1)} \\ (1 + \frac{1}{v^{(2)}}) d_{24}^{(2)} - d_{24}^{(1)} \end{pmatrix}. \tag{10f}$$

$$\vec{y}_5 = \frac{1}{v^{(2)}} T_{13}^{eff} \begin{pmatrix} s_{15}^{(2)} \\ s_{35}^{(2)} \\ s_{45}^{(2)} \\ s_{55}^{(2)} \\ s_{56}^{(2)} \\ d_{25}^{(2)} \end{pmatrix}. \quad \vec{y}_6 = \frac{1}{2} T_{12}^{eff} \begin{pmatrix} (1 + \frac{1}{v^{(2)}}) s_{16}^{(2)} - s_{16}^{(1)} \\ (1 + \frac{1}{v^{(2)}}) s_{36}^{(2)} - s_{36}^{(1)} \\ (1 + \frac{1}{v^{(2)}}) s_{46}^{(2)} - s_{46}^{(1)} \\ (1 + \frac{1}{v^{(2)}}) s_{56}^{(2)} - s_{56}^{(1)} \\ (1 + \frac{1}{v^{(2)}}) s_{66}^{(2)} - s_{66}^{(1)} \\ (1 + \frac{1}{v^{(2)}}) d_{26}^{(2)} - d_{26}^{(1)} \end{pmatrix}. \tag{10g}$$

$$\vec{y}_7 = E_1^{eff} \begin{pmatrix} d_{11}^{(2)} - d_{11}^{(1)} \\ d_{13}^{(2)} - d_{13}^{(1)} \\ d_{14}^{(2)} - d_{14}^{(1)} \\ d_{15}^{(2)} - d_{15}^{(1)} \\ d_{16}^{(2)} - d_{16}^{(1)} \\ \epsilon_{12}^{(2)} - \epsilon_{12}^{(1)} \end{pmatrix}, \quad \vec{y}_8 = \frac{1}{v^{(2)}} E_2^{eff} \begin{pmatrix} d_{21}^{(2)} \\ d_{23}^{(2)} \\ d_{24}^{(2)} \\ d_{25}^{(2)} \\ d_{26}^{(2)} \\ \epsilon_{22}^{(2)} \end{pmatrix}, \tag{10h}$$

$$\vec{y}_9 = E_3^{eff} \begin{pmatrix} d_{31}^{(2)} - d_{31}^{(1)} \\ d_{33}^{(2)} - d_{33}^{(1)} \\ d_{34}^{(2)} - d_{34}^{(1)} \\ d_{35}^{(2)} - d_{35}^{(1)} \\ d_{36}^{(2)} - d_{36}^{(1)} \\ \epsilon_{23}^{(2)} - \epsilon_{23}^{(1)} \end{pmatrix}, \tag{10i}$$

The mechanical stresses $T_{ij}^{(1)}$ and electric field $E_2^{(1)}$ are different in general for these simple loads. Values of mechanical stress and electric field in domain 2 can be expressed from equations (6a)-(6l) using values of corresponding components in domain 1. We can solve the equation (10a) and substitute the results into equations (5a)-(5b) to find the effective material properties for the two-domain system. Detailed procedure is illustrated in the example below.

III. EXAMPLES OF TENSOR PROPERTY AVERAGING FOR A TWIN CRYSTAL WITH THE SAME VOLUME RATIOS OF THE TWO DOMAINS

As an example, we calculate the effective material properties of a $3m$ symmetry class single crystal, such as PZN-PT single crystal, with one set of twins containing equal volume ratios of the two domains. First of all, we need to rotate all tensor components of material properties for both domains from their own material coordinates to the same global coordinate system (material coordinate for the parent cubic structure). Components of material

properties for domains 1 and 2 are rotated to the common coordinate system using matrices

$$\mathbf{R}^{(1)} = \begin{pmatrix} \frac{1}{\sqrt{2}} & \frac{1}{\sqrt{6}} & \frac{1}{\sqrt{3}} \\ -\frac{1}{\sqrt{2}} & \frac{1}{\sqrt{6}} & \frac{1}{\sqrt{3}} \\ 0 & -\frac{2}{\sqrt{6}} & \frac{1}{\sqrt{3}} \end{pmatrix}, \quad \mathbf{R}^{(2)} = \begin{pmatrix} -\frac{1}{\sqrt{2}} & \frac{1}{\sqrt{6}} & \frac{1}{\sqrt{3}} \\ -\frac{1}{\sqrt{2}} & -\frac{1}{\sqrt{6}} & -\frac{1}{\sqrt{3}} \\ 0 & -\frac{2}{\sqrt{6}} & \frac{1}{\sqrt{3}} \end{pmatrix}. \tag{11}$$

Because the prototype symmetry of the paraelectric phase is cubic, the possible DW orientations[18] for the two domains with polarization $P_S[111]$ and $P_S[1\bar{1}1]$ are [010] and [101]. We calculate the effective material properties for the case with DW oriented in [010]. Domains are often observed as periodic twin band in most ferroelectric materials, therefore, it is reasonable to assume the same volume ratios for the two domains, i.e. $v^{(1)} = v^{(2)} = \frac{1}{2}$, the expected symmetry of such a twin structure and its effective material properties is $mm2$.

Independent material properties for $3m$ symmetry class in its own crystallographic coordinate system with the mirror symmetry plane perpendicular to x-axis can be found in Ref.[17].

Material properties for domain 1 in the chosen coordinate system (as plotted in Fig. 1) are

$$\mathbf{s}'^{(1)} = \begin{pmatrix} s'_{11} & s'_{12} & s'_{12} & s'_{14} & s'_{15} & s'_{15} \\ s'_{12} & s'_{11} & s'_{12} & s'_{15} & s'_{14} & s'_{15} \\ s'_{12} & s'_{12} & s'_{11} & s'_{15} & s'_{15} & s'_{14} \\ s'_{14} & s'_{15} & s'_{15} & s'_{44} & s'_{45} & s'_{45} \\ s'_{15} & s'_{14} & s'_{15} & s'_{45} & s'_{44} & s'_{45} \\ s'_{15} & s'_{15} & s'_{14} & s'_{45} & s'_{45} & s'_{44} \end{pmatrix}, \tag{12a}$$

$$\epsilon' = \begin{pmatrix} \epsilon'_{11} & \epsilon'_{12} & \epsilon'_{12} \\ \epsilon'_{12} & \epsilon'_{11} & \epsilon'_{12} \\ \epsilon'_{12} & \epsilon'_{12} & \epsilon'_{11} \end{pmatrix}, \tag{12b}$$

$$\mathbf{d}' = \begin{pmatrix} d'_{11} & d'_{12} & d'_{12} & d'_{14} & d'_{15} & d'_{15} \\ d'_{12} & d'_{11} & d'_{12} & d'_{15} & d'_{14} & d'_{15} \\ d'_{12} & d'_{12} & d'_{11} & d'_{15} & d'_{15} & d'_{14} \end{pmatrix}, \tag{12c}$$

while material properties for the second domain in the same coordinate system can be derived as

$$\mathbf{s}'^{(2)} = \begin{pmatrix} s'_{11} & s'_{12} & s'_{12} & -s'_{14} & s'_{15} & -s'_{15} \\ s'_{12} & s'_{11} & s'_{12} & -s'_{15} & s'_{14} & -s'_{15} \\ s'_{12} & s'_{12} & s'_{11} & -s'_{15} & s'_{15} & -s'_{14} \\ -s'_{14} & -s'_{15} & -s'_{15} & s'_{44} & -s'_{45} & s'_{45} \\ s'_{15} & s'_{14} & s'_{15} & -s'_{45} & s'_{44} & -s'_{45} \\ -s'_{15} & -s'_{15} & -s'_{14} & s'_{45} & -s'_{45} & s'_{44} \end{pmatrix}, \tag{13a}$$

$$\epsilon' = \begin{pmatrix} \epsilon'_{11} & -\epsilon'_{12} & \epsilon'_{12} \\ -\epsilon'_{12} & \epsilon'_{11} & -\epsilon'_{12} \\ \epsilon'_{12} & -\epsilon'_{12} & \epsilon'_{11} \end{pmatrix}. \tag{13b}$$

$$\mathbf{d}' = \begin{pmatrix} d'_{11} & d'_{12} & d'_{12} & -d'_{14} & d'_{15} & -d'_{15} \\ -d'_{12} & -d'_{11} & -d'_{12} & d'_{15} & -d'_{14} & d'_{15} \\ d'_{12} & d'_{12} & d'_{11} & -d'_{15} & d'_{15} & -d'_{14} \end{pmatrix}. \tag{13c}$$

where

$$s'_{11} = \frac{1}{9}(4s_{11} + 4s_{13} + 4\sqrt{2}s_{14} + s_{33} + 2s_{44}) \tag{14a}$$

$$s'_{12} = \frac{1}{9}(s_{11} + 3s_{12} + 4s_{13} - 2\sqrt{2}s_{14} + s_{33} - s_{44}) \tag{14b}$$

$$s'_{14} = \frac{2}{9}(s_{11} - 3s_{12} + s_{13} + \sqrt{2}s_{14} + s_{33} - s_{44}) \tag{14c}$$

$$s'_{15} = \frac{1}{9}(-4s_{11} + 2s_{13} - \sqrt{2}s_{14} + 2s_{33} + s_{44}) \tag{14d}$$

$$s'_{44} = \frac{2}{9}(5s_{11} - 3s_{12} - 4s_{13} - 4\sqrt{2}s_{14} + 2s_{33} + s_{44}) \tag{14e}$$

$$s'_{45} = \frac{1}{9}(-2s_{11} + 6s_{12} - 8s_{13} + 4\sqrt{2}s_{14} + 4s_{33} - s_{44}) \tag{14f}$$

$$d'_{11} = \frac{1}{3\sqrt{3}}(2d_{15} - 2\sqrt{2}d_{22} + 2d_{31} + d_{33}) \tag{14g}$$

$$d'_{12} = \frac{1}{3\sqrt{3}}(-d_{15} + \sqrt{2}d_{22} + 2d_{31} + d_{33}) \tag{14h}$$

$$d'_{14} = -\frac{2}{3\sqrt{3}}(d_{15} + 2\sqrt{2}d_{22} + d_{31} - d_{33}) \tag{14i}$$

$$d'_{15} = \frac{1}{3\sqrt{3}}(d_{15} + 2\sqrt{2}d_{22} - 2d_{31} + 2d_{33}) \tag{14j}$$

$$\epsilon'_{11} = \frac{1}{3}(2\epsilon_{11} + \epsilon_{33}) \tag{14k}$$

$$\epsilon'_{12} = \frac{1}{3}(-\epsilon_{11} + \epsilon_{33}). \tag{14l}$$

As an example, let us apply load 1, i.e. $T_{11}^{eff} \neq 0$, other are all zero (the other loads 2-9 can be solved similarly). The corresponding matrices for the linear systems are

$$\mathbf{A} = \begin{pmatrix} 2s'_{11} & 2s'_{12} & s'_{15} & 0 & 0 & 0 \\ 2s'_{12} & 2s'_{11} & s'_{15} & 0 & 0 & 0 \\ 2s'_{15} & 2s'_{15} & s'_{44} & 0 & 0 & 0 \\ 0 & 0 & 0 & s'_{44} & s'_{45} & 2d'_{15} \\ 0 & 0 & 0 & s'_{45} & s'_{44} & 2d'_{15} \\ 0 & 0 & 0 & d'_{15} & d'_{15} & 2\epsilon'_{11} \end{pmatrix}, \tag{15a}$$

$$\vec{\mathbf{x}}_1 = \begin{pmatrix} T_{11}^{(1)} \\ T_{33}^{(1)} \\ T_{12}^{(1)} \\ T_{32}^{(1)} \\ T_{13}^{(1)} + T_{31}^{(1)} \\ E_2^{(1)} \end{pmatrix}, \tag{15b}$$

$$\vec{y}_1 = (2T_{11}^{eff}) \begin{pmatrix} s'_{11} \\ s'_{12} \\ s'_{15} \\ -s'_{14} \\ -s'_{15} \\ -d'_{12} \end{pmatrix}, \tag{15c}$$

where we reshaped matrix A and vectors $\vec{x}_1, \vec{y}_1$ for convenience. Solution of equation (10a) for our particular case is given by

$$T_{11}^{(1)} = T_{11}^{eff}, \quad T_{33}^{(1)} = 0, \quad T_{13}^{(1)} + T_{31}^{(1)} = 0, \tag{16}$$

$$T_{32}^{(1)} = (-2T_{11}^{eff})\frac{\det \mathbf{B}_1}{\det \mathbf{B}}, \quad T_{12}^{(1)} = (-2T_{11}^{eff})\frac{\det \mathbf{B}_2}{\det \mathbf{B}}, \quad E_2^{(1)} = (-T_{11}^{eff})\frac{\det \mathbf{B}_3}{\det \mathbf{B}}, \tag{17}$$

where

$$\mathbf{B} = \begin{pmatrix} s'_{11} & s'_{15} & d'_{15} \\ s'_{15} & s'_{11} & d'_{15} \\ d'_{15} & d'_{15} & \epsilon'_{11} \end{pmatrix}, \quad \mathbf{B}_1 = \begin{pmatrix} s'_{14} & s'_{45} & d'_{15} \\ s'_{15} & s'_{44} & d'_{15} \\ d'_{12} & d'_{15} & \epsilon'_{11} \end{pmatrix}. \tag{18}$$

$$\mathbf{B}_2 = \begin{pmatrix} s'_{14} & s'_{14} & d'_{15} \\ s'_{15} & s'_{15} & d'_{15} \\ d'_{15} & d'_{12} & \epsilon'_{11} \end{pmatrix}, \quad \mathbf{B}_3 = \begin{pmatrix} s'_{44} & s'_{45} & s'_{14} \\ s'_{45} & s'_{44} & s'_{15} \\ d'_{15} & d'_{15} & d'_{12} \end{pmatrix}. \tag{19}$$

Mechanical stresses in domain 2 are expressed as

$$T_{11}^{(2)} = T_{11}^{eff}, \quad T_{33}^{(2)} = 0, \quad T_{32}^{(2)} = -T_{32}^{(1)}, \tag{20}$$

$$T_{13}^{(2)} + T_{31}^{(2)} = 0, \quad T_{12}^{(2)} = -T_{12}^{(1)}, \quad E_2^{(2)} = -E_2^{(1)}. \tag{21}$$

Now we can substitute these expressions into the averaging conditions (6a)-(6l) and obtain some of the effective material properties for the two-domain system. The same procedure

can be applied to the other loads $2 \rightarrow 9$ and a complete set of effective material properties for the twin structure will be obtained and they are explicitly given below.

$$\mathbf{s}^{eff} = \begin{pmatrix} s_{11}^{eff} & s_{12}^{eff} & s_{13}^{eff} & 0 & s_{15}^{eff} & 0 \\ s_{12}^{eff} & s_{22}^{eff} & s_{12}^{eff} & 0 & s_{25}^{eff} & 0 \\ s_{13}^{eff} & s_{12}^{eff} & s_{11}^{eff} & 0 & s_{35}^{eff} & 0 \\ 0 & 0 & 0 & s_{44}^{eff} & 0 & s_{46}^{eff} \\ s_{15}^{eff} & s_{25}^{eff} & s_{35}^{eff} & 0 & s_{55}^{eff} & 0 \\ 0 & 0 & 0 & s_{46}^{eff} & 0 & s_{44}^{eff} \end{pmatrix}, \tag{22a}$$

$$\epsilon^{eff} = \begin{pmatrix} \epsilon_{11}^{eff} & 0 & \epsilon_{13}^{eff} \\ 0 & \epsilon_{22}^{eff} & 0 \\ \epsilon_{13}^{eff} & 0 & \epsilon_{11}^{eff} \end{pmatrix}. \tag{22b}$$

$$\mathbf{d}^{eff} = \begin{pmatrix} d_{11}^{eff} & d_{12}^{eff} & d_{13}^{eff} & 0 & d_{15}^{eff} & 0 \\ 0 & 0 & 0 & d_{24}^{eff} & 0 & d_{24}^{eff} \\ d_{13}^{eff} & d_{12}^{eff} & d_{11}^{eff} & 0 & d_{15}^{eff} & 0 \end{pmatrix}. \tag{22c}$$

where

$$s_{11}^{eff} = s'_{11} - (s'_{11} \det \mathbf{B}_1 + s'_{15} \det \mathbf{B}_2 + d'_{12} \det \mathbf{B}_3) / \det \mathbf{B} \tag{23a}$$

$$s_{12}^{eff} = s'_{12} - (s'_{15} \det \mathbf{B}_1 + s'_{15} \det \mathbf{B}_2 + d'_{11} \det \mathbf{B}_3) / \det \mathbf{B} \tag{23b}$$

$$s_{13}^{eff} = s'_{12} - (s'_{15} \det \mathbf{B}_1 + s'_{14} \det \mathbf{B}_2 + d'_{12} \det \mathbf{B}_3) / \det \mathbf{B} \tag{23c}$$

$$s_{15}^{eff} = s'_{15} - (s'_{15} \det \mathbf{B}_1 + s'_{45} \det \mathbf{B}_2 + d'_{14} \det \mathbf{B}_3) / \det \mathbf{B} \tag{23d}$$

$$s_{22}^{eff} = s'_{11} - (s'_{15} \det \mathbf{B}_4 + s'_{15} \det \mathbf{B}_5 + d'_{11} \det \mathbf{B}_6) / \det \mathbf{B} \tag{23e}$$

$$s_{25}^{eff} = s'_{14} - (s'_{15} \det \mathbf{B}_4 + s'_{45} \det \mathbf{B}_5 + d'_{14} \det \mathbf{B}_6) / \det \mathbf{B} \tag{23f}$$

$$s_{44}^{eff} = s'_{44} - (s'_{14} \det \mathbf{B}_7 + s'_{15} \det \mathbf{B}_8 + s'_{45} \det \mathbf{B}_9) / \det \mathbf{B}^* \tag{23g}$$

$$s_{46}^{eff} = s'_{45} - (s'_{15} \det \mathbf{B}_7 + s'_{14} \det \mathbf{B}_8 + s'_{45} \det \mathbf{B}_9) / \det \mathbf{B}^* \tag{23h}$$

$$s_{55}^{eff} = s'_{44} - (s'_{15} \det \mathbf{B}_{10} + s'_{45} \det \mathbf{B}_{11} + d'_{14} \det \mathbf{B}_{12}) / \det \mathbf{B} \tag{23i}$$

$$\epsilon_{11}^{eff} = \epsilon'_{11} - (d'_{14} \det \mathbf{B}_{13} + d'_{15} \det \mathbf{B}_{14} + \epsilon'_{12} \det \mathbf{B}_{15}) \,/\, \det \mathbf{B} \tag{23j}$$

$$\epsilon_{13}^{eff} = \epsilon'_{12} - (d'_{15} \det \mathbf{B}_{13} + d'_{14} \det \mathbf{B}_{14} + \epsilon'_{12} \det \mathbf{B}_{15}) \,/\, \det \mathbf{B} \tag{23k}$$

$$\epsilon_{22}^{eff} = \epsilon'_{11} - (d'_{12} \det \mathbf{B}_{16} + d'_{12} \det \mathbf{B}_{17} + d'_{14} \det \mathbf{B}_{18}) \,/\, \det \mathbf{B}^* \tag{23l}$$

$$d_{11}^{eff} = d'_{11} - (s'_{14} \det \mathbf{B}_{13} + s'_{15} \det \mathbf{B}_{14} + d'_{12} \det \mathbf{B}_{15}) \,/\, \det \mathbf{B} \tag{23m}$$

$$d_{12}^{eff} = d'_{12} - (s'_{15} \det \mathbf{B}_{13} + s'_{15} \det \mathbf{B}_{14} + d'_{11} \det \mathbf{B}_{15}) \,/\, \det \mathbf{B} \tag{23n}$$

$$d_{13}^{eff} = d'_{12} - (s'_{15} \det \mathbf{B}_{13} + s'_{14} \det \mathbf{B}_{14} + d'_{12} \det \mathbf{B}_{15}) \,/\, \det \mathbf{B} \tag{23o}$$

$$d_{15}^{eff} = d'_{15} - (s'_{15} \det \mathbf{B}_{13} + s'_{45} \det \mathbf{B}_{14} + d'_{14} \det \mathbf{B}_{15}) \,/\, \det \mathbf{B} \tag{23p}$$

$$d_{24}^{eff} = d'_{15} - (s'_{14} \det \mathbf{B}_{16} + s'_{15} \det \mathbf{B}_{17} + s'_{45} \det \mathbf{B}_{18}) \,/\, \det \mathbf{B}^* \tag{23q}$$

where

$$\mathbf{B}^* = \begin{pmatrix} s'_{11} & s'_{12} & s'_{15} \\ s'_{12} & s'_{11} & s'_{15} \\ s'_{15} & s'_{15} & s'_{14} \end{pmatrix}, \quad \mathbf{B}_4 = \begin{pmatrix} s'_{15} & s'_{45} & d'_{15} \\ s'_{14} & s'_{44} & d'_{15} \\ d'_{11} & d'_{15} & \epsilon'_{11} \end{pmatrix}, \tag{24a}$$

$$\mathbf{B}_5 = \begin{pmatrix} s'_{11} & s'_{15} & d'_{15} \\ s'_{15} & s'_{15} & d'_{15} \\ d'_{15} & d'_{11} & \epsilon'_{11} \end{pmatrix}, \quad \mathbf{B}_6 = \begin{pmatrix} s'_{44} & s'_{45} & s'_{15} \\ s'_{45} & s'_{44} & s'_{15} \\ d'_{15} & d'_{15} & d'_{11} \end{pmatrix}, \tag{24b}$$

$$\mathbf{B}_7 = \begin{pmatrix} s'_{11} & s'_{12} & s'_{15} \\ s'_{15} & s'_{11} & s'_{15} \\ s'_{15} & s'_{15} & s'_{14} \end{pmatrix}, \quad \mathbf{B}_8 = \begin{pmatrix} s'_{11} & s'_{14} & s'_{15} \\ s'_{12} & s'_{15} & s'_{15} \\ s'_{15} & s'_{45} & s'_{44} \end{pmatrix}, \tag{24c}$$

$$\mathbf{B}_9 = \begin{pmatrix} s'_{11} & s'_{12} & s'_{14} \\ s'_{12} & s'_{11} & s'_{15} \\ s'_{15} & s'_{15} & s'_{45} \end{pmatrix}, \quad \mathbf{B}_{10} = \begin{pmatrix} s'_{45} & s'_{45} & d'_{15} \\ s'_{45} & s'_{44} & d'_{15} \\ d'_{14} & d'_{15} & \epsilon'_{11} \end{pmatrix}, \tag{24d}$$

$$\mathbf{B}_{11} = \begin{pmatrix} s'_{14} & s'_{45} & d'_{15} \\ s'_{15} & s'_{45} & d'_{15} \\ d'_{15} & d'_{14} & \epsilon'_{11} \end{pmatrix}, \quad \mathbf{B}_{12} = \begin{pmatrix} s'_{44} & s'_{45} & s'_{45} \\ s'_{45} & s'_{44} & s'_{45} \\ d'_{15} & d'_{15} & d'_{14} \end{pmatrix}. \tag{24e}$$

$$\mathbf{B}_{13} = \begin{pmatrix} d'_{14} & s'_{45} & d'_{15} \\ d'_{15} & s'_{44} & d'_{15} \\ \epsilon'_{12} & d'_{15} & \epsilon'_{11} \end{pmatrix}, \quad \mathbf{B}_{14} = \begin{pmatrix} s'_{44} & d'_{14} & d'_{15} \\ s'_{45} & d'_{15} & d'_{15} \\ d'_{15} & \epsilon'_{12} & \epsilon'_{11} \end{pmatrix}, \tag{24f}$$

$$\mathbf{B}_{15} = \begin{pmatrix} s'_{44} & s'_{45} & d'_{14} \\ s'_{45} & s'_{44} & d'_{15} \\ d'_{15} & d'_{15} & \epsilon'_{12} \end{pmatrix}, \quad \mathbf{B}_{16} = \begin{pmatrix} d'_{12} & s'_{12} & s'_{15} \\ d'_{12} & s'_{11} & s'_{15} \\ d'_{14} & s'_{15} & s'_{44} \end{pmatrix}, \tag{24g}$$

$$\mathbf{B}_{17} = \begin{pmatrix} s'_{11} & d'_{12} & s'_{15} \\ s'_{12} & d'_{12} & s'_{15} \\ s'_{15} & d'_{14} & s'_{44} \end{pmatrix}, \quad \mathbf{B}_{18} = \begin{pmatrix} s'_{11} & s'_{12} & d'_{12} \\ s'_{12} & s'_{11} & d'_{12} \\ s'_{15} & s'_{15} & d'_{14} \end{pmatrix}. \tag{24h}$$

The symmetry of these effective material properties is at least $mm2$. Some may show degeneracy in certain components.

Similar calculation can be carried out for any arbitrary material symmetry and arbitrary orientation of domains and DW.

IV. NUMERICAL EXAMPLES FOR m3m — 3m AND m3m — 4mm FERROELECTRIC SPECIES

In order to make some comparison between our method and the volume ratio weighted average, we have performed numerical computation for two systems that have experimental data available in the single domain single crystal state. Unfortunately, the lack of experimental results prevented us from directly compare to measured data for a two-domain twin band system. The two systems calculated represent domains formed at the ferroelectric phase transitions of $m3m - 3m$ ($LiNbO_3$) and $m3m - 4mm$ ($BaTiO_3$).

According to Ref.[8], if the effective material properties could be calculated based on volume ratio weighted average, the effective material properties can have very a compact form. In vector notation, the effective material properties of a two-domain system are given by a 9x9 matrix

$$\mathbf{M} = \begin{pmatrix} \mathbf{s} & \mathbf{d}^T \\ \mathbf{d} & \epsilon \end{pmatrix}, \tag{25}$$

where $\mathbf{s}$ is a 6x6 matrix of the elastic compliances. $\mathbf{d}$ is a 6x3 matrix of piezoelectric constants and ϵ is a 3x3 matrix of the dielectric constant. Because the volume ratio weighting method eliminated the cross coupling between domain 1 and domain 2 and ignored the orientation effect. the effective material properties can be simply expressed as

$$\mathbf{M} = \left(\mathbf{M}^{(1)}(\mathbf{m}^{(1)})^{-1}\mathbf{m}^{(2)} + \frac{v^{(2)}}{v^{(1)}}\mathbf{M}^{(2)}\right)\left((\mathbf{m}^{(1)})^{-1}\mathbf{m}^{(2)} + \frac{v^{(2)}}{v^{(1)}}\mathbf{I}\right)^{-1}. \tag{26}$$

where $\mathbf{M}^{(1)}$ and $\mathbf{M}^{(2)}$ are matrices of material properties of both domains and $\mathbf{I}$ is a 9x9 unit matrix. The matrices $\mathbf{m}^{(1)}$ and $\mathbf{m}^{(2)}$ are given by

$$\mathbf{m}^{(i)} = \begin{pmatrix} s_{11}^{(i)} & s_{12}^{(i)} & s_{13}^{(i)} & s_{14}^{(i)} & s_{15}^{(i)} & s_{16}^{(i)} & d_{11}^{(i)} & d_{21}^{(i)} & d_{31}^{(i)} \\ 0 & 1 & 0 & 0 & 0 & 0 & 0 & 0 & 0 \\ s_{13}^{(i)} & s_{23}^{(i)} & s_{33}^{(i)} & s_{34}^{(i)} & s_{35}^{(i)} & s_{36}^{(i)} & d_{13}^{(i)} & d_{23}^{(i)} & d_{33}^{(i)} \\ 0 & 0 & 0 & 1 & 0 & 0 & 0 & 0 & 0 \\ s_{15}^{(i)} & s_{25}^{(i)} & s_{35}^{(i)} & s_{45}^{(i)} & s_{55}^{(i)} & s_{56}^{(i)} & d_{15}^{(i)} & d_{25}^{(i)} & d_{35}^{(i)} \\ 0 & 0 & 0 & 0 & 0 & 1 & 0 & 0 & 0 \\ 0 & 0 & 0 & 0 & 0 & 0 & 1 & 0 & 0 \\ d_{21}^{(i)} & d_{22}^{(i)} & d_{23}^{(i)} & d_{24}^{(i)} & d_{25}^{(i)} & d_{26}^{(i)} & \epsilon_{12}^{(i)} & \epsilon_{22}^{(i)} & \epsilon_{23}^{(i)} \\ 0 & 0 & 0 & 0 & 0 & 0 & 0 & 0 & 1 \end{pmatrix}, \quad i = 1, 2. \tag{27}$$

Numerical values for two a domain system of $LiNbO_3$ and $BaTiO_3$ calculated using this approach (labeled as Ref.[8]) are listed in Table I to compare with the numerical values obtained by using the method given in this paper (also listed in Table I).

V. DISCUSSION AND CONCLUSIONS

It is important to point out that the global symmetry of the twin structure is maintained no matter if the intercoupling between the two domains has been considered. For the case of $LiNbO_3$ ($m3m - 3m$). the symmetry belongs to $mm2$ class. For $BaTiO_3$ ($m3m \rightarrow 4mm$)

the symmetry of the system is also $mm2$, but there are additional degeneracy for some material properties. They are: $s_{11}^{eff} = s_{22}^{eff}, s_{13}^{eff} = s_{23}^{eff}$, and $s_{44}^{eff} = s_{55}^{eff}$. Using the method in Ref.[8], only two of the degenerate relations $s_{11}^{eff} = s_{22}^{eff}, s_{13}^{eff} = s_{23}^{eff}$ hold for the elastic compliance tensor.

From Table I, the difference in elastic properties calculated using these two methods is small. This is because the elastic properties of the two variants are very similar. the intercoupling effect is not significant. The difference is much larger in the piezoelectric and dielectric constants for lower symmetry systems. For $LiNbO_3$, the calculated piezoelectric coefficient d_{13} using these two methods differ by more than 100% and the dielectric coefficient ϵ_{13} even have different signs. It appears that the difference becomes smaller for higher symmetry systems. For the $4mm$ symmetry $BaTiO_3$, the difference is within a few percent for most of the quantities. Therefore, the volume ratio averaging method could give good predictions on the effective properties for higher symmetry systems but may run into problems for lower symmetry systems.

In summary, we have reported in this paper a general procedure to calculate the effective material properties of a two variant twin structures. The method has taken into account specifically all the boundary conditions and used more realistic relations for each individual tensor component rather than using a unified volume ratio averaging scheme. This procedure requires to solve two sets of linear systems of equations and could be easily implemented using computer. The equations are all linear which can be solved without much difficulties.

In order to compare to the volume averaging scheme, we have calculated two systems with polar symmetries of $3m$ and $4mm$ using both methods. It was found that the new method gives similar results for a $4mm$ system but predict quite different piezoelectric and dielectric coefficients for 3m systems. In some components, the difference can exceed 100%. The elastic properties, however, differ very little for both symmetries because the two type of domains are very similar in elastic properties, the coupling of the two domains does not make significant difference while performing the property average.

Two variant twins are the basis of all twin structures as revealed by all microscopy

works. Properly calculate the effective property of the two variant twins will pave a way to calculate more complicated multi-domain single crystal ferroelectric systems more precisely rather than using the less rigorous statistical approach.

ACKNOWLEDGMENT

This work was supported by the National Science Foundation under Grant No. DNS 9704714 and by the Office of Naval Research under the Grant No. N00014-98-1-0527. One of the authors (J.E.) is also grateful for partial support from Ministry of Education of the Czech Republic (Code VS 96006. 1996).

REFERENCES

[1] R. C. DeVries, J. E. Burke, J. Am. Ceram. Soc. **40**, (1957), pp. 200-206

[2] G. Arlt, P. Sasko, J. Appl. Phys. **51**, 9 (1980), pp.4956-4960

[3] S. E. Park, T. Shrout, J. Appl. Phys. **82**, 4 (1997), pp.1804-1811

[4] J. Yin, W. Cao, to be published

[5] M. L. Mulvihill, L.E.Cross, W.Cao, K.Uchino, J. Am. Ceram. Soc. **80**, 6 (1997), pp.1462-1468

[6] M. L. Mulvihill, K.Uchino, Z.Li, W.Cao, Phil. Mag. **74**, 1 (1996), pp. 25-36

[7] M. Grimsditch, F. Nizzolli, Phys. Rev. **B33**, 8 (1986), pp.5891-5892

[8] E. Aksakaya, G. W. Farnell, J. Appl. Phys. **64**, 9 (1988), pp.4469-4473

[9] E. Aksakaya, G. W. Farnell, E. L. Adler, J. Appl. Phys. **68**, 3 (1990), pp. 1009-1012

[10] Ce-Wen Nan, D. R. Clarke, J. Am. Ceram. Soc. **79**, 10 (1996), pp.2563-2566

[11] T. Olson, M. Avellaneda, J. Appl. Phys. **71**, 9 (1992), pp.4455-4464

[12] N. A. Pertsev, A. G. Zembilgotov, R. Waser, J. Appl. Phys. **84**, 3 (1998), pp. 1524-1529

[13] Ce-Wen Nan, J. Appl. Phys. **76**, 2 (1994), pp. 1155-1163

[14] M. L. Dunn, M. Taya, Int. J. Solids Structures **30.2** (1993), pp.161-175

[15] W. Cao, Q. M. Zhang, L. E. Cross, IEEE Trans. Ultrason. Ferroel. Freq. Contr. **40**, 2 (1993), pp.103-109

[16] W. A. Smith, A. Shaulov, B. A. Auld, in *Proc. IEEE Ultrason. Symp. 1985*, pp.642-647

[17] J. F. Nye, *Physical Properties of Crystals* (Clarendon Press, Oxford, 1957)

[18] J. Fousek, V. Janovec, J. Appl. Phys. **40**, 1 (1969), pp.135-142

FIGURES

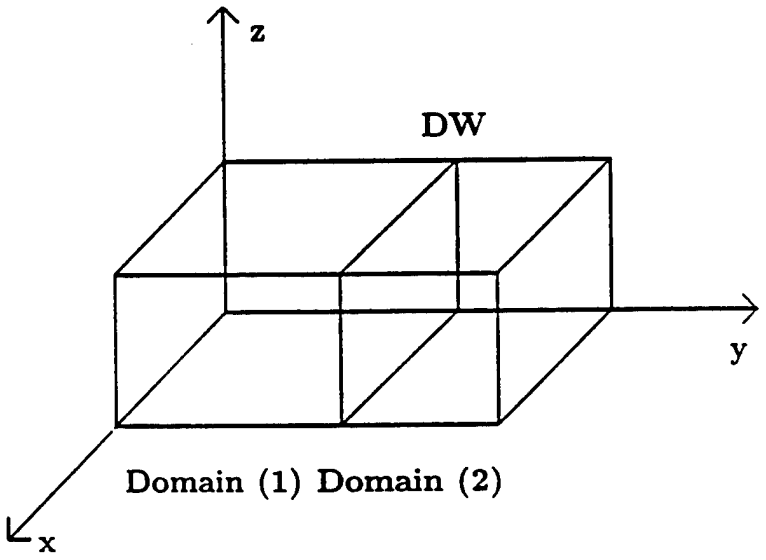

FIG. 1. The two domain system with coordinate systems chosen with the y-axis perpendicular to the domain wall (DW).

TABLES

TABLE I. Effective material properties for two variant twin structure of $LiNbO_3$ and $BaTiO_3$. The coordinate system is chosen in the way that the y-axis is perpendicular to the DW. Zero values of tensor components are listed by dots.

Material		$LiNbO_3$ DW(010)				$BaTiO_3$ DW(110)			
property		P_S[111]	P_S[1$\bar{1}$1]	This work	Ref.[8]	P_S[100]	P_S[010]	This work	Ref.[8]
$S_{\alpha\beta}$	11	5.60	5.60	5.42	5.50	7.92	7.92	7.49	7.92
$[10^{-12}m^2N^{-1}]$	12	-1.36	-1.36	-1.10	-1.08	-1.28	-1.28	-1.71	-1.28
	13	-1.36	-1.36	-1.38	-1.46	-3.80	-3.80	-3.47	-3.79
	14	-1.35	1.35	...	...	...	...	...	...
	15	0.26	0.26	-0.49	-0.53	...	...	...	...
	16	0.26	-0.26	...	...	3.83	-3.83	...	...
	22	5.60	5.60	4.65	4.84	7.92	7.92	7.49	7.92
	23	-1.36	-1.36	-1.10	-1.08	-3.80	-3.80	-3.47	-3.79
	24	0.26	-0.26	...	...	...	...	...	...
	25	-1.35	-1.35	1.36	0.87	...	...	...	...
	26	0.26	-0.26	...	...	3.83	-3.83	...	...
	33	5.60	5.60	5.42	5.50	8.05	8.05	7.81	8.05
	34	0.26	-0.26	...	...	...	...	...	...
	35	0.26	0.26	-0.49	-0.53	...	...	...	...
	36	-1.35	1.35	...	...	-2.89	2.89	...	...
	44	15.65	15.65	15.27	15.27	13.62	13.62	11.94	11.94
	45	-0.98	0.98	...	...	4.78	-4.78	...	...
	46	-0.98	-0.98	-0.99	-0.99	...	...	...	...
	55	15.65	15.65	7.92	9.22	13.62	13.62	11.94	13.62
	56	-0.98	0.98	...	...	...	...	...	...
	66	15.65	15.65	15.27	15.27	34.23	34.23	30.63	30.63
$d_{i\alpha}$	11	16.28	16.28	11.84	15.53	-157	157	...	...

$d_{i\alpha}$	11	16.28	16.28	11.84	15.53	-157	157	...	...
$[10^{-12}\mathrm{CN}^{-1}]$	12	-5.83	-5.83	-5.03	-3.74	121	-121	...	...
	13	-5.83	-5.83	-3.14	-6.58	24	-24	...	...
	14	-47.11	47.11	...	...	...	...	...	...
	15	26.44	26.44	23.84	20.40	...	...	...	...
	16	26.44	-26.44	...	...	-85	-85	-127	-127
	21	-5.83	5.83	...	...	121	121	130	121
	22	16.28	-16.28	...	...	-157	-157	-147	-157
	23	-5.83	5.83	...	...	24	24	17	24
	24	26.44	26.44	22.23	22.23	...	...	...	...
	25	-47.11	47.11	...	...	...	...	...	...
	26	26.44	26.44	22.23	22.23	-85	85	...	...
	31	-5.83	-5.83	-3.14	-6.58	...	...	...	...
	32	-5.83	-5.83	-5.03	-3.74	...	...	...	...
	33	16.28	16.28	11.84	15.53	...	...	...	...
	34	26.44	-26.44	...	...	-277	-277	-179	-180
	35	26.44	26.44	23.84	20.40	-277	277	...	...
	36	-47.11	47.11	...	...	...	...	...	...
ϵ_{ij}	11	3.45	3.45	1.68	3.40	135	135	24.1	24.1
$[10^{-10}\mathrm{Fm}^{-1}]$	12	-0.44	0.44	...	...	-121	121	...	...
	13	-0.44	-0.44	1.04	-0.50	...	...	...	...
	22	3.45	3.45	1.91	1.92	135	135	133.3	135.5
	23	-0.44	0.44	...	...	...	...	...	...
	33	3.45	3.45	1.68	3.40	256	256	199.6	199.6

APPENDIX 74

Preprint of the paper presented at IEEE '98, Sendai, Japan.

Domain Formation in 0.90 Pb($Zn_{1/3}$ $Nb_{2/3}$)O_3 – 0.10$PbTiO_3$ Single Crystals under Electric Field along [111] Direction

Uma Belegundu, M. Pastor, X. H. Du, L. E. Cross and Kenji Uchino

International Center for Actuators and Transducers,
Materials Research Laboratories, The Pennsylvania State University, USA

Abstract: Domain switching has been observed in the 0.9PZN – O.1PT single crystals with electric field along [111] direction. Their formation as the temperature is reduced is discussed here. It is shown that these are remarkably similar to the domains formed, when the temperature is fixed and the concentration of PT varied. This may partly explain the high k values obtained in these crystals.

INTRODUCTION

Relaxor materials such as Pb($Zn_{1/3}Nb_{2/3}$)O_3 (PZN), Pb($Mg_{1/3}$ $Nb_{2/3}$)O_3 (PMN), Pb($Sc_{1/3}Nb_{2/3}$)O_3 (PSN) and their solid solutions with $PbTiO_3$ have come into prominence due to their very high electromechanical coupling factors k[1,2,3,4]. Strain rates of 1.7% have been observed[2, 3] in such single crystals. Currently, these materials are being studied intensively for actuator / transducer applications in medical imaging. Among the materials mentioned above, the solid solution of Pb($Zn_{1/3}$ $Nb_{2/3}$)O_3 - $PbTiO_3$ (PZN -PT) single crystals have the highest reported value of piezoelectric coefficient $d_{33} \cong 2000$ pC/N and electromechanical coupling factors $k_{33} \cong 94\%$ [1,2] . The phase diagram for this system is shown in Fig.1. One of the end members of the system is a relaxor. The relaxor ferroelectrics are characterized by large frequency dependence of the permittivity, broad phase transition region, tapering off of the polarization charge. The other end member, lead titanate, (PT) is a regular ferroelectric characterized by the sharp phase transition and frequency independent permittivity. The solid solution of this system forms a morphotropic phase boundary (MPB) near PT = 0.09 which shows the high values of k_{33}, d_{33} and elastic compliances[5]. An issue of great importance is the direction in which the crystal must be poled to obtain the highest k_{33} value. These values are obtained when the crystals of rhombohedral composition are poled along [001]. The spontaneous polarization direction for the rhombohedral compositions is along [111] and for tetragonal compositions is along [001]. However, the mechanism relating this poling direction and k-value is not very clear. Two aspects for this explanation can be considered- the crystal orientation dependence of the piezoelectric properties and the domain motion in relaxor ferrolectrics and possibly their behavior under the electric field.

Phenomenological calculations[6] for orientation dependence of piezoelectric properties have been calculated for the PZT system. These show that the maximum k_{33}, and d_{33} occur in the direction canted about 50°–60°from the spontaneous polarization direction for the rhombohedral PZT.

Domain motions in relaxor ferroelectrics contribute towards the piezoelectric properties. The relation between the dielectric property and the domain motion was shown for pure PZN[7]. A large dielectric relaxation was observed over a wide temperature for unpoled crystal. On poling, the dielectric dispersion occurs over a narrow temperature range, showing that a micro to macro

domain change takes place under the influence of electric field. In the present paper, domain motion under the influence of electric field is discussed for crystals of composition 0.90PZN - 0.10 PT (near MPB).

EXPERIMENTAL DETAILS

Single crystals of 0.90PZN - 0.10PT were grown by flux method. Crystallographic direction [111] and [110] were then determined using a Laue x – ray diffractometer. The crystal was then thinned down to 90 μm. Sputtered gold was used as electrodes. The plane of the Figures shown in 2e – 2h are perpendicular to [110], and the [111] direction lies along top to bottom in the plane of the figure. Electric field was applied along [111]through the surface electrode gap.

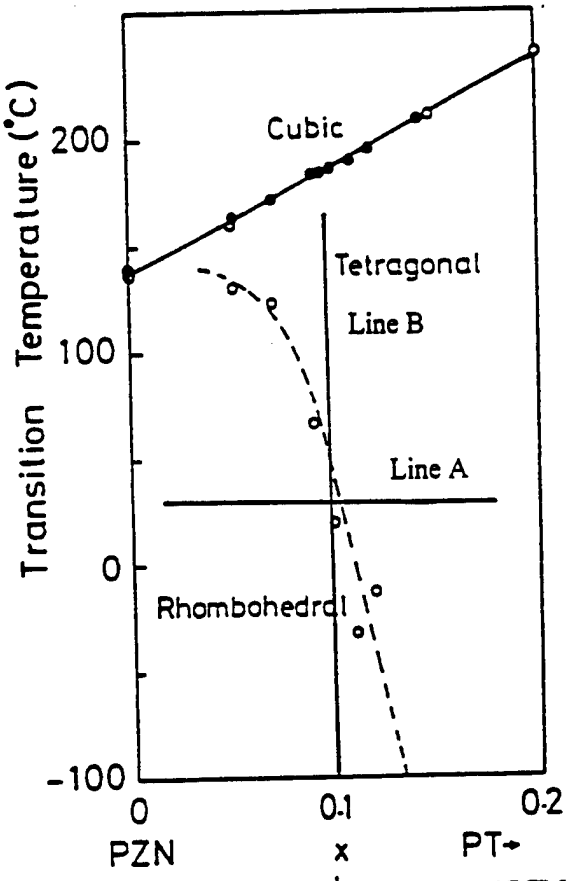

Figure 1. Phase diagram[1] of the (1-x)PZN - xPT system near the MPB region. The changes in the domain configuration along lines A and B are discussed in this paper.

RESULTS

The present crystal consisted of a mixture of two phases; rhombohedral and tetragonal. The rhombohedral domains have spindle like morphology and the tetragonal domains show clear stripe pattern.

Figures 2a – 2d show the domain evolution as the concentration of PT is changed from x = 0.20 to 0 in (1-x)PZN – x PT single crystals. All the figures were taken[8] at room temperature with the field of 12kV/cm essentially following the line A in Fig. 1. Fig. 2a is for x = 0.2 and shows clearly the tetragonal domains formed. As the x is reduced to 0.11 (Fig. 2b) and x = 0.05 (Fig 2c), the configuration becomes more complex. The domain pattern consists of stripes and the spindles showing the co-existence of both the phases.

Figures 2e – 2h show the typical domain configuration observed during switching while reducing temperature for 0.90PZN – 0.10 PT single crystals. The field value is 3 kV/cm. When the temperature is reduced without the applied field domain appear at 224° C, the co- existence region occurs between room temperature and 110° C. Below room temperature, the number density of rhombohedral increases as expected from the phase diagram in Fig. 1.

Figures 2e – 2h essentially follows the line B in Fig. 1. At a very high temperature, clear stripe patterns corresponding to the tetragonal state was observed only at the zero field value of the electric field cycle as the field is applied along [111] direction. As the temperature was reduced to 75°C, corresponding to co-existence region, the stripe pattern disappeared and long spindle like domains with a high aspect ratio and oriented along [111] was observed. During an electric field cycle, these domains switched between the top and the bottom surface of the crystal: domains that were darker during the positive value of the field became lighter during the negative value of the field. The switching of these domains became slower as the temperature was reduced. Also, the sharpness of these domains reduced with decreasing temperature. Instead, small spindle like domains

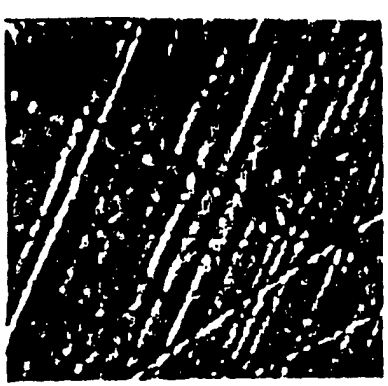

a) x = 0.20

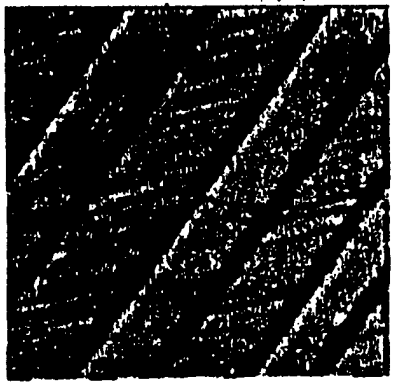

b) x = 0.11

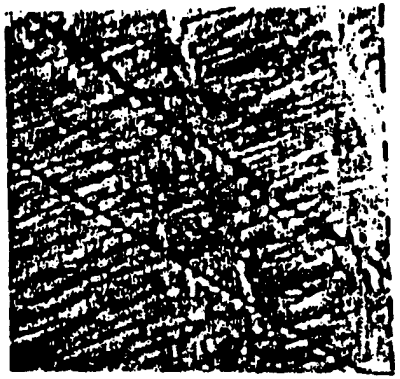

c) x = 0.05

d) x = 0.0

e) T = 220°C

f) T = 76°C

g) T = 25°C

h) T = -40°C

Figure 2 a) - d) Changes in the domain configuration in (1-x) PZN - x PT with varying amounts of x (PT) content at room temperature with field 12kV/cm along [111] Data taken from Ref. 8

2 e) - h) Changes in the domain configuration in 0.90PZN - 0.10PT with decreasing temperature T and field of 3kV/cm along [111]. Present data

with a smaller aspect ratio emerged in between and almost perpendicular to the larger domains. The switching of these smaller domains occur in wave like fashion during the maximum value of the field. The switching speed reduced as the temperature was reduced. The domains oriented along [111] disappeared completely and were replaced by domains of a smaller aspect ratio. A typical domain configuration is shown for -40°C. The domain motion was frozen below -30°C.

The similarities between the two sets of the domain configuration are quite clear. Figures 2a to 2d show the domain configuration for decreasing amount of PT content from x = 0.20 to x = 0.0 (PZN); Figures 2e to 2h show the changes in the domain configuration while changing the temperature for one composition of x = 0.10. Clear stripe patterns corresponding to the tetragonal phase are observed at room temperature for high content of PT (x = 0.2) and at high temperature (223 °C) for x = 0.10 (MPB composition). As the temperature is lowered, small spindles with a smaller aspect ratio are observed in between the spindles having a larger aspect ratio corresponding to the domain pattern for composition x = 0.05 and finally, only the smaller domains remain at very low temperatures which corresponds to the domain pattern of pure PZN.

SUMMARY

It can be summarized that the domain evolution with field along [111] and reducing temperature for 0.90PZN - 0.10 PT crystals are similar to that formed at a constant temperature and decreasing amount of PT content in the crystals. This type of domain hierarchy in combination with the crystal orientation dependence of piezoelectric properties may be the contributing factors for the high *k* observed in these materials. Further studies are required to quantify these results.

ACKNOWLEDGEMENTS:

This work is being supported by Office of Naval Research, USA through contract N00014-91-J-4145

REFERENCES

1) J. Kuwata, K. Uchino and S. Nomura, Ferroelectrics, vol. 37, p579 (1981)
2) S. E. Park and T. R. Shrout, J. Mateer, Res. Innovations vol.1, p20 (1997)
3) T. R. Shrout, Z. P. Chang, N. Kim and S. Markgraf, Ferroelectrics Letter Section, vol. 12, p63 (1990c)
4) Y. Yamashita, Jpn. J. Appl. Phys., vol. 33, p5328 (1994)
5) J. Kuwata, K. Uchino and S. Nomura, Jpn. J. Appl. Phys., vol. 21, p1298 (1982)
6) X. H. Du, U. Belegundu and K .Uchino, Jpn. J. Appl. Phys., vol. 36, p5580 (1997)
7) M. L. Mulvihill, L. E. Cross and K. Uchino, Proc. 8th European mtg. On Ferroelectrics, Ferroelectrics vol. 186, p325 (1996)
8) R. Ujiie and K. Uchino, Proc. IEEE Ultrasonic Symp. '90, Hawaii, vol. 2, p 725 (1991)

APPENDIX 75

Pyroelectric and Piezoelectric Imaging of Ferroelectric Domains in $LiTaO_3$ by Scanning Electron Microscopy

Shining Zhu* and Wenwu Cao

Materials Research Laboratory, The Pennsylvania State University

University Park, Pennsylvania 16802

Abstract

Ferroelectric domains of a $LiTaO_3$ single crystal were directly observed by the scanning electron microscopy (SEM) on its polished polar surface without metal coating. Two kinds of domain contrast were found with slow scan rate under the conditions of cathode voltage V_0=5kV and probe current $I_b=8\times10^{-11}$A. These two kinds of contrast are antiparallel domains and domain boundaries that appeared at the initial and subsequent frames of scanning, respectively. The formation of these two different kinds of contrast is explained as pyroelectric and piezoelectric effects.

PACS: 77.70.+a, 77.22.Ej, 77.84.-s, 61.16.Bj

*Permanent address: National Laboratory of Solid State Microstructures and Physics Department, Nanjing University, Nanjing , 210093, People's Republic of China.

I. INTRODUCTION

Visualization of domains by using scanning electron microscopy (SEM) and investigating effects of surface charge deposition in ferroelectric crystals have gained broad interests in both physics and material science communities in recent years[1-4]. This is attributed to its promising potential of resolving several problems in the observation of engineered domains in nonlinear optical and ultrasonic materials[5,6]. One may also gain more physical insight into the behaviors of ferroelectric crystals under the electron-irradiation on the surface. Investigation of several ferroelectric crystals using SEM had been made with low electron energy of $E \approx 1\sim5$ keV[1,7]. For most ferroelectric, the secondary electron emission yield is close to one within this energy range. The obstacle of obtaining imaging using SEM, i.e. charge accumulation on the surface of insulation materials, may be overcome under this low energy condition. Recently, we have successfully observed domain contrast using environmental scanning electron microscopy (ESEM) using an ion conduction charge neutralization mechanism[8]. The domain contrast image from ESEM can be kept stable at the condition of 2 Torr chamber pressure and a 30 kV accelerating voltage.

Aside from the depolarization field influence to the secondary-electron emission, other physical effects provided by the non-centersymmetry characteristics, such as the pyroelectric and piezoelectric, also have influence on the electron emission rate in ferroelectric materials. It is expected that surface charge accumulation on insulating crystals can lead to the formation of different kinds of domain images under certain conditions.

II. EXPERIMENTAL PROCEDURE

In this paper we analyze in detail an in situ observation of ferroelectric domains and the evolution of the image using SEM technique in a polished c-cut $LiTaO_3$ (LT) single crystal plate. Consider the situation shown in Figure 1. The LT sample is 0.5 mm thick with a pair of parallel surfaces. The bottom surface was loosely fixed to a conducting holder and the electron probe of current I_b was radiated into the sample from the top surface. The cathode voltage was set at V_0. The conducting sample holder was connected to the ground.

The irradiated surface emitted secondary- and backscatter-electrons. The total emitted electron coefficient $\delta+\eta$ as a function of acceleration voltage V_a of probe electrons is shown in figure 2, where δ and η are the yields of secondary- and backscattered-electrons, respectively. If the cathode voltage $V_0 = V_2$, where V_2 is the voltage of the equilibrium point at which $\delta+\eta = 1$, the charges injected to the sample by the probe are the same as total emitted electrons, thus, no net charge accumulation occur in the sample. If $V_0>V_2$, then $\delta+\eta < 1$, the sample will be charged negatively, i.e., more electrons are injected than emitted until $V_a = V_0 - V_s = V_2$. If $V_0 < V_2$, more electrons are emitted before reaching the same condition of $V_a = V_2$ and the sample will be charged positively. Under parallel plate capacitance approximation, the electric potential of the top surface can be written as $V_s = ql/\varepsilon\varepsilon_0 a^2$, where q, l and a are surface charge, sample thickness and the beam radius, respectively; ε and ε_0 are, respectively, the relative dielectric constant and free space permittivity. For $\delta+\eta \neq 1$, the effective potential from the cathode to the sample surface V_a is equal to $V_0+|V_s|$ for $V_s > 0$ and $V_0- |V_s|$ for $V_s< 0$[9,10].

In our experiment, the LT sample with 180° anti-parallel domains was fabricated by field poling method on a single domain single crystal at room temperature [11]. The poled sample was first etched. Some positive domains with triangular shape on the -c face were confirmed by optical microscopy. Second, the etched surface was re-polished to remove the topographic domain patterns and the sample was put into the SEM chamber. The SEM observations were performed with the scan rate of 20 second(s) per frame using a "JEOL JSM-6300" scanning electron microscope in the secondary electron emission mode. The experimental conditions are as follows: chamber pressure $p < 10^{-6}$ Torr, probe current $I_b = 8\times10^{-11}$A and the cathode voltage $V_0 = 5$ kV. The small probe current ensures a longer effective observation time. The voltage $V_0>V_2$ since we found that the sample surface was gradually charged negatively during the scan.

III. RESULTS AND DISCUSSION

Two kinds of SEM contrast images were obtained at the above experimental conditions. The first kind was a brightness contrast between the positive and negative domains, and the second is domain boundary contrast. The first kind of contrast was

shown only at the initial frame of electron probe scanning. The image of positive domains was brighter than that of negative domains as shown in Fig. 3. This means that the secondary electron emission yield from the surface of positive domains is larger than that from the surface of negative domains. In subsequent frames, the first kind of contrast disappeared completely leaving only the second kind-- domain boundary contrast. Shown in Fig.4 is a topographic image with the surface of positive domain higher than that of negative domains. The topographic origin of the image can be seen from the shadowing effect in Fig.4, i.e., one side of the boundary is brighter and the opposite side is darker. Similar result was also reported by Roseman et al. from the SEM observation of KTP [12]. These two kinds of contrast are of different physical origin as analyzed in more detail below.

III.1. *Pyroelectric imaging*

The average energy per incident electron is $E_a=eV_a$ before they entering the sample. A portion of this energy is used to excite the secondary electrons, backscattered-electrons and X-ray. While the major portion of this energy was absorbed by the sample and it converted into heat. Since the thermal conductivity of the sample is finite, there will be some temperature difference, ΔT, between the irradiated region and the rest of the sample. This temperature rise may be estimated using the follow formula:

$$\Delta T = \frac{t_d\{[I_b(E_a - \delta \bar{E}_s - \eta \bar{E}_b)/e] - \bar{A}_x - \bar{B}_T\}}{v\rho c_p} \qquad (1)$$

where I_b is the probe current, e = 1.60×10^{-19}C is the basic charge unit, v =$\pi a^2 h$ is the irradiated volume, h is the penetration depth of the electron, c_p is the heat capacity per unit volume, ρ is the density of crystal, $\bar{E}_s$ and $\bar{E}_b$ are the average energies of secondary- and backscattered-electrons, and $\bar{A}_x$ and $\bar{B}_T$ are the energy losses related to the X-ray generation and thermal conduction, respectively. The dwell time t_d of the probe can be evaluated from $t_d = \frac{2t_l a}{l_s}$, here l_s and t_l are the line scan length and line scan time, respectively. In Eq.(1), the product $t_d I_b E_a/e$ is the incident energy of probe electrons,

which could be estimated from the experimental parameters. Without efficient thermal conduction and other energy losses, the temperature rise in the irradiated local region for a LT crystal ($\rho = 7.456\, g \cdot cm^{-3}$ [14] and c_p=0.424 $J \cdot g^{-1} \cdot K^{-1}$ [15]) could be over one hundred degrees. However, in reality, due to thermal conduction, the actual local temperature rise is only a few degrees in a bulk sample. According to Ref.[16], the last term $\vec{B}_T$, which is related to the geometry and dimension of the sample as well as its thermal conductivity, is the main factor to prevent the local temperature increase. A temperature rise of a few degrees Celsius was observed for bulk samples with a typical SEM current $I_b = 1\times10^{-9}$A[16]. For our case, smaller current was used but the scan rate was also slower, a temperature rise of 2 - 3 degrees Celsius in the irradiated local region is a reasonable estimate. This thermal effect can generate a pyroelectric potential U_{pyro} in the positive and negative domain regions,

$$U_{pyro} = \frac{\kappa \Delta T h}{\varepsilon_0 \varepsilon}, \qquad (2)$$

where κ is the pyroelectric coefficient of the sample. For LT crystal [15] κ = -17.6 × 10^{-5} C $K^{-1}m^{-2}$ and ε = 43.4. Assuming a small local temperature rise of ΔT~ 3 K, the generated potential will be U_{pyro}= -2.5V (2.5 V) for the positive (negative) domains. The pyroelectric potential difference between the positive and negative domains ΔU_{pyro} can be amounted to 5.0 V. This potential difference is large enough to produce a potential contrast on the surfaces of the positive and negative domains. This is because secondary electrons are low in energy (most are emitted with less than 10 eV), they are sensitive to the effects of surface potential and the electric field gradients near the sample surface. If U_{pyro}=2.5V for the negative domains, the secondary electrons with energies less 2.5 eV will not escape the sample, therefore, less electrons will arrive at the Everhart-Tornley detector. While for the positive domains, a bias of -2.5 V will act as a booster for the escape of secondary electrons, hence more electrons are likely to arrive at the detector. Experimentally, a higher yield of the secondary electrons can be observed on the surface of positive domains making them brighter.

LT is a good insulator with low electrical conductivity. When the cathode voltage $V_0 > V_2$, $\delta + \eta < 1$, electrons tend to accumulate on the irradiated surface producing

additional electric filed in the interior of the sample. In our experiment, the dwell time t_d of the probe is approximately 10^{-5}s and the frame interval t_i is 20s, therefore, the incident charge density per frame is estimated to be 2×10^{-5} C/cm^2. Because a significant fraction of the charge is scattered and emitted in the form of secondary electrons, the effective charge density for the surface build up is much lower. These accumulated charges may be dissipated through Maxwell relaxation process with a typical relaxation time $\tau_m = \varepsilon\varepsilon_0/\sigma$, where σ is the conductivity of the crystal. For a LT crystal, $\sigma < 10^{-11}\Omega^{-1}m^{-1}$ [17], so that $\tau_m > 30$s. Therefore, the accumulated charges will not be sufficiently relaxed within the dwell time t_d. Even after the frame interval time t_i (~ 20s) there are still remaining changes. This charge accumulation will cause the reduction of the effective acceleration potential V_a between the sample and the cathode to reduce the velocity of the injected electrons. It will continue accompanying the scan until the condition $\delta+\eta=1$ is reached, at which time the total charge on the surface of sample reached a dynamic equilibrium.

Before reaching the dynamic equilibrium, the surface charge is time-dependent, and follows a simple rule $q=q_0(1-e^{-t/\tau})$, where q_0 is the surface charge at the equilibrium, t is the observation time, and τ is the effective relaxation time which depends on the conductivity of the sample, the voltage and the current of the probe, the degree of vacuum in the chamber etc., thus, the surface potential V_s can be written as the following

$$V_s=(V_0-V_2)(1-e^{-t/\tau}) \qquad (3)$$

The average energy of an incident electron becomes

$$E_a = e(V_0 - V_s) = eV_2+e(V_0-V_2)e^{-t/\tau}. \qquad (4)$$

When the observation time $t >> \tau$, $E_a \rightarrow eV_2$. Equation (4) means that the probe energy is a function of the observation time t. At the inital stage of scan, $V_s=0$, $E_a=eV_0$. The resulting surface pyroelectric potential, according to Eqs.(1),(2),(3) and (4), may be estimated as

$$U_{pyro} = \frac{\kappa I_b t_d [V_2 + (V_0 - V_2)e^{-t/\tau} - L]}{\varepsilon_0 \varepsilon \pi a^2 \rho c}, \qquad (5)$$

where L is related with the terms of energy losses in Eq.(1). The pyroelectric potential on the LT sample surface will monotonously decrease with time during scan. The surface potential V_s of the positive and negative domains will differ by $2U_{pyro}$. When $t<<\tau$, V_s

$\approx U_{pyro}$, the dominant effect is the pyroelectric potential. On the other hand, when $t >> \tau$, $V_s >> U_{pyor}$, the potential difference between the positive and negative domains becomes insignificant. Experimentally, the pyroelectric domain contrast can only be unambiguously observed in the first frame of the scan. The image fades away rapidly with the increase of V_s.

III.2. *Piezoelectric imaging*

With the build up of the surface potential V_s, piezoelectric effect becomes more and more obvious, which leads to a topographic domain pattern. The field induced by the surface charge accumulation along the thickness direction is $E=V_s/l$, where l is the thickness of the sample, which induces an elastic strain $S=\Delta l/l = d_{33}E$ in the sample through the converse piezoelectric effect. For LT, $d_{33}=9.2\times10^{-12}$C N^{-1} [18], thus the surface displacement Δl is given by

$$\Delta l = d_{33}V_s = d_{33}(V_0-V_2)(1- e^{-t/\tau}), \qquad (6)$$

When $t>>\tau$, for $V_s\approx 3kV$, $\Delta l \approx \pm 0.03$ μm. For positive domains, the field $\boldsymbol{E}$ is parallel to the polarization $\boldsymbol{P}$ so that Δl is positive. While for the negative domains, $\boldsymbol{E}$ is anti-parallel to $\boldsymbol{P}$ so that Δl is negative. Because the bottom surface of the sample is only loosely bounded to the sample holder and free to deform, the surface displacement difference between the positive and negative domain on the top surface is 0.03 μm. Experimental results confirmed our analysis. The boundaries between positive and negative domains show sub-micron steps as shown in Fig.3. We also observed the boundary contrast at lower V_0 ($V_0 \leq$ 3 kV); the image was the same except shallower boundary steps as expected. This fact revealed that the equilibrium potential V_2 of the secondary electron emission in LT is lower than 3 kV.

The brightness of the topographic contrast actually observed depends on the physical location of Everlart-Thornely detector relative to the sample. Because the detector was located on one side of the sample, it has a non-perpendicular view. The secondary electrons emitted from the domain boundaries near the detector have a higher collective efficiency, therefore, these boundaries are brighter, and those emitted from the boundaries away from the detector have a relatively lower collective efficiency, therefore, appear

darker. In addition, the backscattered electrons mixed with secondary electrons may enhance the contrast.

IV. CONCLUSIONS

In conclusion, two different kinds of image contrast, i.e., domain contrast and domain boundary contrast, were observed in LT using SEM. They appeared in different stages during the scanning process by electron probe. At the initial frame, lower surface potential and higher probe energy produced contrast in antiparallel domains through pyroelectric effect. As charge accumulation began to occur on the polar surface of the sample due to the insulating nature of the sample and the imbalance of charge flow, i.e., $\delta+\eta \neq 1$, topographic images were produced by the piezoelectric effect in subsequent frames of scan. These two different kinds of contrast reveal that ferroelectric domains may be imaged by different physical mechanisms in which electrons play different roles.

ACKNOWLEDGMENT

This research was sponsored by the NSF and the ONR.

Reference

1. R. Le Bihan, Ferroelectrics **97**, 19(1989).
2. A. A. Sogr and I. B. Kopylova, Ferroelectrics **191**, 193(1997).
3. T. Ozaki, K. Fujii and S. Aoyagi, J. Appl. Phys. **80**, 1697(1996).
4. G. Rosenman, A. Skliar, Y. Lareah et al., J. Appl. Phys. **80**, 7166(1996).
5. D.V. Roshchupkin, M. Brunel, Scanning. Microsc. **7**, 543(1993).
6. A. Skliar et al., Ferroelectrics **191**, 187(1997).
7. T. Ozaki, K. Fujii and S. Aoyagi, J. Appl. Phys. **80**, 1697(1996).
8. S.N. Zhu and W. Cao, Phys. Rev. Lett. **79**, 2558(1997).
9. R. Le Bihan and M. Maussion, Rev. de Phys. Appl. **9**, 427(1974).
10. P. R. Thornton, *Scanning Electron Microscopy*, Chapman and Hall, London (1968).
11. S. N. Zhu el al., J. Appl. Phys. **77**, 5481(1995).
12. G. Rosenman et al., Phys. Rev. B, **54**, 6222(1996).
13. K. Kanaya and S. Ono, *Electron Beam Interactions with Solids*, SEM, O'Hare, Illinois (1984).
14. S.C.Abrahams and S.C. Bernstein, J. Phys. Chem. Solids **28**, 1685(1967).
15. H.P.Beerman, Infrared Phys. **15**, 225(1975).
16. J. I. Goldstein, *Scanning Electron Microscopy and X-Ray Microanalysis*, Plenum, New York, 1992.
17. G. I. Rozenman, J. S. Rez, Tu. L. Chepelev, N. B. Angert, Sov. Phys.-Tech. Phys. **26**, 234(1981).
18. T.Yamada, H.Iwasaki, N.Niizeki, Jpn. J. Appl. Phys, **8**., 1127(1969).

Figure captions:

Fig.1: Definition of electrical potential levels in the experimental set-up.

Fig.2: The sum of secondary- and backscattered-electron yield verses the effective acceleration voltage V_a of probe electron for an insulating crystal.

Fig.3: Domain contrast on the –c polar surface of a LT single crystal at the initial scanning frame. The triangular positive domains surrounded by the negative domains are brighter.

Fig.4: In subsequent frames, only boundary contrast can be observed on the polar surface of the LT sample.

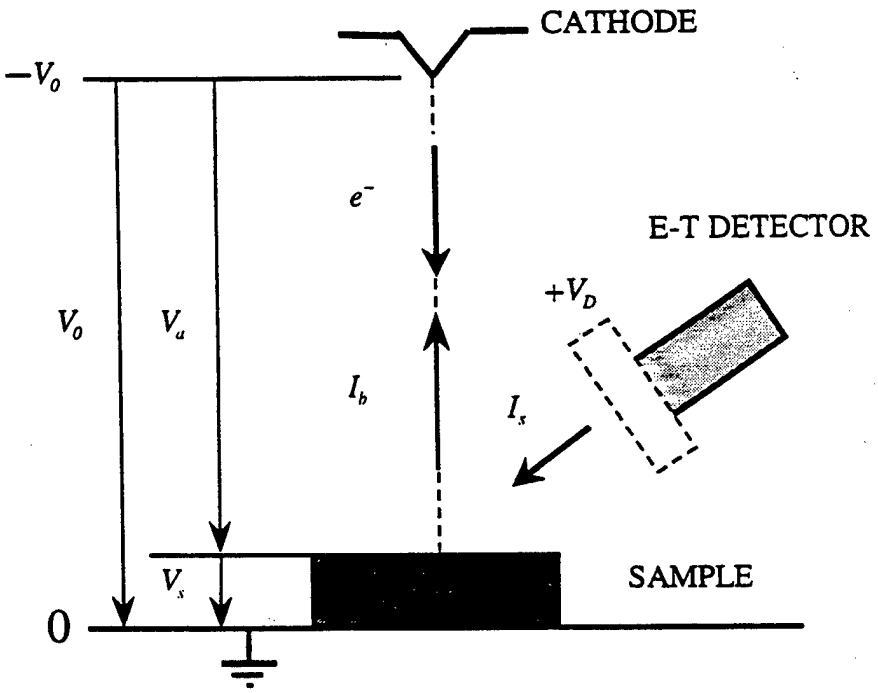

Fig. 1

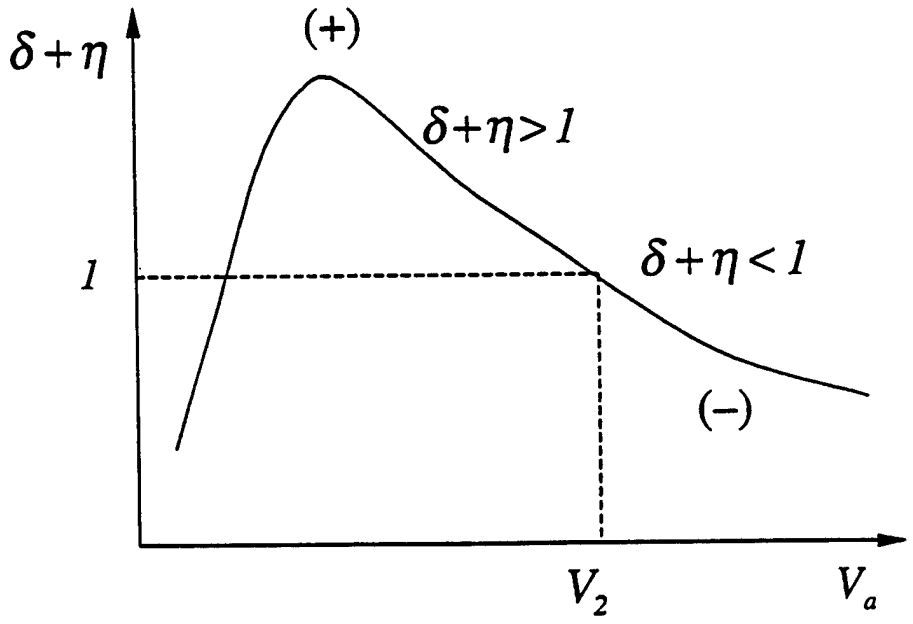

Fig. 2

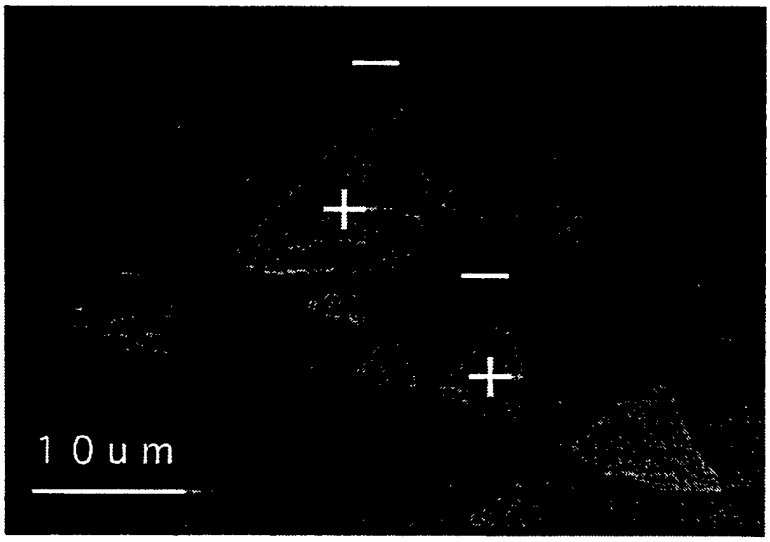

Fig. 3

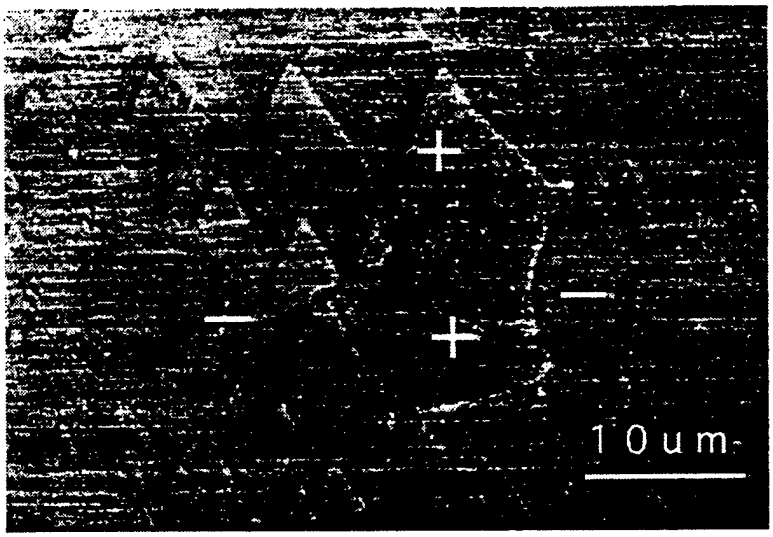

Fig. 4

APPENDIX 76

DETERMINATION OF DOMAIN AND DOMAIN WALL FORMATION AT FERROIC TRANSITIONS

D. M. HATCH* and W. CAO+
*Department of Physics and Astronomy, Brigham Young University, Provo, Utah 84602; +Materials Research Laboratory, The Pennsylvania State University, University Park, Pennsylvania 16802

Abstract: Through the example of the $Pm\bar{3}m$ - $I4/mmm$ structural phase transition in $LaAg_{1-x}In_x$ (x~0.2), a general procedure is given in this paper to model and predict the domain pair and domain wall formation using a group theoretical approach and a Landau-Ginzburg type continuum theory. The heterogeneous order parameter profile can then be calculated by using an initial value scan method based on the equilibrium conditions of the order parameter and the minimization of the total elastic energy. The dependence of the domain wall profile on different expansion coefficients of the free energy is demonstrated numerically in several examples.

Keywords: Group theory, Domains, Domain walls, Phase transitions, Ferroelastic, Landau-Ginzburg theory.

INTRODUCTION

Group theoretical methods provide the tools to obtain a great deal of information about phase transitions and the resulting domain structures. The symmetry change at a transition allows us to obtain the following: (1) the Landau-Ginzburg free energy, including gradient and secondary order-parameter (OP) invariants, (2) the number and the physical properties of possible homogeneous domains,

(3) the classification of equivalent domain and twin pairs and their symmetry, (4) the sets of non-linear equations which define the domain wall profiles in the heterogeneous structures, (5) the criteria for stability, and (6) the merging and splitting of domain walls.

In this paper we use the improper ferroelastic phase transition in a CsCl structure to illustrate the methodology of the symmetry approach. The transition is from a $Pm\bar{3}m$ to $I4/mmm$ structure[1] and is induced by an M_5^- mode softening in the pseudo- binary rare earth alloy $LaAg_{1-x}In_x$ (x~0.2). Structural details of the transition in CsCl are given in Ref. 1. We use the software program *ISOTROPY*[2] by Stokes and Hatch to quickly obtain some of the pertinent details of the invariants and domain twins.

THE LANDAU -GINZBURG FREE ENERGY

The symmetry of the $I4/mmm$ distorted phase with cell quadrupling initially gives two possible choices[2] for this symmetry change from $Pm\bar{3}m$. However, comparison with the observed displacements leads uniquely to the realization that the transition is induced by the soft mode of the M_5^- irreducible representation, corresponding to a six-component OP $\eta = (\eta_1,\eta_2,\eta_3,\eta_4,\eta_5,\eta_6)$, with the direction[1] of P_{10} = (a, a, 0, 0, a, -a). The Landau-Ginzburg free energy is constructed by forming polynomials which are invariant under the complete set of transformations of the higher symmetry group $Pm\bar{3}m$. The invariants obtained from *ISOTROPY* can be collected into two parts. The first, the Landau energy part, is composed of invariant polynomials of the primary and secondary OPs. These terms are indicated in the following manner $F_L(\eta)=F_{primary} + F_{secondary} + F_{coupled}$, with invariants up to sixth order in the primary and fourth order in secondary OPs, and terms coupling these two sets of parameters[1]. As far as the space group symmetry change is concerned, the first order vs second order nature of a transition does not play a prominent role, therefore, we take the expansion

for the primary OP only up to fourth order in this paper, which allows us to obtain some simple analytic and numerical solutions. The Ginzburg portion, F_G, is an invariant combination of spatial derivatives of the primary OP. The free

$$
\begin{aligned}
F_G = {} & b_1\left(\tfrac{5}{6}(\eta_{1,x})^2 - \tfrac{1}{\sqrt{3}}(\eta_{1,x})(\eta_{1,y}) + \tfrac{1}{2}(\eta_{1,y})^2 + \tfrac{1}{3}(\eta_{2,x})^2 + (\eta_{2,y})^2\right. \\
& \left. + \tfrac{5}{6}(\eta_{3,x})^2 + \tfrac{1}{\sqrt{3}}(\eta_{3,x})(\eta_{3,y}) + \tfrac{1}{2}(\eta_{3,y})^2\right) \\
& + b_2\left(-\tfrac{1}{2\sqrt{3}}(\eta_{1,x})^2 + (\eta_{1,x})(\eta_{1,y}) + \tfrac{1}{2\sqrt{3}}(\eta_{1,y})^2 + \tfrac{1}{\sqrt{3}}(\eta_{2,x})^2 - \tfrac{1}{\sqrt{3}}(\eta_{2,y})^2\right. \\
& \left. - \tfrac{1}{2\sqrt{3}}(\eta_{3,x})^2 - (\eta_{3,x})(\eta_{3,y}) + \tfrac{1}{2\sqrt{3}}(\eta_{3,y})^2\right) \\
& + b_3\left(\tfrac{1}{2}(\eta_{1,x})(\eta_{1,z}) + \tfrac{\sqrt{3}}{2}(\eta_{1,y})(\eta_{1,z}) - (\eta_{2,x})(\eta_{2,z})\right. \\
& \left. + \tfrac{1}{2}(\eta_{3,x})(\eta_{3,z}) - \tfrac{\sqrt{3}}{2}(\eta_{3,y})(\eta_{3,z})\right) + b_4\left((\eta_{1,z})^2 + (\eta_{2,z})^2 + (\eta_{3,z})^2\right)
\end{aligned}
\tag{1}
$$

energy form for this portion is given in Eq. (1). Euler's equations then lead to six coupled partial differential equations in η and three equations in stress as shown in Eq. (2),

$$
\begin{aligned}
\sum_m \frac{\partial}{\partial x_j}\left[\frac{\partial F}{\partial \eta_{i,j}}\right] - \frac{\partial F}{\partial \eta_i} &= 0, \quad (j=1,2,3;\ i=1,....6), \\
\sum_m \sigma_{nm,m} &= 0, \quad (m,n=1,2,3).
\end{aligned}
\tag{2}
$$

DOMAIN TWINS

The transition from $Pm\bar{3}m$ to $I4/mmm$ produces twelve homogeneous single domain states, labeled S_1, S_2 ...., S_{12}. The set of all elements of the parent group that do not change S_1 comprise the isotropy group $I4/mmm$ of the first domain. We label this group F_1, which is a subgroup with basis vectors (2,0,0), (0,2,0), (0,0,2) and origin (½, ½, 0) with respect the parent group. Those elements of the

parent group that transform S_1 into the particular domain S_i will form a left coset with respect to F_1 and the cosets can be used to write the parent group, denoted as G, in the form $G = F_1 + g_{2,1}F_1 + g_{3,1} + \ldots g_{12,1}F_1$, where $g_{i,1}$ is an element that transforms S_1 to domain S_i. The isotropy group of S_i is $g_{i,1} F_1 g_{i,1}^{-1} = F_i$.

A domain pair is of the form (S_i,S_j) and is made up of two domains which simultaneously exist in space without being combined and without interacting. Two domain pairs are said to be equivalent if there is some element g of the parent group G for which $g(S_i,S_j)=(gS_i,gS_j)=(S_k,S_l)$. This procedure allows all possible domain pairs for the $LaAg_{(1-x)}In_x$ transition to be grouped into four classes. The identity class (S_i,S_i), two antiphase classes exemplified by the domain pairs (S_1,S_{10}) and (S_1,S_4), and an orientation class exemplified by the pair (S_1,S_2). Equivalent domain pairs are indicated in Table I. We will not

Table I Equivalent domain pairs. k, m, n are positive integers; $k+3m$, $k+3n+1$, $k+3n+2$ are smaller than 12.

Domain Pair	Equivalent Pairs
(1,10)	(2,11), (3,12), (4,7), (5,8), (6,9)
(1,4)	(k, $k+3m$) without pairs in type (1,10)
(1,2)	(k, $k+3n+1$), (k, $k+3n+2$)

discuss here the case of the identity class. The study of domain walls will then be reduced to studying one representative from each of three classes.

A domain twin is defined as two semi-infinite single domain regions separated by a thin planar wall, with normal **n**, and containing the point **p**. Following Janovec's notation[3], this twin will be labeled $(S_j/\mathbf{n},\mathbf{p}/S_j)$. Its symmetry group (hereafter called its twin group) consists of four parts:

$$J_{ij} = \hat{F}_{ij} + t'_{ij}\hat{F}_{ij} + r_{ij}\hat{F}_{ij} + s'_{ij}\hat{F}_{ij}. \qquad (3)$$

Here, $\hat{F}_{ij}$ contains those elements that leave S_i, S_j, and **n** invariant; $\underline{t}'_{ij}\hat{F}_{ij}$ contains those elements that interchange S_i and S_j, and reverse **n**; $\underline{r}_{ij}\hat{F}_{ij}$ contains those elements that leave S_i and S_j invariant and reverse **n**; and $s'_{ij}\hat{F}_{ij}$ contains those elements that interchange S_i and S_j, and leave **n** invariant; while all of the above leave **p** invariant. Representative twin groups are indicated in Table II.

Table II Representative Twin Groups in LaAgIn
(in terms of the parent cubic setting)

Twin, Group, Basis, Origin	$\hat{F}_{ij}$	$\underline{t}'_{ij}\hat{F}_{ij}$	$s'_{ij}\hat{F}_{ij}$	$\underline{r}_{ij}\hat{F}_{ij}$
(1/(0,0,1),(0,0,0)/10) **P4/m2/m2/m** (1,-1,0),(-1,-1,0) (1/2,1/2,0)	**P4mm**	(C2b|0,0,0)	(E|-1,1,0)	(C2b|-1,1,0)
(1/(0,0,1),(0,0,0)/4) **P2/m2/m2/m** (0,2,0),(-1,0,0) (0,1/2,0)	**P2mm**	(C2y|0,0,0)	(E|-1,0,0)	(C2y|-1,0,0)
(2/(1,1,0),(0,0,0)/3) **C2mm** (0,0,2),(2,-2,0) (0,0,-1/2)	**C11m**	none	(C2a|0,0,1)	none
(2/(-1,1,0),(0,0,0)/3) **Cmm2** (-2,2,0),(2,2,0) (0,-1,0)	**C11m**	none	none	(C2a|0,0,1)

DOMAIN WALL SOLUTIONS

(I) The (1,10) antiphase boundary (APB) is formed between $P_1(\eta') = (\sqrt{2}\,a, 0,0,0,0,\sqrt{2}\,a)$ and $P_{10}(\eta') = (-\sqrt{2}\,a,0,0,0,0,-\sqrt{2}\,a)$. For convenience new OP components have been defined where $\eta'_i = \sqrt{2}(\eta_i + \eta_{i+1})$ or $\eta'_i = \sqrt{2}(\eta_i - \eta_{i+1})$ for *i* even or odd, respectively. The APB is formed by half a lattice constant

translation of the lower symmetry phase along the z direction. The single domain states serve as boundary conditions for heterogeneous solutions, and we consider the *inverse* boundary value problem based on the assumption that both the primary and the secondary OP depend only on the position coordinate z perpendicular to the domain wall, thus $\eta' = \eta'(z)$. The strains are subjected to

$$-(2D_4 - D_1)\frac{d^2\eta'}{dz^2} + k^+\eta' + (A_6^+ + A_{1,6}^+)\eta'^3 = 0. \qquad (4)$$

compatibility relations[4]. Assuming $\eta'_2 = \eta'_3 = \eta'_4 = \eta'_5 = 0$, the Euler equations reduce to two non-linear coupled second-order ordinary differential equations for $\eta'_1(z)$ and $\eta'_6(z)$. Both order parameter components satisfy the same equation, The solutions are $\eta'_1 = \eta'_6 = a\tanh(z/\xi_{APB})$, where $\xi_{APB} = [-2(2D_4 - D_1)/k^+]^{1/2}$ is the half width of the APB and k^+ is a renormalized second-order coefficient.

(II) The (1,4) antiphase boundary is formed between $P_1(\eta') = (\sqrt{2}\,a,0,0,0,0,$

$$-(2D_4 + D_1)\frac{d^2\eta'_1}{dx^2} + k_1^+\eta'_1 + A_1^+\eta'^3_1 + A_{1,6}^+\eta'_1\eta'^2_6 = 0,$$
$$-2D_3\frac{d^2\eta'_6}{dx^2} + k_6^+\eta'_6 + A_6^+\eta'^3_6 + A_{6,1}^+\eta'_6\eta'^2_1 = 0. \qquad (5)$$

$\sqrt{2}\,a)$ and $P_4(\eta') = (-\sqrt{2}\,a,0,0,0,0,\ \sqrt{2}\,a)$. This APB is formed by half a lattice constant translation of the lower symmetry phase along the x direction . We assume $\eta'_2 = \eta'_3 = \eta'_4 = \eta'_5 = 0$ and a domain wall perpendicular to x. The set of coupled nonlinear equations are given in Eq. (5). If we take no coupling, i.e., $A^+_{1,6} = 4A'_1 + 2A'_3 = 0$, we can find the following solution: $\eta'_1 = \sqrt{2}\,a\tanh(x/\xi_{APB})$, $\eta'_6 = \sqrt{2}\,a$, and $\xi_{APB} = [-2(2D_4 + D_1/k_1^+]^{1/2}$. In addition, the strain components e_2, e_3 are constant and $\sigma_{12} = \sigma_{23} = \sigma_{13} = \sigma_{11} = 0$.

(III) The (2,3) orientation twin boundary (OTB) is formed between $P_2(\eta') = (0,0,0,\sqrt{2}\,a,\ \sqrt{2}\,a,\ 0)$ and $P_3(\eta') = (0,\ \sqrt{2}\,a,\ \sqrt{2}\,a,\ 0,0,0)$. The domains 2 and 3 are related by a three-fold rotation along the [111] direction of the $Pm3m$ structure. Note that the (2,3) OTB is equivalent to the (1,2) OTB. In contrast to

the antiphase domains, orientation twin domains are distinguished by their ferroic properties, i.e., the two twin domains have *different* strains which can be detected optically or with x rays. The order-parameter profile representing the twin boundary has the following form: $\eta' = (0, \eta'_2, \eta'_3, \eta'_4, \eta'_5, 0)$ and contains the x = y plane. For the special case $Q_1 = \eta_2' = \eta_3'$, $\eta_4' = \eta_5' = Q_2$ we get the two coupled differential equations:

$$D^+ \frac{d^2 Q_1}{ds^2} + 2k_1^+ Q_1 + 4A_1^+ Q_1^3 + 2A_{1,2}^+ Q_1 Q_2^2 = 0,$$
$$D^- \frac{d^2 Q_2}{ds^2} + 2k_2^+ Q_2 + 4A_2^+ Q_2^3 + 2A_{1,2}^+ Q_2 Q_1^2 = 0. \qquad (6)$$

Assuming $A_{1,2}^+ = 0$ and by defining $\xi_{TB} = \sqrt{D^- / k_2^+}$, we get $Q_1 = 1/\sqrt{2}a\left[1 + \tanh(s/\xi_{TB})\right]$, and $Q_2 = 1/\sqrt{2}a[1 - \tanh(s/\xi_{TB})]$. The domain wall energy is $E = -\xi_{TB}(\frac{10}{3}k_2^+ a^2 + \frac{8}{3}A_1^+ a^4 + 2A_{1,2}^+ a^4)$. The strains e_r', e_3' are constant and $\sigma_{ss} = 0$, where r and s denote the [110] and [1,$\bar{1}$,0] directions, respectively.

(IV) Numerical Solutions: General solutions for both the antiphase and twin boundaries can be obtained by numerically solving the nonlinear coupled differential Eqs. (4), (5), and (6). From the mathematical formulations, the differential equations for the OTB (2,3) is the same as that for the AP twin boundary (1,4); therefore, we will analyze the equations for (1,4) using normalized variables and the normalized equations can also apply to the OTB case. The differential equations for a (1,4) AP boundary were given in Eq. (5). This set of coupled nonlinear differential equations can be solved by using the initial value scan method[5], and the solutions are expected to be similar to the solutions of Cao and Barsch[6].

The solutions for $A_{1,6}^+ = 0$ were given in our discussion after Eq. (5). For the more general case, $A_{1,6}^+ \neq 0$, we must solve Eq. (5) numerically. To simplify the mathematical problem, the following substitutions are introduced:

$$q_1 = \frac{\eta_1'}{\sqrt{2a}}, \quad q_2 = \frac{\eta_2'}{\sqrt{2a}}, \tag{7a,b}$$

$$\alpha = \sqrt{\frac{2D_3 k_1^+}{k_6^+(2D_4 + D_1)}}, \quad \beta_1 = \frac{A_{1,6}^+}{A_1^+ + A_{1,6}^+}, \quad \beta_2 = \frac{A_{1,6}^+}{A_6^+ + A_{1,6}^+}, \tag{7c,d,e}$$

$$x = \gamma\xi, \qquad \gamma = \sqrt{\frac{(2D_4 + D_1)D_3}{k_1^+ k_6^+}}. \tag{7f,g}$$

With these substitutions, Eqs. (6a,b) becomes dimension-less, i.e.,

$$\begin{aligned} \frac{1}{\alpha}\frac{d^2 q_1}{d\xi^2} &= q_1 + (1-\beta_1)q_1^3 + \beta_1 q_1 q_2^2, \\ \alpha\frac{d^2 q_1}{d\xi^2} &= q_1 + (1-\beta_2)q_2^3 + \beta_2 q_2 q_1, \end{aligned} \tag{8a,b}$$

and the boundary conditions become

$$\lim_{x\to\pm\infty} q_1 = \pm 1, \quad \lim_{x\to\pm\infty} q_2 = 1. \tag{9a,b}$$

From Eqs. (8) and (9), the function $q_1(\xi)$ should be an odd function, $q_2(\xi)$ should be an even function, and the following conditions hold:

$$q_1(0) = 0, \quad \frac{dq_2(0)}{d\xi}. \tag{10a,b}$$

One integral exists for Eqs. (8a,b), and is shown in Eq. (11),

$$\begin{aligned} &\beta_2{}^2\left(\frac{dq_1}{d\xi}\right)^2 + \alpha^2\beta_1\left(\frac{dq_2}{d\xi}\right)^2 + \alpha\beta_2(q_1^2 - 1) - \frac{\alpha}{2}\beta_2(1-\beta_1)(q_1^4 - 1) \\ &+\alpha\beta_1(q_2^2 - 1) - \frac{\alpha}{2}\beta_1(1-\beta_2)(q_2^4 - 1) - \alpha\beta_1\beta_2(q_1^2 q_2^2 - 1) = 0. \end{aligned} \tag{11}$$

Analyzing Eqs. (8a,b), one finds that stability requires $\beta_2 < 1$, which means that the coefficients A_6^+ and A_{16}^+ must have the same sign. The coefficient α should be on the order of one and positive. There are three independent parameters in Eqs. (8a,b), β_1, β_2 and α, which control the variation of the

order parameter across a domain wall or an AP boundary. Fig. 1 shows the influence of β_1 while the parameters α and β_2 are fixed. One can see that the anti-symmetric component q_1 of the order parameter changes the most while q_2, the symmetric component, shows little change. In Fig. 2, α and β_1 are fixed and β_2 changes from -0.4 to 0.2. For this case, only the symmetric component of the OP q_2 changes its amplitude while q_1 is practically un-changed. For both cases, only the amplitude of the OP varies but the thickness of the transition region is almost unchanged by the variation of β_1 and β_2. In Fig. 3, both β_1 and β_2 are fixed but changes in α go from -0.4 to 0.4. As we can see the wall thickness increases with α. The OP amplitude variation across a domain wall is determined by the nonlinear coefficients in the free energy expansion while the domain wall thickness is mainly controlled by the gradient coefficients.

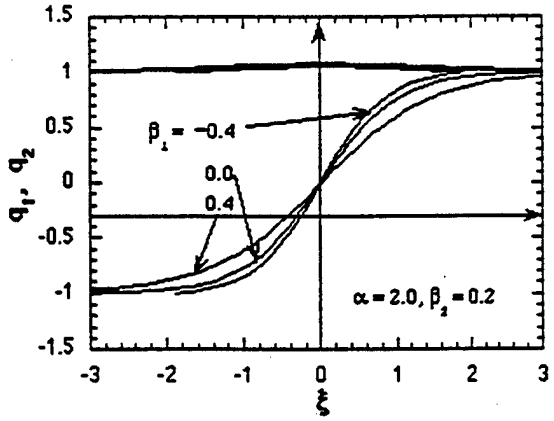

Figure 1 Numerical solutions for Eq. (8 a,b) with the coefficients $\alpha = 2.0$, $\beta_2 = 0.2$ and $\beta_1 = -0.4$, 0.0 and 0.4, respectively.

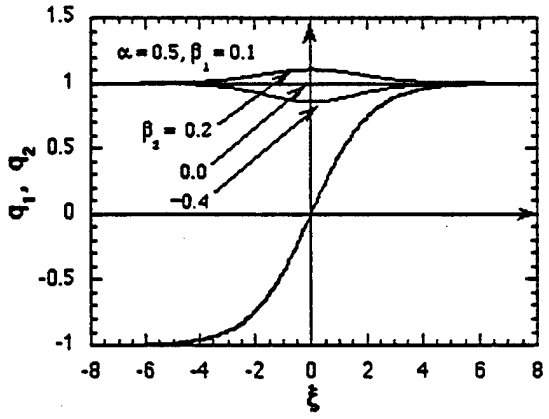

Figure 2 Numerical solutions for Eq. (8 a,b) with the coefficients $\alpha = 0.5$, $\beta_1 = 0.1$ and $\beta_2 = -0.4$, 0.0 and 0.2, respectively.

Stronger non-local coupling (large gradient coefficients) results in broader domain walls.

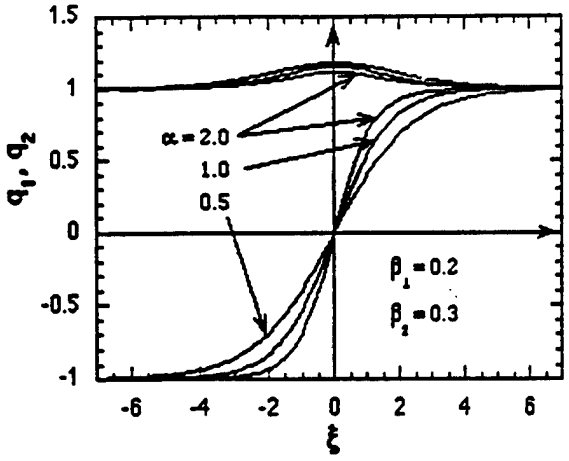

Figure 3: Numerical solutions for Eq. (8 a,b) with the coefficients $\alpha = 2.0$, $\beta_2 = 0.2$ and $\beta_1 = -0.4$, 0.0 and 0.4, respectively.

CONCLUSION

We have described a systematic method for studying the domains and also domain walls that occur in ferroic phase transitions. Use of the continually expanding ISOTROPY program gives information about primary and secondary order parameters and their invariants, gradient invariants, domain pairs and domain twins, as well as symmetry determined physical properties. Numerical solutions for the domain walls provided additional insight into the detailed OP variation in the spatial transition region and the influence of different physical parameters in the free energy.

REFERENCES

1. A. Saxena, G. R. Barsch, and D. M. Hatch, *Phase Trans.* **46**, 89 (1994); see the figures and references, therein.
2. H. T. Stokes and D. M. Hatch, *Isotropy Subgroups of the 230 Crystallographic Space Groups*, (World Scientific, Singapore, 1988).
3. V. Janovec, W. Schranz, H.Warhanek, and Z. Zikmund, *Ferroelectrics* **98**, 171 (1989).
4. E. A. H. Love, *A Treatise on the Mathematical Theory of Elasticity* (Dover, New York, 1944), pp.49, 131.
5. W. Cao, Ph.D. thesis, The Pennsylvania State University, (1987).
6. W. Cao and G. R. Barsch, *Phys. Rev. B* **41**, 4334 (1990).

APPENDIX 77

Ferroelectrics, 1998, Vols. 206–207, pp. 113–122
Reprints available directly from the publisher
Photocopying permitted by license only

THRESHOLD OF IRREVERSIBLE DOMAIN WALL MOTION IN SOFT PZT-PIEZOCERAMIC

VOLKMAR MUELLER and Q. M. ZHANG

Materials Research Laboratory, The Pennsylvania State University, University Park, PA 16802, USA

Received in final form 31 March 1997.

The nonlinear ac-field dependence of dielectric and piezoelectric coefficients in soft PZT piezoceramics is studied at $f = 100$ Hz. We demonstrate that two different thresholds for the onset of nonlinearity exist at $E_{c2} \approx 1$ V/cm and $E_{c1} \approx 100$ V/cm, respectively. At weak fields, the ac-field dependence of the effective dielectric coefficients obeys a scaling law $x = x_0 - A[(E-E_c)/E_c]^\varphi$ with the effective coefficient $\varphi = 1.5 \pm 0.1$. Above the large field threshold, both dielectric and piezoelectric coefficients exhibit a non-analytic scaling behavior. The nonlinearity is here anisotropic which is reflected by exponents $\varphi = 1.0 \pm 0.1$ and $\varphi = 1.2 \pm 0.1$ for fields parallel and perpendicular to the poling direction of the ceramic, respectively. The nonlinear domain wall response at fields well below the electrical depoling field is apparently dominated by the depinning of domain walls rather than by the anharmonicity of the potential energy of the wall.

Keywords: Nonlinearity; PZT; domain wall

INTRODUCTION

PZT-piezoceramics are widely used in technically applications such as piezoelectric actuators, resonators and motors. In these applications, the material is usually driven in high electric fields resulting in a substantial nonlinearity in the piezoelectric and dielectric behavior. [1] Nevertheless, up to date little understanding was developed about the mechanisms causing the nonlinear field dependence of the piezoelectric and dielectric properties of PZT.

It is well known that the motion of domain walls driven by external electric or elastic fields has an important influence on the linear dielectric and piezoelectric response of the piezoceramic (see for example reference [2–5]).

A large amount of experimental work was done to separate this extrinsic domain wall contribution to the material coefficients from the intrinsic properties of a (hypothetic) single domain PZT-single crystal. [6–11] In donar doped (soft) PZT, where the mobility of the walls is exceptionally high, the domain wall contribution to the permittivity at room temperature was shown to be approximately 60%. [6] The data available up to now indicate that, depending on the amplitude of the driving ac-field, at least two different types of domain wall contributions exist in PZT.

First, domain walls were shown to contribute already at low ac fields $20\,\mathrm{mV/cm} < E < 40\,\mathrm{V/cm}$ both to the permittivity ε_{33} and the piezomodule d_{33} and no ac-field dependence could be detected within the measuring accuracy in this ac-field range. [12] It is assumed that weak ac-fields excite oscillations of domain walls which are pinned at the grain boundary and at randomly distributed defects within the grain. The amplitude of these oscillations is thereby much smaller than the lattice constant. This type of domain contribution is referred to as reversible domain wall motion because no field hysteresis of the polarization P could be observed at weak fields.

Results of several authors indicate, on the other hand, that a threshold for the onset of nonlinearity exists in soft PZT at $E_c \approx 100\,\mathrm{V/cm}$. [7, 12, 13] Since the intrinsic nonlinearity in PZT is believed to be negligible at these fields, it was suggested that an additional type of domain wall movement sets in at E_c. Above threshold, the $P(E)$ dependence is hysteretic and can be described by the Rayleigh law originally discovered in ferromagnetic systems. [14] Therefore, the additional domain wall contribution at $E > E_c$ is referred to as irreversible domain wall motion. The threshold field E_c is usually defined to be the smallest value of the electric field for which a field dependence of the corresponding quantity can be detected. Clearly, this procedure depends on the accuracy of the measurement and can give only an upper limit for E_c.

In addition to the threshold behavior due to the onset of irreversible domain wall motion, other sources of nonlinearity related to the domain wall interaction, the electrical and mechanical boundary conditions and the nucleation and coalescence of domains may be of importance at higher field strengths. These effects were considered in a formal phenomenological approach by treating the motion of the wall in an anharmonic potential. [7]

In this paper, we have studied the ac-field dependence of the dielectric and electromechanical properties of a soft PZT-piezoceramic. We compare data obtained in fields parallel and perpendicular to the poling direction of the ceramic, respectively. Special attention was paid to the range of low ac-fields in order to get information about the threshold for the onset of irreversible domain wall motion in this material.

Experimental

All samples were cut from a commercial available PZT-ceramic (Motorola 3203HD) which had been poled for 1 minute at a temperature $T = 373$ K. The poling field was thereby $E = 20$ kV/cm. The measurements parallel to the poling direction were performed at thin plates (typical dimensions $3 \times 3 \times 1\,\text{mm}^3$), whereas perpendicular to this direction rectangular parallelepipeds (typical dimensions $5 \times 3 \times 3\,\text{mm}^3$) were chosen. Gold electrodes were sputtered onto the major faces.

The longitudinal and shear strain S_3 and S_5, respectively, were measured using a glass fibre sensor (MTI 2000). The sample was glued with its bottom electrode on a stage and a mirror was mounted on to the top electrode from which the motion of the top surface, originated from either S_3 or S_5, can be sensed. The sinusoidal measuring voltage ($f = 100$ Hz) was generated by a function generator (Stanford Research Systems DS 345) and a high voltage amplifier (TREK 610 C). The output signal of the glass fiber sensor was fed both into a digital oscilloscop displaying the strain-field dependence and a lock-in amplifier (Stanford Research Systems DSR-830) analyzing its first harmonic component $S_j^{(1.h)}$ from which we determined the effective piezocoefficient $d_{ij} = S_j^{(1.h)}/E_i$. A Sawyer-Tower circuit was used to measure simultaneously the polarization of the sample which was analyzed in its first harmonic $P_i^{(1.h)}$ by another lock-in amplifier to obtain the effective dielectric coefficients $\varepsilon_{ii} = P_i^{(1.h)}/E_i$.

In order to estimate the influence of dielectric heating and field induced changes of the domain structure in large fields, we compared the results obtained in the continuous wave mode and tone burst mode where 5 periods of the ac-voltage are followed by a 3 seconds zero voltage dwelling time. The measurements were restricted to the field range where the results do not depend on the mode chosen in the experiment. At weak fields, only the permittivity was measured using a General Radio 1616 precision capacitance bridge with an DSR-830 lock-in amplifier as a null indicator.

RESULTS AND DISCUSSION

All effective dielectric and piezoelectric coefficients show qualitatively the same ac-field dependence (Figs. 1a,b). The nonlinear contribution to these coefficients increases considerably with increasing amplitude E of the ac-field so that at a field $E \approx 3$ kV/cm the coefficients are about two times of the corresponding small signal value. By adjusting the weak signal coefficient,

the large field data can be scaled in such a way that, in a double logarithmic scale, they can be well approximated by straight lines. This indicates that the ac-field dependence of the coefficients obeys in large fields a simple power law. However, deviations from the power law appear at $E < 100$ V/cm and the ac-field dependence is much smaller in this field range. This supports the hypothesis suggested previously [7, 12] that the onset of irreversible domain wall motion in electric fields above a threshold E_c causes the significant nonlinearity of PZT. In order to test this scenario, the data were analyzed with the scaling relation

$$x = x_0 + A\left[(E - E_c)/E_c\right]^{\phi} \tag{1}$$

where x stands for ε_{11}, ε_{33}, d_{15} and d_{33}, respectively, and the threshold field E_c, the weak field coefficient x_0, the prefactor A and the exponent ϕ are used as free fitting parameters.

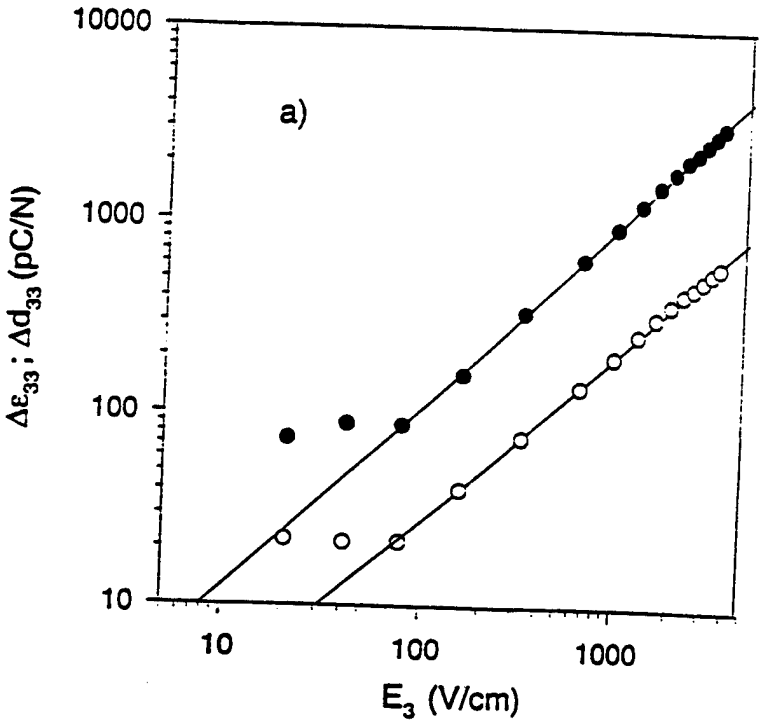

FIGURE 1 AC-field dependence of the field dependent part of the effective coefficients a) ε_{33}, d_{33}; b) ε_{11}, d_{15}. Full symbols represent dielectric data, open symbols piezoelectric data. The straight lines illustrate the power law at fields $E > 100$ V/cm.

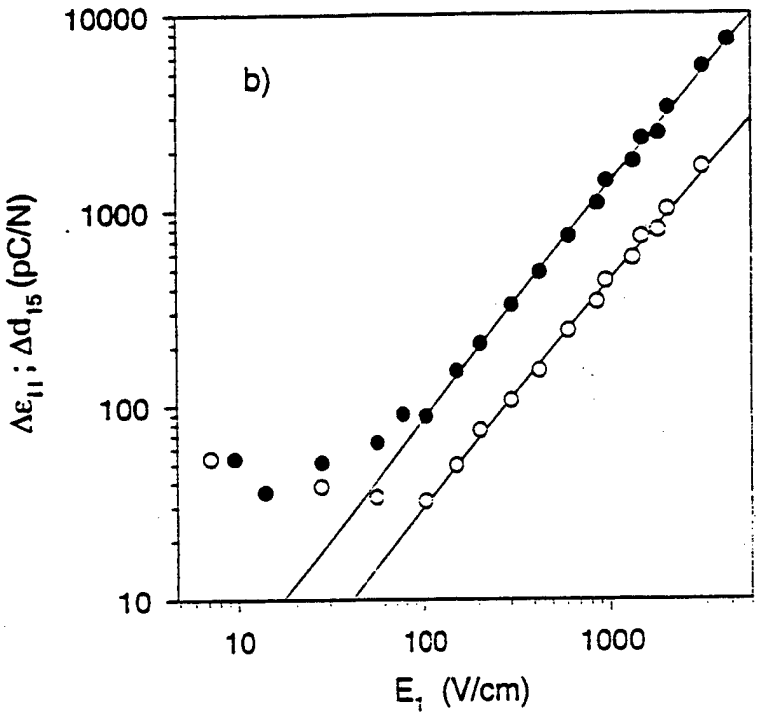

FIGURE 1 (Continued).

The data above threshold can be fitted quite well by Eq. (1). For an accurate determination of E_c, however. the parameter x_0 would have to be fixed. This requires the precise knowledge of the weak signal coefficient which we find to have itself a weak but distinctive ac-field dependence which we will discuss later. For this reason. we can give here only a rough estimation $E_c = 100 \pm 50$ V/cm. For a given direction of the field, the fit parameters φ and E_c obtained on piezoelectric and dielectric data do not show significant difference. Since the piezoelectric response can only be from the non-180° wall motion. the adta suggest that it is predominantly the non-180° walls which are depinned and contribute to the nonlinear response above E_c. On the other hand. the effective exponent φ depends on the direction of the ac-field which indicates a significant anisotropy of the nonlinearity of the ceramic. We determined exponents $\varphi = 1.0 \pm 0.1$ for fields parallel and $\varphi = 1.2 \pm 0.1$ for fields perpendicular to the poling direction.

Now we discuss the observed nonlinearity of PZT piezoceramics in terms of the motion of domain walls driven by the external electric field. At low frequencies where the inertia of the wall can be neglected. this motion is

given by [3, 5]

$$\frac{\partial U}{\partial \Delta x} + F_F = -\frac{\partial W_E}{\partial \Delta x} \tag{2}$$

Here, Δx is the wall displacement from the equilibrium position due to the driving force given by the electric energy W_E of the wall in the external electric field. The energy dissipation of the moving walls is usually treated by introducing a friction force $F_F \propto \Delta \dot{x}$, depending linearly on the wall velocity. Finally, the restoring force F_r is determined by the potential energy $U(\Delta x)$ of the wall which may be strongly anharmonic. In this case, F_r acting on a wall would depend nonlinearly on the displacement Δx from its equilibrium position. Nevertheless, any nonlinearity attributed to an anharmonic potential $U(\Delta x)$ has to meet the symmetry conditions which imply that the Taylor expansion of a coefficient depending on a field E_1 perpendicular to the poling direction can contain only even order terms of E_1. [7] The exponent $\varepsilon = 1.2 \pm 0.1$ determined from the ac-field dependence of d_{15} and ε_{11}, respectively, is obviously inconsistent with this symmetry restriction. It should be noted that this non-analytic nonlinearity can be found also in other soft PZT materials and the results of a more comprehensive study will be published elsewhere. [15]

In small fields $E < 100$ V/cm, the resolution of the strain measurement was insufficient to provide an accurate analysis of the ac-field dependence of the piezoelectric coefficients so that we present here only dielectric weak field data. Though much weaker than in large fields, the ac-field dependence of the dielectric coefficients shown in Figure 2 is apparently more intricate than in large fields and depend moreover on the particular sample under investigation. A closer examination shows, however, that the sample properties have changed during the measurement by the measuring field itself. That is, the value $\chi(E_0)$ of the susceptibility, determined for sufficiently small fields $E_0 \leq 0.3$ V/cm for which no ac-field dependence can be detected, changes during the measurement and depends on the value of the measuring field E_m before (see Fig. 2). We interprete this behavior as a deaging phenomenon due to the measuring field. This deaging effect has in weak fields the same order of magnitude as the reversible ac-field dependence which we separate by considering the difference

$$\Delta\chi = \chi(E_m) - \chi(E_0). \tag{3}$$

The resulting values $\Delta\chi(E_m)$ are independent of the particular aging state of the sample and can be fitted according to Eq. (1) in the same way as the corresponding data in large fields. In this manner, we found for both

directions of the external field the effective exponent $\varphi = 1.5 \pm 0.1$ (Fig. 3). As in the large field region, this ac-field dependence can not be attributed to a simple Taylor-expansion of the dielectric coefficient. On the other hand, the threshold in weak fields can be determined much more precisely because the field independent part χ_{lin} has not to be taken into account as an additional fitting parameter. Therefore, the data prove unambiguously the existence of a non-zero threshold $E_{c2} = 0.6 \pm 0.2$ V/cm for the onset of nonlinearity in the ceramic at weak fields. Since we could not obtain sufficiently accurate piezoelectric data in weak fields, it is not clear whether the threshold at E_{c2} is connected with the onset of 180° wall motion or with another kind of non-180° wall motion.

One approach to introduce a nonlinearity into the model of moving domain walls, which is compatible with the experimental results, is to modify the assumption of a linear friction force-velocity dependence $F_F(\dot{x})$.

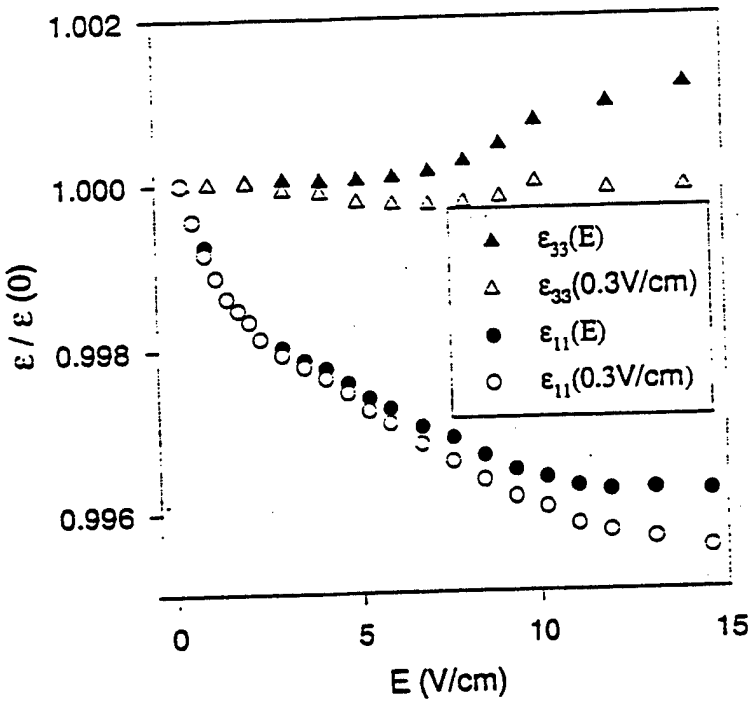

FIGURE 2 AC-field dependence of the dielectric coefficients in weak fields (full symbols). The data are normalized to the value ε(0) measured initially at the AC-field $E_0 = 0.3$ V cm. Open symbols represent data measured at $E = E_0$ immediately after the measurement at the particular measuring field $E_m > E_0$ was completed.

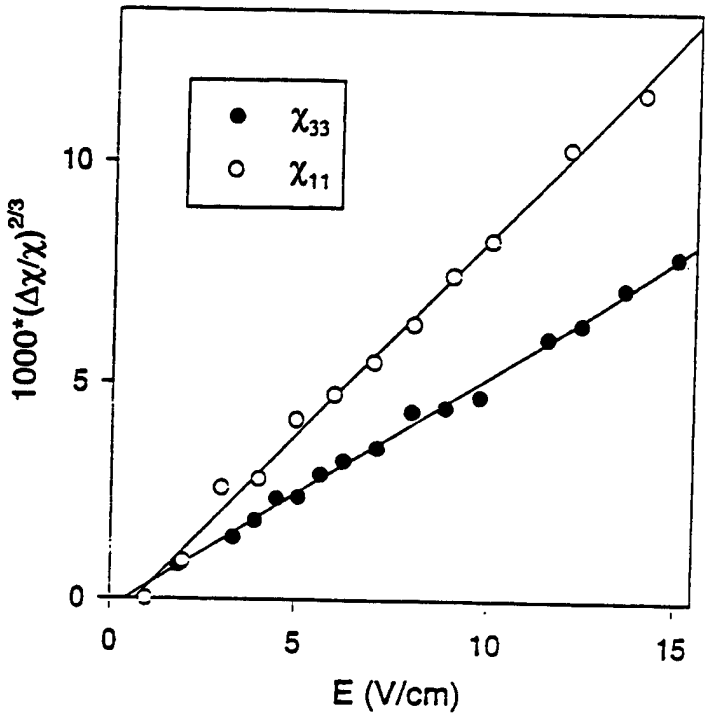

FIGURE 3 AC-field dependence of the reversible excess part $(\Delta\chi\ \chi)^{1.5}$ of the susceptibility close above weak field threshold. The exponent $\beta = 3.2$ was obtained from a least square fit of the experimental data which is represented by the straight lines.

We note that theoretical models treating the depinning transition of elastic interfaces as a dynamical critical phenomenon predict a scaling behavior similar to Eq. (1) between force and velocity above the onset of interface motion. [16] The introduction of a nonlinear friction force changes Eq. (3) into a nonlinear differential equation

$$\Delta\dot{x} = \beta\left[-\left(\frac{\partial W_E}{\partial\Delta x} + \frac{\partial U}{\partial\Delta x}\right) - F_c\right]^{\zeta}, \qquad (4)$$

where β is a friction coefficient and F_c the critical depinning force. The critical exponent ζ depends on the spatial dimensionality d and no result is available up to now for $d=3$. It is believed that the exponent for $d=3$ is between 1 and the mean-field exponent 3/2. [17]

We are aware that the values for threshold field and effective exponent obtained in a technical piezoceramic represent the average over all grains. 180°– and several types of non-180° domain walls with different

orientations to the external field. In addition, our experiments may not probe the critical region of a probable depinning transition in the sense of the theory mentioned above. As more it is surprising, that the exponents determined in this study seem to be consistent with the theoretical expectations. Moreover, an exponent $\varphi = 1.45 \pm 0.03$ was found recently for (non-ferroelastic) 180° domain walls in the ferroelectric lock-in phase of a purified incommensurate single crystals. [18] Clearly, more experimental work especially on single crystals is necessary to obtain further information about the depinning transition of ferroelectric non-180° walls.

Another related issue is the nature of the restoring force which cannot be ignored in Eq. (4) since this would lead to a nonlinear conductivity. It should be pointed out that only a small amount $\Delta P \leq 0.1\, P_0$ of the spontaneous polarization P_0 is switched in our experiments. Apparently, the mean displacement of the walls is considerably smaller than the mean wall-wall distance provided that the majority of the walls are displaced by the field and contribute to ΔP. For small displacements Δx, it is reasonable to assume that the wall moves in a quasiharmonic potential and the restoring force depends approximately linearly on Δx. On the other hand, the motion of the interface close above the depinning threshold is jerky and the elasticity of the wall itself may also contribute to the restoring force.

To conclude, evidence for the onset of nonlinearity in soft PZT piezoceramics at two threshold fields E_{c1} and E_{c2} was obtained by analyzing the nonlinear ac-field dependence of their dielectric and piezoelectric coefficients. The result suggests that dynamical critical phenomena connected with the onset of collective interface motion above a threshold field E_c determine the nonlinear response of the piezoceramics. The nonlinearity of ferroelectrics in the field range of so called "Raleigh loops" [14] appears therefore to be attributed to the dynamics of domain walls moving in a medium with randomly distributed pinning centers rather than by the anharmonicity of the potential energy of the wall.

The authors are grateful to the Motorola Ceramics Products Division for providing ceramic material for this study and acknowledge financial support from the office of Naval Research.

References

[1] Cross, L. E. "Ferroelectric Ceramics: Tailoring Properties for Specific Applications" in "Ferroelectric Ceramics", edited by N. Setter and E. L. Colla (Birkhaeuser Verlag, Basel 1993).

[2] Jaffe, B., Cook, J. and Jaffe, H. "*Piezoelectric Ceramics*", (Academic Press, London 1971).

[3] Arlt, G. and Pertsev, N. A. (1991). *J. Appl. Phys.*, 70, 2283.
[4] Smits, J. (1976). *IEEE Trans. Son and Ultrason.*, SU-23, 168.
[5] Fousek, J. and Brezina, B. (1964). *J. Phys. Soc. Jpn.*, 19, 830.
[6] Zhang, Q. M., Wang, H., Kim, N. and Cross, L. E. (1994). *J. Appl. Phys.*, 75, 454.
[7] Li, S., Cao, W. and Cross, L. E. (1991). *J. Appl. Phys.*, 69, 7219.
[8] Zhang, X. L., Chen, Z. X., Cross, L. E. and Schulze, W. A. (1983). *J. Mater. Sci.*, 18, 968.
[9] Kersten, O. and Schmidt, G. (1986). *Ferroelectrics*, 67, 191.
[10] Boettger, U. and Arlt, G. (1992). *Ferroelectrics*, 127, 95.
[11] Kleemann, W. and Schremmer, H. (1989). *Phys. Rev. B*, 40, 7428.
[12] Zhang, Q. M., Pan, W. Y., Jang, S. J. and Cross, L. E. (1988). *J. Appl. Phys.*, 64, 6445.
[13] Saito, Y. (1995). *Jpn. J. Appl. Phys.*, 34, 5313.
[14] Damjanovic, D. and Demartin, M. (1996). *J. Phys. D: Appl. Phys.*, 29, 2057.
[15] Mueller, V. and Zhang, Q. M. to be published.
[16] Fisher, D. S. (1985). *Physical Review B*, 31, 1396.
[17] Littlewood, P. B. in "Charge Density Waves in Solids", edited by L. P. Gorkov and G. Gruner (Elsevier, Amsterdam 1989).
[18] Hauke, T., Mueller, V., Beige, H. and Fousek, J. (1996). *J. Appl. Phys.*, 79, 7958.

APPENDIX 78

Jpn. J. Appl. Phys. Vol. 37 (1998) pp. 602–605
Part 1, No. 2, February 1998

A Fractal Analysis on Domain Related Electric Field Induced Acoustic Emission in Ferroelectric Ceramics

Hideaki ABURATANI, John P. WITHAM and Kenji UCHINO

International Center for Actuators and Transducers (ICAT), Intercollege Materials Research Laboratory, The Pennsylvania State University, University Park, PA 16802, USA

(Received May 30, 1997; accepted for publication November 21, 1997)

The electric field induced acoustic emission (AE) in ferroelectric ceramics under bipolar electric fields has been studied. From the AE event rate and the AE signal amplitude distribution, it is assumed that there are two origins of the field induced AE in the ferroelectric ceramics: domain reorientation related deformation and piezoelectric deformation without domain reorientation. The fractal dimension (m) in the field induced AE signal amplitude distribution of the ferroelectric ceramic is found to be $m = 1$ for the domain reorientation related deformation. The fractal dimension of $m = 2.8$ is observed for the piezoelectric deformation unrelated to domain reorientation after domain reorientation is completed. It is shown that the fractal dimension of the AE caused by the domain reorientation related deformation is lower than that of the AE generated by the piezoelectric deformation unrelated to domain reorientation at high electric fields.

KEYWORDS: acoustic emission (AE), domain, ferroelectrics, fractal dimension, PLZT, PMN-PT, PZT

1. Introduction

Acoustic emission (AE) method is a non-destructive technique used to detect pulses of released elastic strain energy caused by deformation, crack growth and phase change in a solid.[1] The AE method has also been used to investigate fundamental domain motions in ferromagnetic and ferroelectric materials,[2,3] as well as mechanical and fatigue properties of materials.[4] In ferroelectric and piezoelectric materials, the AE method has been used to determine phase change,[5–7] to detect domain reorientation[8–10] and to monitor crack propagation.[11,12] However, recent research has revealed a significant problem in most of the previous field induced AE studies in the ferroelectrics. Acoustic waves were generated by a sample's mechanical vibration, which was caused by an electrical coupling between the power supply feedback and the piezoelectricity of sample.[13] The acoustic wave generated by the vibration was large enough to conceal the true AE signal and was constantly observed at high signal amplification of the AE measurement system. It was clarified that the fundamental Kaiser effect in terms of the electric field took place in ferroelectric ceramics by eliminating the sample vibrations.[14] The field induced AE will not be present after poling as long as the applied field is maintained lower than that of the poling field (i.e., Kaiser effect). Therefore, the previous reported ferroelectric domain contributions in the field induced AE generation should be reexamined through the new AE measurement technique.

This paper deals with the electric field induced AE generations in the ferroelectric and related ceramics under bipolar fields. A fractal analysis of the AE signal amplitude distribution, which is used in the AE method to determine the damage of materials, was applied.[15] The effect of the existence of the domain structure to the AE generation in ferroelectric lead zirconate titanate $Pb(Zr_x, Ti_{1-x})O_3$ (PZT) ceramics has been discussed with comparisons to the electrostrictive lead magnesium niobate–lead titanate solid solution $x Pb(Mg_{1/3}Nb_{2/3})O_3$–$(1-x)PbTiO_3$ (xPMN–$(1-x)$PT) and soft piezoelectric lead lanthanum zirconate titanate $Pb_{1-3x/2}La_x(Zr_{1-y}, Ti_y)O_3$ (PLZT: $(x/y/1-y)$) ceramics.

2. Experimental Setup

Figure 1 shows the measurement system. The electric field induced AE and displacement were observed simultaneously. The AE signal was detected by an AE sensor (NF Corp., AE-904E) with its resonant frequency of 450 kHz. The AE signal was amplified by 40 dB through a pre-amplifier (NF Corp., AE-9913) and again up to 60 dB with a main amplifier (NF Corp., AE-922). The amplified signal was counted after passing through a high-pass filter (100 kHz) and a discriminator. Disc specimens of commercialized ferroelectric PZT ceramic (Morgan Matroc, PZT-5A) as well as, electrostrictive ceramics 0.9 PMN–0.1PT and soft piezoelectric PLZT (9/65/35), with 12.7 mm in diameter and 0.4 mm in thickness were employed for this study. Gold electrodes were formed on both surfaces by sputtering. The AE sensor was attached to the sample through brass-foil with 0.025 mm in thickness, and silicone grease was used as a couplant to make a close adhesion. An external resistor R ($R = 20\,M\Omega$) and a capacitor C ($C = 0.01\,\mu F$) were installed to the power supply in order to eliminate the electrical coupling by increasing the time constant τ ($=R \times C$) of the voltage application system (i.e., to suppress the high frequency feedback components). It should be noted that the external resistor and capacitor did not cause any electrical interference to the AE measurement system and also the intrinsic AE generations in the ceramics as long as the induced displacement was maintained and the field was applied at much lower frequency than the time constant τ. The threshold level and amplification of the AE signal were changed from 400 mV at 100 dB to 400 mV at 60 dB. The samples were driven under the bipolar field at various electric field levels. The driving frequency of 0.0015 Hz was employed to obtain the saturation of the field induced displacement and AE to avoid the effect of the supplied current limited by the external resistor and capacitor.

3. Results and Discussions

3.1 The electric field induced AE

Figures 2(a) and 2(b) show the AE event count rate and the induced displacement of the ferroelectric PZT ceramics as a function of applied field at 0.0015 Hz with field levels

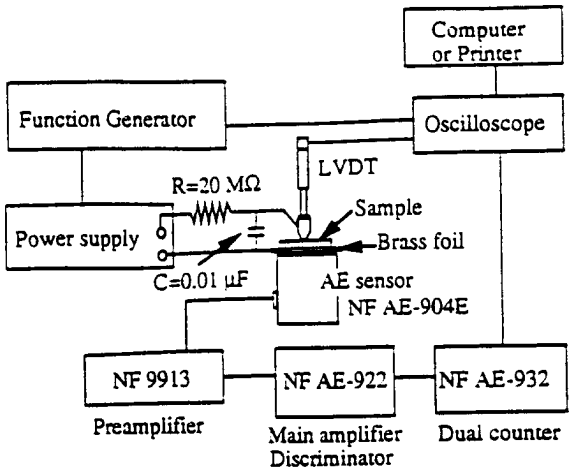

Fig. 1. Measurement system.

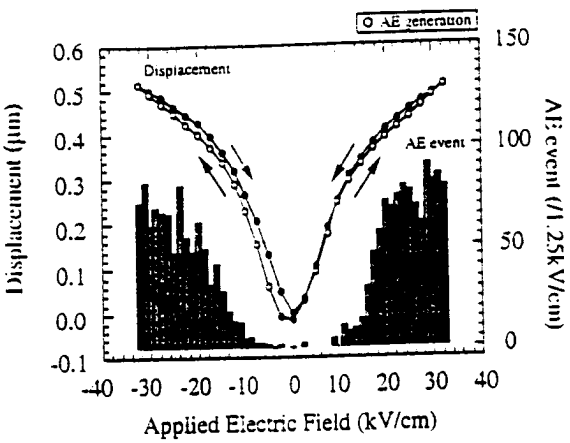

Fig. 3. AE event count and the induced displacement as a function of applied field electrostrictive 0.9 PMN–0.1 PT.

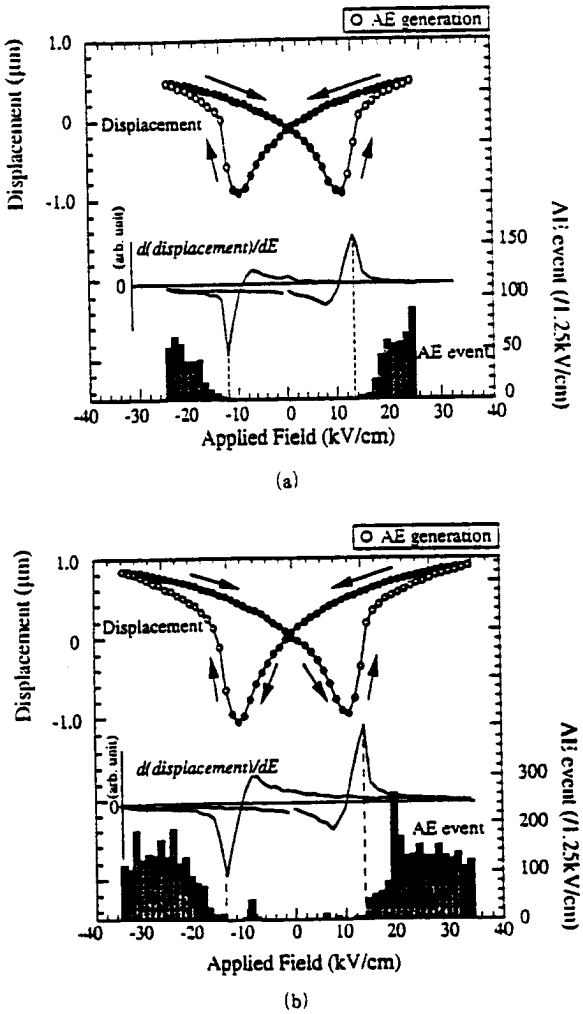

Fig. 2. AE event count and the induced displacement as a function of applied field of ferroelectric PZT. (a) $E = \pm 25$ kV/cm and (b) $E = \pm 35$ kV/cm.

of ± 25 kV/cm and ± 35 kV/cm, respectively. The AE measurement conditions were set to be at 100 dB with a threshold level of 400 mV. A butterfly shape induced displacement was obtained. For both measurements, the AE was not observed at the coercive field at which the induced displacement took a minimum. The critical electric field, where the AE started to be generated, was slightly higher than the coercive field. This critical electric field corresponded to the point of inflection at which the second derivative of the displacement with respect to the field, $d^2(displacement)/dE^2$, changes the sign. In Figs. 2(a) and 2(b), change of the first derivative of the displacement with respect to the field $d(displacement)/dE$ is shown for the point of inflection, and the critical electric field corresponds to the point where $|d(displacement)/dE|$ is the maximum. Since the displacement induction rate started to decrease in spite of the field simply increasing and the AE was present above this field, these results might indicate that a damping process for the sample deformation existed above this field and the AE was generated through that process. The AE event count rate increased with the applied field when a field of $E = \pm 25$ kV/cm was applied to the sample. For a field of $E = \pm 35$ kV/cm, the maximum of AE event count rate was not observed at the maximum applied field. The maximum event rate occurred around 27.5 kV/cm. Considering that internal stress increases with the applied field in ferroelectrics, if this observed AE was caused only by the internal stress, the AE event count rate should have increased with the applied field. Thus, this decrease in the AE event rate might suggest that the internal stress could be the origin of the AE, but not only one source. Since the induced displacement in the ferroelectric ceramics consists of the domain reorientation related deformation and piezoelectric deformation without the domain reorientation, it was assumed that the field induced AE in the PZT ceramics was generated first through domain reorientation related deformation and, after domain reorientation was completed, the piezoelectric deformation unrelated to domain reorientation which was accompanied with induced stress was expected to be the origin of the AE. The decrease in the AE event might indicate the completion of the domain reorientation related deformation.

Figure 3 shows the induced displacement and AE event count rate of the electrostrictive PMN–PT ceramics. A quadratic induced displacement which showed much less hysteresis than that of ferroelectric PZT ceramics was observed. The AE event count rate increased with the applied field. Because of the absence of the domain in PMN–PT, the induced

displacement did not caused by the domain reorientation, but domain reorientation unrelated electrostrictive deformation. It was assumed that the origin of the AE was the internal stress caused by the electrostrictive deformation unrelated to domain reorientation, resulting in the increased AE event rate with applied electric field.

Figure 4 shows the AE event count rate and the induced displacement of the soft piezoelectric PLZT (9/65/35) ceramics, which showed an intermediate displacement change between the ferroelectric PZT and electrostrictive PMN–PT ceramics. The AE generation started above the coercive field which was determined from the induced displacement. A peak of the AE event rate was observed around 10 kV/cm, and the AE event rate increased with the applied field when a field higher than 10 kV/cm was applied. It was assumed that the peak of the AE event rate was due to the domain reorientation related deformation, and after the domain reorientation was completed, the AE was caused by the piezoelectric deformation unrelated to domain reorientation. These results suggests that both the domain reorientation related and unrelated deformations were the origins of AE in the PLZT (9/65/35) ceramics.

3.2 *The fractal dimension of the electric field induced AE*

When the AE event rate $f(x)$ is the minus m-th power of x, where x is the AE signal amplitude,

$$f(x) = cx^{-m} \quad (c : \text{constant}) \tag{1}$$

the number of m is defined as a fractal dimension.[14] The fractal dimension m is used to estimate the damage in the materials. In general, the fractal dimension is found to be more than 2 for the AE generated from the plastic deformation. The fractal dimension of $m = 2$ is the critical number to evaluate the condition of materials. If there is a damage (i.e., crack) in the material, the fractal dimension becomes lower than 2.

The integrated AE event $F(x)$,

$$F(x) = \int_x^{\infty} f(x) \cdot dx = \frac{1}{m-1} cx^{-m+1} \quad (m > 1) \tag{2}$$

was observed through changing the AE signal threshold level in the measurements.

Figures 5(a) shows the AE event count per cycle as a function of the AE signal threshold level in the ferroelectric PZT ceramics. The observed AE event count logarithmically decreased with the AE signal threshold level when a field of ± 25 kV/cm was applied [Fig. 5(a)]. Thus, a fractal dimension of $m = 1(d/dx\{c \log x - A\} = cx^{-1})$ was obtained for the logarithmic decrease in the ferroelectric PZT. From the

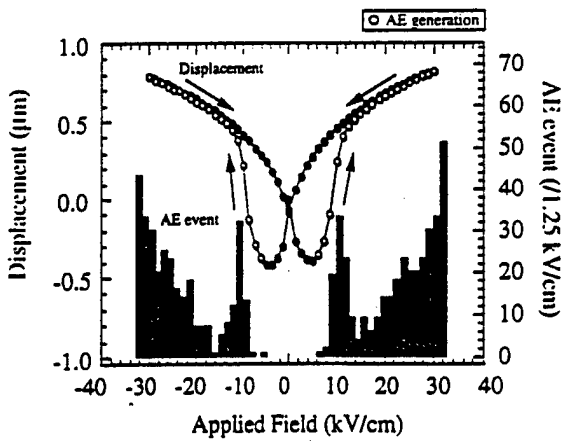

Fig. 4. AE event count and the induced displacement as a function of applied field of soft piezoelectric PLZT (9/65/35).

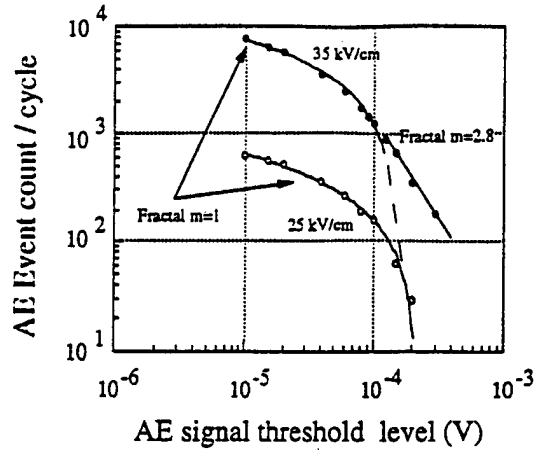

(a)

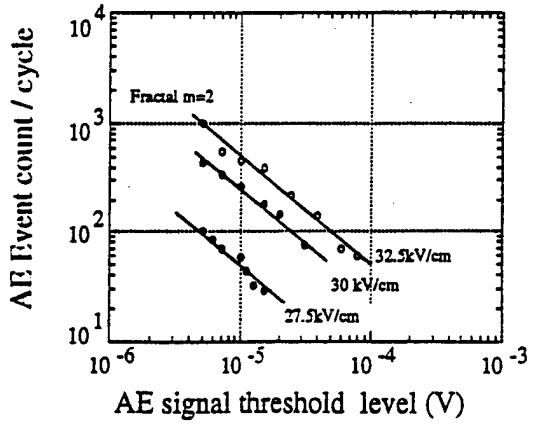

(b)

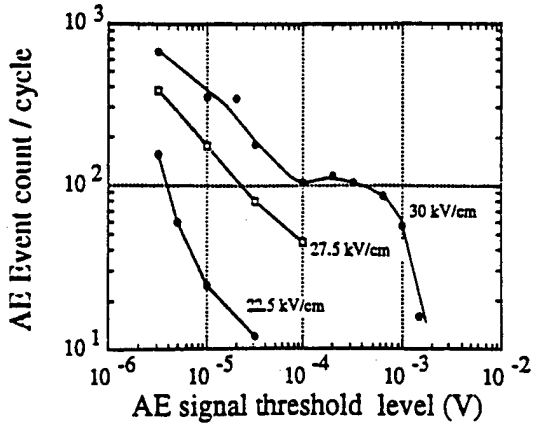

(c)

Fig. 5. AE event count per cycle as a function of the AE signal threshold level (a) ferroelectric PZT, (b) electrostrictive 0.9 PMN–0.1 PT, and (c) soft piezoelectric PLZT (9/65/35).

concept of the fractal dimension, the obtained dimension indicated that the sample had been damaged. However, since repeatable and stable field induced AE were observed, it was supposed that the lowered fractal dimension was due to the existence of ferroelectric domain and the effect of the domain reorientation related deformation, instead of the damage. When a field of ± 35 kV/cm was applied, the higher AE signal threshold level parts did not follow to logarithmic change. The lower signal threshold level region still could be fitted to a logarithmic curve and the extended line also ended around the AE signal threshold level obtained for ± 25 kV/cm. The fractal dimension of higher signal threshold level part was found to be $m = 2.8$. Since the domain reorientation was supposed to be completed at higher electric field, the origin of the AE with the fractal dimension of 2.8 was assumed to be piezoelectric deformation without domain reorientation. It was shown that the fractal dimension of the field induced AE for the domain reorientation related deformation ($m = 1$) was lower than that for the piezoelectric deformation without domain reorientation ($m = 2.8$). The fractal dimension greater than two corresponded to the plastic deformation. However, it was difficult to recognize the electrically induced deformation of ferroelectric ceramics as the plastic deformation, since the induced displacement recovers to the initial point after removing the field. Hence, it should be noted that the AE generation process in the ferroelectric ceramics could be different from that of reported AE in the materials such as metals and structural ceramics.

Figure 5(b) shows the AE event count per cycle for the electrostrictive PMN–PT as a function of the AE signal threshold level. The same slopes for the AE event count were observed at various applied fields, and the critical fractal dimension of $m = 2$ was obtained. It seems that the origin of AE in the electrostrictive PMN–PT ceramics did not change with the applied field level, and was assumed to be the internal stress caused by the electrostrictive deformation unrelated to domain reorientation.

In the PLZT (9/65/35) ceramics, the AE event count fluctuated with the applied field [Fig. 5(c)]. This fluctuation in the AE was probably due to the field induced phase change and/or domain creation. It seems that the domain reorientation related deformation, the piezoelectric deformation unrelated to domain reorientation and the field induced domain creation as well as phase related behavior caused the AE generations in the PLZT (9/65/35) ceramics. The fractal dimension of the PLZT (9/65/35) did not take a constant intermediate number between $m = 1$ and $m = 2$, but fluctuated. This was probably due to the change of AE generation source caused by the applied field.

4. Conclusion

The electric field induced acoustic emissions (AE) under the bipolar fields were studied in the ferroelectric PZT, soft piezoelectric PLZT (9/65/35) and electrostrictive 0.9 PMN–0.1 PT ceramics. The AE event rate as a function of applied field and AE signal threshold level distribution were employed to identify the origin of field induced AE.

The AE event rate in ferroelectric PZT and soft piezoelectric PLZT (9/65/35) ceramics showed two origins: domain reorientation related deformation and piezoelectric deformation without domain reorientation. On the contrary, the internal stress caused by the induced electrostrictive deformation was supposed to be the dominant AE generation source in the electrostrictive 0.9 PMN–0.1 PT ceramics.

The fractal dimension of the ferroelectric PZT ceramics consisted of the domain reorientation related $m = 1$ and the domain reorientation unrelated $m = 2.8$, when the electric field of ± 35 kV/cm was applied. The fractal dimension of $m = 2$ was obtained in the electrostrictive PMN–PT. The fluctuation of the fractal dimension was observed in PLZT (9/65/35) ceramics, which showed an intermediate state between PZT and PMN–PT in terms of the induced displacement.

It was shown that the domain reorientation related and unrelated deformations were the origins of the field induced AE in the ferroelectric ceramics. The fractal dimension of the AE caused by the domain reorientation related deformation was found to be lower than that of the AE associated with the piezoelectric deformation without domain reorientation.

Acknowledgement

This work was supported by the Office of Naval Research through Contract No. N00014-92-J-1510.

1) R. Halmshaw: *Non-Destructive Testing* (Edward Arnold, London, 1991) 2nd ed., Chap. 2, p. 273.
2) M. Guyot and V. Cagan: J. Magn. Magn. Mater. **101** (1991) 256.
3) M. Guyot and V. Cagan: J. Magn. Magn. Mater. **83** (1990) 217.
4) G. A. Evans and M. Linzer: J. Am. Ceram. Soc. (1973) 56.
5) P. Buchman: Solid State Electron. **15** (1972) 142.
6) I. J. Mohamad, E. F. Lambson, A. J. Miller and G. A. Saunders: Phys. Lett. A **71** (1979) 115.
7) V. A. Kalitenko, V. M. Perga and I. N. Salivonov: Sov. Phys. Solid State **22** (1980) 1067.
8) H. Iwasaki and M. Izumi: Ferroelectrics **37** (1981) 563.
9) Y. Saito and S. Hori: Jpn. J. Appl. Phys. **33** (1994) 5555.
10) M. Arai, Y. Sugawara and K. Uchino: *Proc. Ultrasonic Symposium, Hawaii, 1990*, IEEE, p. 1197.
11) A. Furuta and K. Uchino: J. Am. Ceram. Soc. **76** (1993) 1615.
12) H. Aburatani, S. Harada, K. Uchino, A. Furuta and Y. Fuda: Jpn. J. Appl. Phys. **33** (1994) 3091.
13) H. Aburatani and K. Uchino: Jpn. J. Appl. Phys. **35** (1996) L516.
14) H. Aburatani and K. Uchino: *Proc. 9th Int. Symp. Application of Ferroelectrics, 1996*, IEEE, p. 871.
15) H. Nakasa: *Theoretical Bases and Applications of Acoustic Emission* (Chijin Shokan, Tokyo, 1994) 1st ed. [in Japanese].

MODELING
and
CHARACTERIZATION

Electrostriction

APPENDIX 79

Reprinted from Ceramic Transactions, Vol. 88, 1998

ELECTROSTRICTION IN DIELECTRIC MATERIALS

R. E. Newnham, V Sundar, R. Yimnirun, J. Su and Q.M. Zhang
Materials Research Laboratory, The Pennsylvania State University, University Park, PA 16802.

ABSTRACT

Electrostriction is the basis of electromechanical coupling in all insulators. The quadratic electrostrictive strain x_{ij} associated with induced polarization components P_k and P_l is given by $x_{ij}=Q_{ijkl}P_kP_l$. Two converse electrostrictive effects may also be defined. In this paper, some trends in structure-property relationships that govern electrostriction are identified, along with the problems that limit our understanding of this fundamental electromechanical property. Electrostrictive coefficients range from the ~$10^{-3}m^4/C^2$ in relaxor ferroelectrics to ~$10^3m^4/C^2$ in some polymers. High sensitivity techniques such as interferometry or compressometry are necessary to accurately measure electrostrictive effects in most insulators. But even in low-K dielectrics, electrostrictive stresses may initiate breakdown in high field environments such as microelectronic components with small dimensions, high voltage insulators or in high power lasers. In polymeric materials, charge injection mechanisms may produce local electric field concentrations that can cause large electrostrictive strains. The electromechanical properties in polymers have also been observed to vary with the thickness of the specimen. A brief description of the anharmonic nature of electrostriction and its frequency dependence is included.

INTRODUCTION

Many of the recent innovations in the field of electroceramics have exploited the nonlinearities of material properties with factors such as electric field, frequency, or temperature. The nonlinear dielectric behavior of ferroelectric ceramics (fig.1), for example, has opened up new market segments in electronics and communication. In these materials, the polarization increases nonlinarly to a saturation value as the applied electric field is increased[1]. Polarization P_i varies with applied electric field E_j as :

$$P_i = \eta_{ij} E_j + \eta_{ijk} E_j E_k + ...$$

where η_{ij} is the dielectric susceptibility, and η_{ijk} the higher order dielectric susceptibility. η_{ij} is related to the dielectric constant K_{ij} by the linear relation $\eta_{ij} = (K_{ij} - 1)\varepsilon_0$.

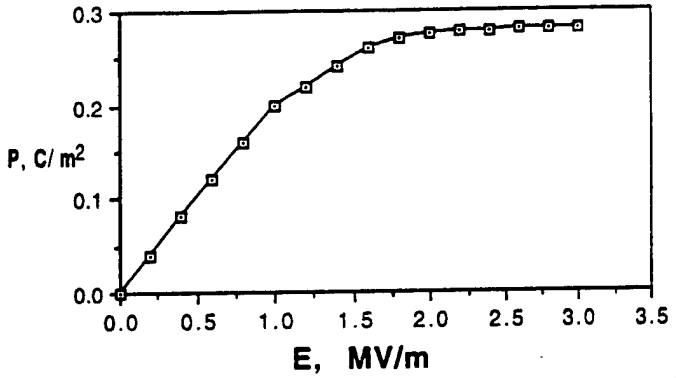

Fig. 1 : Nonlinear polarization vs. electric field behavior for the relaxor ferroelectric 0.9PMN-0.1PT in its paraelecric regime (Ref. 1).

Similarly the nonlinear elastic behavior of materials such as polymers (fig.2) has also been exploited in composite structures. In the natural vulcanized rubber shown, the strain obtained saturates as stress is increased in the low MPa range[2].

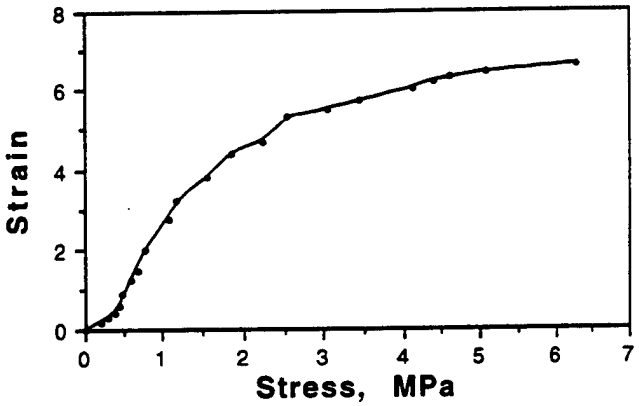

Fig. 2 : Nonlinear strain vs. stress behavior of a typical natural vulcanized rubber (Ref. 2).

Linear stress-strain behavior conforming to Hooke's law is observed only in regions of low stress. In the linear region, the strain x_{ij} is related to the stress X_{kl} by the relation $x_{ij} = s_{ijkl} X_{kl}$. Nonlinear elastic behavior in general may be described by the equation :

$$x_{ij} = s_{ijkl} X_{kl} + s_{ijklmn} X_{kl} X_{mn} + \ldots$$

where s_{ijkl} is the elastic compliance, and s_{ijklmn} the higher order elastic compliance.

Materials which display large electromechanical interactions have been exploited in the areas of stress or displacement sensing and in actuating. While most

commercial electromechanical materials and structures are based on linear or piezoelectric mechanisms, nonlinear electromechanical interactions are of interest in engineering material systems and structures with tunable properties[3]. Strains caused by linear and nonlinear electromechanical interactions may be expressed as:

$$x_{ij} = g_{ijm} P_m + Q_{ijmn} P_m P_n + ..$$

where the linear effect is associated with the piezoelectric constants g_{ijm} and quadratic nonlinear effect with the electrostriction conefficients Q_{ijmn}. These strains may also be expressed in terms of electric field related coefficients d_{ijm} and M_{ijmn} as :

$$x_{ij} = d_{ijm} E_m + M_{ijmn} E_m E_n + ..$$

Piezoelectricity is absent in centric crystals, but electrostriction, being a tensor property of even rank, can be observed in all insulating materials. Quadratic

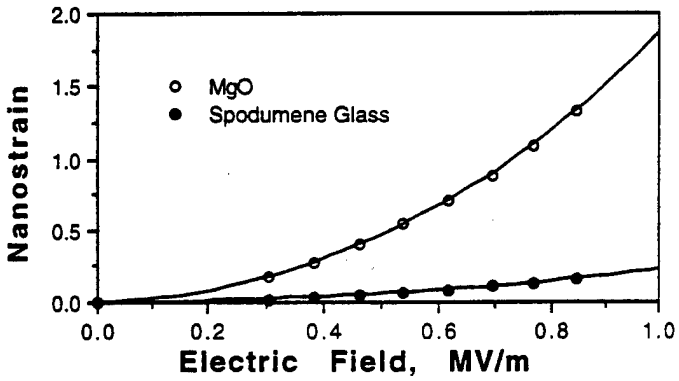

Fig. 3 : Electrostrictive strain can be observed in all insulating materials. Quadratic strain vs. electric field relationships for single crystal <100> oriented MgO and spodumene glass measured by interferometry are illustrated here.

electrostrictive strain in MgO and spodumene glass ($Li_2O{\cdot}Al_2O_3{\cdot}4SiO_2$) is illustrated in fig. 3[4]. It is also the primary electromechanical coupling mechanism in centrosymmetric materials. In this review, we look at nonlinear electromechanical interactions in the different ways in which it may be observed in materials, along with trends in structure property relationships that affect these interactions.

PHENOMENOLOGY OF ELECTROSTRICTION

Nonlinearity in electrical, elastic and electromechanical properties may be defined using the Devonshire formalism[5,6]. The elastic Gibbs function (G) for the free energy of a material may be expressed in differential form as :

$$dG = -SdT - x_{ij}dX_{ij} + E_i dP_i$$

where S is the entropy, T the temperature, x_{ij} the elastic strain tensor, X_{ij} the stress tensor, and E_i and P_i the electric field and polarization vectors. Properties relating derived variables such as S, x_{ij} or E_i to fixed variables of state such as T, X_{ij} or P_i are obtained by taking the second derivative of this free energy function. For example, the first order terms for inverse dielectric susceptibility χ_{mn} and elastic compliance s_{ijkl} may be expressed as :

$$\chi_{mn} = (dE_m/dP_n)_{X,T} = (d^2G/dP_m dP_n)_{X,T}, \text{ and}$$
$$s_{ijkl} = (dx_{ij}/dX_{kl})_{P,T} = (d^2G/dX_{ij}dX_{kl})_{P,T}$$

Cross-coupled properties can be derived by changing the differentiation variable for the second differential. The properties that introduce strain in a material are derived by differentiating the elastic Gibbs function with respect to stress. The tensor properties associated with these effects are elastic constants, linear and nonlinear thermal expansion, linear piezoelectric constants (g_{ijm}), and quadratic (Q_{ijmn}) electrostriction constants. These electromechanical interactions can be expressed in a power series to the second order (fixed X, T) as :

$$x_{ij} = g_{ijm} P_m + Q_{ijmn} P_m P_n + ..$$

Electrostriction may be thus defined as the quadratic coupling between strain and electric field, or between strain and polarization. It is a fourth rank tensor defined by the following relationships :

$$x_{ij} = M_{ijmn} E_m E_n, \text{ or}$$
$$x_{ij} = Q_{ijmn} P_m P_n$$

where M_{ijmn} the fourth rank field related electrostriction tensor and Q_{ijmn} the fourth rank polarization related electrostriction tensor. The M and Q coefficients are equivalent in linear dielectrics. Conversions between the two coefficients are carried out using the field-polarization relationships $P_m = \eta_{mn} E_n$ and $E_n = \chi_{mn} P_m$ where η_{mn} is the dielectric susceptibility tensor, and χ_{mn} is the inverse dielectric susceptibility tensor. The need for defining a polarization related electrostriction tensor arises from the fact that ferroelectrics and other materials often show nonlinearity of dielectric properties with changing electric fields. Electrostrictive strain is not always quadratic with electric field, especially in high permittivity materials with nonlinear P_i - E_j relationships (Fig. 4). Thus, it is useful to define a polarization related electrostriction coefficient Q_{ijmn} better express the quadratic nature of electrostriction in all materials.

The M coefficients are defined in units of m^2/V^2. Their values range from about 10^{-24} m^2/V^2 in low permittivity materials to 10^{-16} m^2/V^2 in high permittivity actuator materials such relaxor ferroelectrics such as lead magnesium niobate - lead

titanate compositions. Large strains of the order of strains in ferroelectric piezoelectric materials such as lead zirconate titanate may be induced in these materials for similar fields. Q coefficients are defined in units of m^4/C^2. Q values vary in an opposite way to M values. Q ranges from 10^{-3} m^4/C^2 in relaxor ferroelectrics to greater than the order of 10^3 m^4/C^2 in polyurethane films.

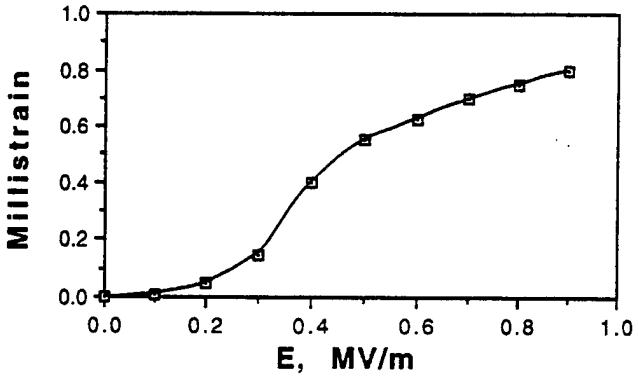

Fig. 4 : Electrostrictive strain is not always quadratic with electric field, especially for high K materials such as PMN (Ref. 1).

Fourth rank electrostriction tensors may also be expressed in collapsed Voigt notation as M_{ij} or Q_{ij}. Expressing these tensors in matrix form illustrates the effects of point group symmetry on this tensor. as applied through Neumann's principle. For example. the electrostriction matrix for cubic materials (point group m3m) is :

Q_{11}	Q_{12}	Q_{12}	0	0	0
Q_{12}	Q_{11}	Q_{12}	0	0	0
Q_{12}	Q_{12}	Q_{11}	0	0	0
0	0	0	Q_{44}	0	0
0	0	0	0	Q_{44}	0
0	0	0	0	0	Q_{44}

while the matrix for isotropic materials such as unoriented ceramics, glasses or polymers (Curie groups ∞∞m and ∞∞∞) would be of the form :

Q_{11}	Q_{12}	Q_{12}	0	0	0
Q_{12}	Q_{11}	Q_{12}	0	0	0
Q_{12}	Q_{12}	Q_{11}	0	0	0
0	0	0	$2(Q_{11}-Q_{12})$	0	0
0	0	0	0	$2(Q_{11}-Q_{12})$	0
0	0 0	0	0		$2(Q_{11}-Q_{12})$

It is also useful to define a hydrostatic electrostriction coefficient Q_h, as the variation of susceptibility with applied hydrostatic pressure. This coefficient can be useful in comparing electrostrictive effects in materials with different anisotropy characteristics. Since applied compressive stress is by convention negative, Q_h values are positive for ceramic materials, indicating the decrease of inverse dielectric susceptibility (χ) with applied pressure. $Q_h = 0.5(d\chi/dp) = Q_{11} + 2Q_{12}$ (for materials with cubic or isotropic symmetry). The Q_h, dielectric permittivity, and elastic compliance values for some common dielectric materials[9-16] are listed in Table 1.

As a consequence of the quadratic nature of the electrostriction effect, the sign of the strain produced in the material is independent of the polarity of the field. This is in contrast with linear piezoelectricity where reversing the direction of the field would cause a change in the sign of the strain.

Another consequence is that electrostrictive strain occurs at twice the frequency of an applied AC field. In acentric materials where both piezoelectric and electrostrictive strains may be observed, this fact is very useful in separating the strains arising from piezoelectricity and from electrostriction.

The electrostriction tensor can also be treated as a complex quantity, similar to the dielectric and the piezoelectric tensors. The imaginary part of the electrostriction is also a fourth rank tensor. Such a treatment could be very useful in providing a better understanding at electromechanical energy conversion in materials with relaxation mechanisms such as glasses containing alkali ions[7] or polymeric materials[8]. In this review, though, the discussion is confined to the real part of the electrostriction tensor.

Also, electrostriction in liquid and gaseous dielectrics has been studied since late in the 19th century, when studies by Roentgen[17] showed that all liquids expanded when an electric field was applied to them. In liquids, electrostriction is observed mainly as the contraction of a solvent around solute ions. Similar to solids, the electrostrictive effect in liquids is observed to be proportional to the square of the charge of the ions, inversely proportional to the ionic radius, and proportional to the value of $K^{-2}dK/dP$ for the solute[18]. This discussion, however, is confined to solid dielectrics.

DIRECT AND CONVERSE ELECTROSTRICTION EFFECTS

The electrostriction effect defined in the previous section, which relates the quadratic dependence of strain on applied field or induced polarization may be termed the direct electrostrictive effect. This effect may be expressed in terms of field related and polarization related electrostriction coefficients as :

$$Q_{ijmn} = (d^2 x_{ij} / dP_m\, dP_n) = (d^3G / dX_{ij}\, dP_m\, dP_n) \text{ or}$$

$$M_{ijmn} = (d^2 x_{ij} / dE_m\, dE_n) = (d^3G / dX_{ij}\, dE_m\, dE_n)$$

By changing the order of differentiation in the free energy term, we may derive an equivalent converse effect of electrostriction, as :

$$Q_{ijmn} = -1/2\ (d\,\chi_{ij} / d\,X_{mn}) = (d^3G / dP_i\, dP_j\, dX_{mn}) \text{ or}$$

$$M_{ijmn} = 1/2\ (d\ \eta_{ij} / d\ X_{mn}) \ = (\ d^3G / dE_i\ dE_j\ dX_{mn}\ )$$

which is the variation of dielectric susceptibility or its inverse with applied stress.

Table 1 : List of dielectric constants, elastic constants, and electrostriction coefficients of common dielectrics.

Materials	K	S ($x10^{-12}$) (m^2/N)	$S/K\varepsilon_0$ ($x10^{-4}$) (m/FN)	Q_h (m^4/C^2)	Ref
Relaxor Ferroelectric					
PLZT (11/65/35)	5900	9.50	1.82	0.007	9, 10,
$BaTi_xSn_{1-x}O_3$ (x=0.38)	10300	8.90	1.01	0.0099	11
$BaSr_xTi_{1-x}O_3$, (x=0.35)	25000	4.55	0.206	0.0069	
La/PMN-PT (1/93/97)	13000	16.42	1.43	0.006	
Perovskite Ferroelectric					
$SrTiO_3$	450	1.82	4.57	0.07	11
$PbTiO_3$	270	7.81	32.6	0.03	
$BaTiO_3$	1070	6.02	6.36	0.03	
$Pb(Ti_{1-x}Zr_x)O_3$	1700	1.52	1.01	0.018	
Glass-Ceramics					
Corning 888VE	300	7.25	27.31	0.079	9
Corning 888YT	370	5.85	17.87	0.055	
Corning 888ZF	440	4.93	12.66	0.064	
Linear Dielectrics					
Single Crystals					
CaF_2	6.8	6.92	1150	0.47	13, 4
BaF_2	7.4	15.3	2342	0.33	
$KMnF_3$	9.8	9.72	1121	0.24	
MgO	9.8	4.03	465	0.18	
Ceramics					
MgO-Doped Al_2O_3	10.5	2.90	312	1.58	This
AlN	9.5	3.03	360	0.318	work
Si_3N_4	8.7	3.13	406	1.06	
Glasses					
Na-Aluminosilicate	10.2	15.3	1696	0.519	12, 14
Fused-SiO_2	3.8	14.0	4163	0.37	
$Na_2O.3SiO_2$	11.3	16.3	1629	0.765	This
Spodumene Glass	7.9	1.18	169	0.43	work
Polymers					
PVDF	16	420	29660	2.4	15, 16,
VDF/TrFE	11	400	41090	2.5	
PVC	3.4	333	110700	10.1	This
Polyurethane	6.5	25000	4346000	850	work

It is also possible to define a second converse effect, in which electrostriction is defined as the variation of the piezoelectric voltage coefficient g_{ijk} with the induced polarization.

$$Q_{ijkl} = -1/2 \, (d \, g_{ijk} / dP_l)$$

ELECTROSTRICTION IN RELATION TO OTHER ANHARMONIC MATERIAL PROPERTIES

It is necessary to model anharmonic behavior to describe some macroscopic properties that cannot be modeled using the harmonic approximation in solid state theory. Some of these properties are the thermal expansion coefficient, the isothermal compressibility, its pressure coefficient, and electrostriction, all of which contribute to the macroscopic Gibbs free energy, and are typically defined like compliance coefficients.

Modeling anharmonic properties from first principles involves much effort in computational theoretical physics. However, simpler atomistic models, in combination with empirical correlations, can provide some understanding of electrostriction in relation with other anharmonic properties.

Under the action of an applied electric field, the cations and anions in a crystal structure are displaced in opposite directions by an amount Δr. This displacement is responsible for the electric polarization, the dielectric constant, and the electrostrictive strain[3]. To a first approximation, we may express the relation between these as :

$$Q = x/P^2 \sim (\Delta r)/(\Delta r)^2 = 1/\Delta r \sim 1/K$$

Plotting Q_h as a function of the dielectric permittivity (fig. 5) reveals two distinct trends, one for materials with cubic perovskite structures and another for other materials. Perovskite materials of comparable compliances follow the $Q \sim 1/K$ relation. However, linear dielectric with a large range of compliances and a small range of dielectric constants do not follow this relationship. For example, diamond is a very covalent material with a very low complaince, and has a $Q_h \sim 0.02$. Introducing a larger compliance range by including soft polymer dielectrics can further dilute this relationship.

Large strains in compliant solids such as polymers can introduce large changes in the dielectric stiffness and in anharmonic potentials. Electrostrictive strain is displacive and acts against the elastic forces in a material. Introducing the elastic compliance s into the Q vs. K relationship can better express the correlation between these properties. Through the first converse effect, electrostriction is proportional to the change of dielectric stiffness β with stress X, which may be expressed as $Q \sim (\Delta\beta)/(X) \sim x/(x/s) \sim s$

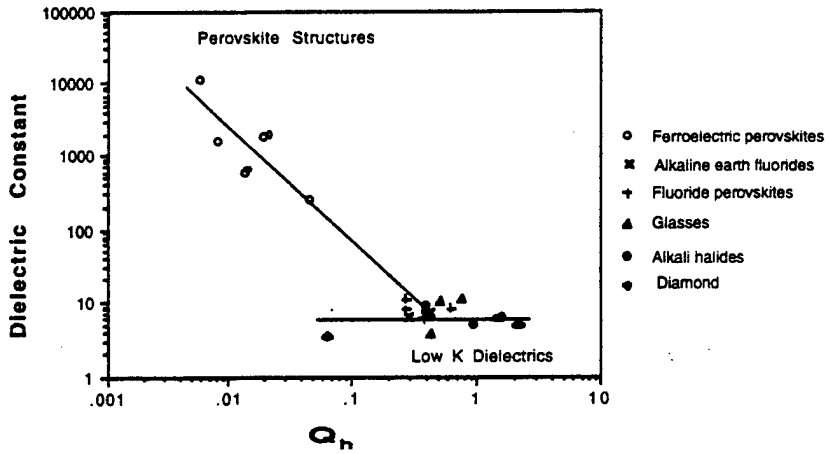

Fig. 5 : Variation of $Q_h(m^4/C^2)$ with dielectric constant for various materials.

Empirically, Log (Q_h) is seen to vary nearly linearly with log ($s/\varepsilon_0 K$) (Fig. 6). This combination of the compliance and the deielectric properties of a materials may be used as a predictor of the size of electrostriction effects in insulators.

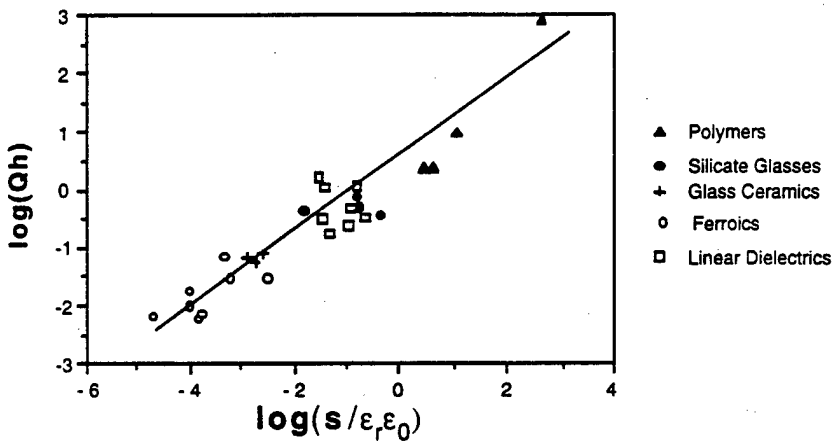

Fig. 6 : Variation of log $Q_h(m^4/C^2)$ with log ($s/\varepsilon_0 K$) for various materials inluding polymers shows a near linear relationship

Electrostrictive coefficients have also been related to other anharmonic properties such as the thermal expansion coefficient, the isothermal volume compressibility, and the pressure derivative of the volume compressibility with comparable levels of correlation. More complicated shell models and quasiharmonic models have also been attempted for electrostriction[19,20,21]. The development of an

a priori model to accurately predict electrostriction in linear dielectrics is held back in part by the lack of reliable and accurate measurements of electrostriction in these materials and also by the complexity of the problem.

ELECTROSTRICTION IN ANTIFERROELECTRIC AND FERROELECTRIC MATERIALS

In a ferroelectric material, that exhibits both spontaneous and induced polarizations, P^F_i and P^i_j, the strains arising from spontaneous polarizations, piezoelectricity, and electrostriction may be formulated as :

$$x_{ij} = Q_{ijkl} P^F_k P^F_l + 2 Q_{ijkl} P^F_k P^i_l + Q_{ijkl} P^i_k P^i_l$$

Leaving out the negligibly small pure electrostrictive contribution in the ferroelectric state, we may express the piezoelectric voltage coefficient g_{ijk} as :

$$g_{ijk} = dx_{ij} / dP^i_l = 2 Q_{ijkl} P^F_k$$

Electrostriction has been shown to be the origin of piezoelectricity in ferroelectric materials in conventional ceramic ferroelectrics such as barium titanate as well as in organic polymer ferroelectrics such as vynilidene fluoride copolymers (PVDF)[15].

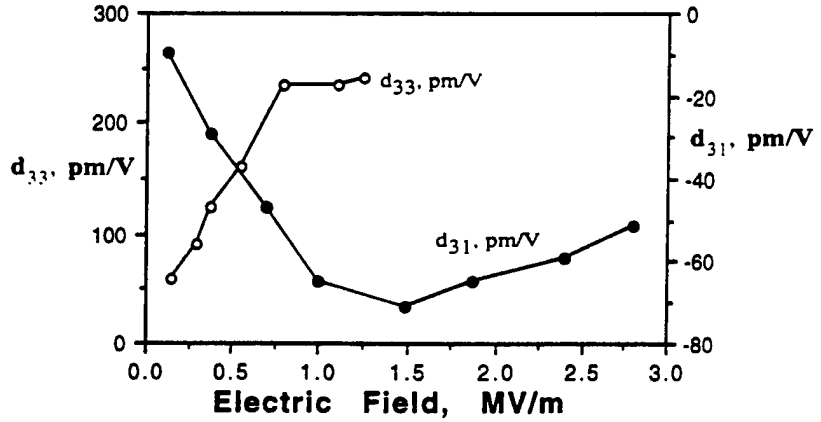

Fig. 7 : Variation of longitudinal and transverse d coefficients with applied electric field for electrostrictive PMN, 18°C (Ref. 1).

This origin of piezoelectricity in electrostriction provides us an avenue into nonlinearity. The piezoelectric coefficient and the dielectric behavior of a transducer can be tuned to desired values. The piezoelectric coefficient varies with the polarization induced in the material, and may be controlled by an applied electric field (Fig. 7). The electrostrictive element may be tuned from an inactive to a highly active state. The electrical impedance of the element may be tuned by exploiting the

dependence of permittivity on the biasing field for these materials, and the saturation of polarization under high fields[3,21].

Electrostrictive coupling between sublattices has also been proposed as a mechanism to explain piezoelectric anisotropy in antiferroelectric ceramics[22]. In a two-sublattice model, if Q_{ij} denotes the conventional electrostriction tensor, and q_{ij} the corresponding intersublattice coupling parameters, then the strains arising from spontaneous polarizations and induced polarizations P^F_k and P^i_k, in the ferroelectric state may be written in Voigt notation as :

$$x_k = (Q_{kl} + q_{kl})(P^F_k)^2 + 2(Q_{kl} + q_{kl}) P^F_k P^i_k + (Q_{kl} + q_{kl}) (P^i_k)^2$$

When a spontaneous polarization is induced, the pure electrostrictive contribution from induced polarizations alone is negligible, and we may express the piezoelectric coefficient d_{kl} as $d_{kl} = dx_k / dP^i_k = 2(Q_{kl} + q_{kl}) P^F_k$

The strains x^{AF}_k associated with the field induced transition from antiferroelectric to ferroelectric states and spontaneous strains x^{PF}_k observed at the transition from paraelectric to antiferroelectric states can be expressed in terms of the spontaneous polarization in the ferroelectric state, P^F_k, and P^A_k, the spontaneous polarization in the antiferroelectric state as :

$$x^{AF}_k = 2q_{lk}(P^F_k)^2 \text{ and } x^{PF}_k = (Q_{kl} - q_{kl})(P^A_k)^2$$

The piezoelectric anisotropy factor d_{ij}/d_{ik} may then be calculated as :

$$d_{ij}/d_{ik} = (Q_{ij} + q_{ij})/(Q_{ik} + q_{ik})$$

Estimations of q_{ij} (~ 0.01 m^4/C^2) show in antiferroelectric materials show that they are comparable to but smaller than Q_{ij} (~ 0.06 m^4/C^2) values.

SOME APPLICATIONS OF ELECTROSTRICTION

Despite the fact that electrostriction was initially relegated to the role of an esoteric, and at best secondary effect, the number of applications of the phenomenon, both theoretical and practical, has been increasing significantly since the introduction of PMN as a prototype electrostrictive material[1]. Most applications take advantage of the electrostrictor as an actuator, exploiting the anhysteretic, tunable nature of the electromechanical response. Mechanical applications range from stacked actuators, through inchworms, micro angle adjusting devices, and oil pressure servo valves[23,24]. These are in the main servo-transducers, deployed as micropositioning devices, featuring a reproducible, non-hysteretic deformation response on the application of an electric signal of suitable magnitude.

The advantages that electrostrictors have over other actuator materials include low hysteresis of the strain-field response, no remanent strain (walk off), reduced aging and creep effects, a high response speed (<10ms), and strain values (>0.03%) achievable at realizable electric fields. Displacement ranges of several tens of microns may be achieved with $\pm 0.01\mu$ reproducibility. Most actuator

applications of electrostrictors as servo transducers and micropositioning devices take advantage of these characteristics. Mechanical applications range from stacked actuators through inchworms, microangle adjusting devices, and oil pressure servo valves. Multilayer actuators produce large displacements and high forces at low drive voltages. The linear change in capacitance with applied stress of an electrostrictor can be used as a capacitive stress gage[25]. Electrostrictors may also be used as used in field tunable piezoelectric transducers. Recently, electrostrictive materials have been integrated into ultrasonic motors and novel flextensional transducers.

Electrostrictors have also been integrated into "smart" optical systems such as bistable optical devices, interferometric dilatometers and deformable mirrors. Electrostrictive correction of optical aberrations is a significant tool in active optics. Electrostrictors also find applications in "very smart" systems such as sensor-actuator active vibration suppression elements. A shape memory effect arising from inverse hysteretic behavior and electrostriction in PZT family antiferroelectrics is also of interest.

In selecting electrostrictive relaxor ferroelectrics for actuator and sensor applications, the following criteria are commonly used. A large dielectric constant and field stability in the K vs. E relations are useful in achieving large electrostrictive strains. These criteria also lead to large induced polarizations and large induced piezoelectric coefficients through the second converse effect. Broad dielectric transitions allow for a large operating temperature range. Minimal E-P hysteresis and no remanent polarization are useful in achieving a low loss material that is not susceptible to Joule heating effects. These factors are listed in Table 2.

Table 2 : Selection Critera for Ceramics for Electrostrictive Devices.

Desirable Properties	Material Behavior
• Large strain, induced polarization, and induced piezoelectricity	• Large dielectric constants
• Large operating temperature range	• Broad dielectric transition
• Low loss, low joule heating, minimal hysteresis, no remanent polarization	• Operation in paraelectric regime ($T > T_{max}$)

As a fundamental effect, electrostriction may prove to be an important factor in the design of sub-micron electronic devices. The present focus is on synthesis of materials with large electrostriction effects. The other extreme of the scale may prove to be of interest, too. As microelectronic devices are taken to smaller dimensions, the increased field levels on the materials can cause quadratic electrostrictive effects ($x \alpha E^2 \sim 1/t^2$) to predominate over inear piezoelectric effects ($x \alpha E \sim 1/t$) .This effect is illustrated for silica, using the piezoelectric d coefficients of quartz ($d \sim 10^{-12}$ m/V) and electrostrictive M coefficients of silica glass ($M \sim 10^{-21}$ m^2/V^2) in fig.8. An applied voltage of 10V is assumed, and piezo and electrostrictive strains are plotted for devices of various thicknesses. Oxide layers in semiconductors are typically a few hundreds of angstroms thick. Around

thicknesses of 100Å, the electrostrictive strain can be larger than the piezoelectric contribution, and close to breakdown strains for ceramics. It is then tempting to consider designing a material with zero electrostriction coefficients, for applications in areas where field induced damage is a significant risk. Other, more benign options are also offered by the effect in an increasing array of novel sensor and actuator applications, that make it well worth further study.

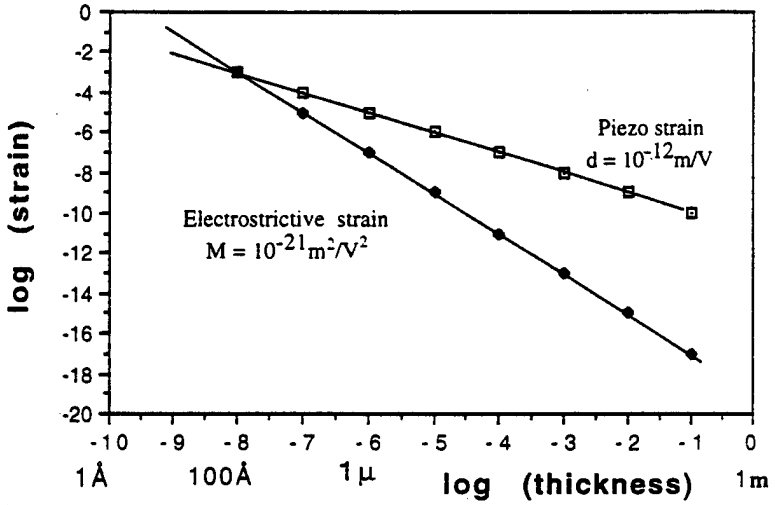

Fig.8 : Strains from piezoelectric quartz and electrostrictive amorphous silica glass for devices of varying thickness, with a voltage of 10V across the device. A typical d coefficient ~ 10^{-12}m/V and M coeffiient ~ $10^{-21}m^2/V^2$ were assumed.

MEASURING A RANGE OF ELECTROSTRICTIVE EFFECTS

A variety of experimental methods have been employed to measure a wide range of electrostrictive effects in dielectric materials. The direct and converse electrostriction effects are of importance in that they offer two independent and equivalent techniques of measuring electrostriction in a material :

a) by measuring the strains induced in materials in response to applied fields or induced polarizations, using the direct effect, and

b) measuring the change in permittivity (via the change in capacitance) under an appropriate stress using the converse effect.

The detection of small electrostrictive strains and the accurate evaluation of electrostrictive properties in most low permittivity materials is a necessarily intricate process. For a field strength of 10^6 V/m, the typical induced strain in a centric ionic material is of the order of 10^{-9}. This translates into a displacement of 10^{-12} m, or 0.01Å for a sample 1mm thick.. However, experiments to measure electrostrictive effects have been carried out since the turn of the 20th century. An early review of electrostriction by Cady[26] cites several measurements of electrostriction in insulators such as gases, oils, rubbers, glasses and cements. These effects were

measured by evaluating the expansion or the contraction of a condenser - probably a Leyden jar in the case of early measurements.

Widely used experimental techniques include the strain gauge method in which the output from a strain gage (usually pasted on the displacing sample) is used to measure the displacement in a given direction. The increased sensitivity and available in linear voltage displacement transformers (LVDTs) and potentiometers have made them another tool to measure displacements in electrostrictive materials[25]. The strain gage and LVDT techniques are typically used for materials with larger strains, typically of the order of 10^{-4} or greater. The technique of capacitance dilatometry involves measuring the change in capacitance arising from the electrostrictive displacement of one face of a parallel plate capacitor. The accuracy of early capacitance dilatometry measurements may have been limited by the unavailability of phase locking and sophisticated electronic feedback loops incorporated into the system to compensate for thermal drift [28,29].

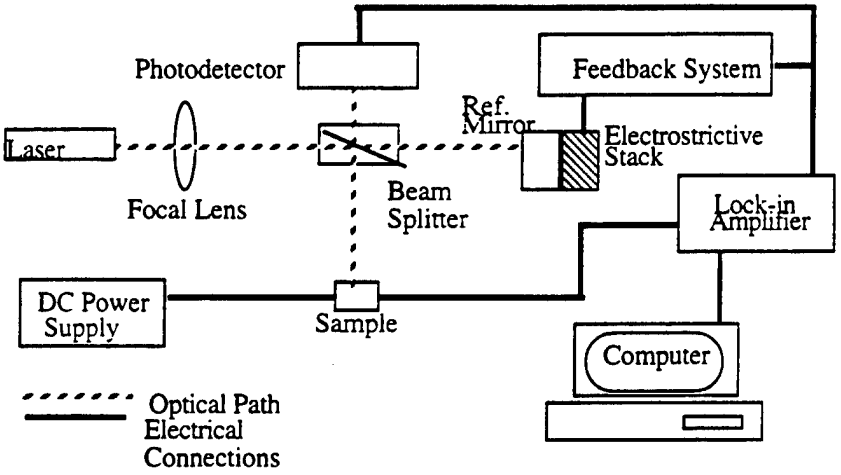

Fig. 9 : Schematic of a typical interferometric ultradilatometer, showing system components, optical paths and electrical connections (Ref. 33)

Homodyne and heterodyne laser ultradilatometers based on Michelson interferometers have been used since the 1930s to measure very small displacements[30,31,32,33]. These instruments detect the shifts in interference fringes caused by changes in path length of two laser beams, one of which is reflected from the surface of a sample under an ac field. Using phase locking and feedback loops to stabilize the system, interferometers are capable of resolutions of 10^{-3}Å or better, and usually operate in the range of 1kHz to 100kHz (Fig.9). Typical results from interferometry measurements for MgO and spodumene glass are shown in fig.3.

Recently, a bimorph based dilatometer similar in principle to an atomic force microscope has been introduced. This instrument is capable of measuring

displacements of the order of 0.01Å in a frequency range of 1 to 100kHz, and is useful in studying electrostriction in thin films (Fig.10)[34].

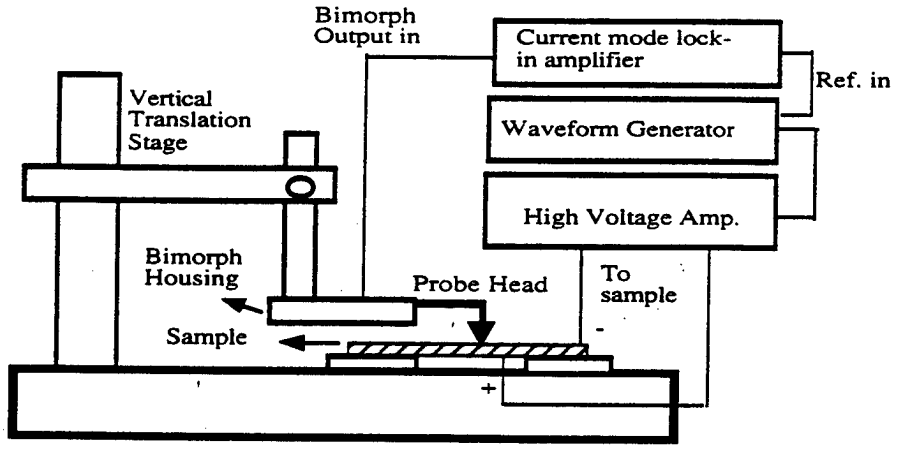

Fig. 10 : Schematic of the bimorph dilatometer for measuring electromechanical response in polymer thin films (Ref. 34)

In most direct effect measurements, the electrostatic attractive stress between opposite charged faces of a dielectric material can contribute to the dimensional change. This stress is called the Maxwell stress, and the corresponding strain x_M is dependent on the dielectric and elastic properties of the material. With all quantities being measured in the direction of the field, x_M is given by[35] :

$$x^M = -0.5\ \varepsilon_0\ \varepsilon_r\ s\ E^2$$

This correction is significant mainly in the case of low permittivity materials where very small strains are observed and for elastically soft polymers.

Techniques for measuring the converse effect call for precision evaluation of dielectric properties. small capacitance changes of the order of 10^{-16} - 10^{-15} F need to be resolved for applied stresses of the order of 0.1MPa for low permittivity ceramic materials. Other requirements are stable temperature control and the establishment of 'true' stress systems - completely hydrostatic if the hydrostatic Q_h coefficients are being measured and truly uniaxial stresses in compressometry (Fig. 11a)[7,36].

Modifications to compressometric systems are aimed mainly at improving sensitivity or uniaxiality for accurate evaluation of the separated components of the electrostriction tensor[37,38]. A correction corresponding the capacitance change due to the geometric shape change of the dielectric from elastic strain has to be performed to calculate accurate Q_{ij} values in low permittivity dielectrics when the

converse method is used. Results from compressometry measurements for some common ceramics are illustrated in fig.11b.

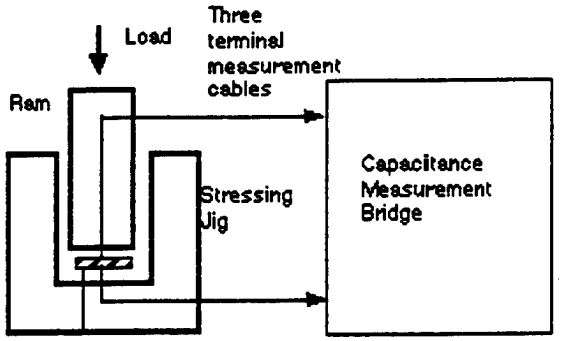

Fig. 11a : Schematic of a converse method measurement system. The sample is shown shaded (Ref. 48).

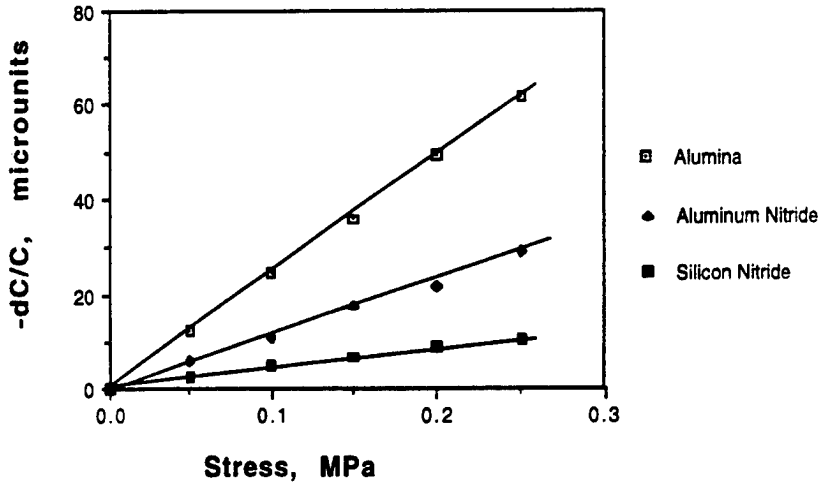

Fig. 11b : Compressometery results for ceramic alumina, aluminum and silicon nitride.

In the case of low permittivity materials, it is necessary to measure electrostriction by both direct and converse methods to calculate reliable and accurate Q or M values (Table 3).

Some recent studies on quartz have used the change in resonant frequency of the vibration modes of the material caused by a dc field[39], or the dc field induced variations in the transit times of ultrasonic pulses in the material[40]. These methods are used to calculate combinations of the electroelastic and the electrostrictive

constants of quartz, as well as the nonlinear piezoelectricity and the permittivity tensors. While the method yields accurate results for the piezostriction, the electrostriction values show poorer agreement with values in the literature.

Table 3 : Comparison of direct and converse method measurement results for a variety of dielectric materials. These values agree to within ±5% (Refs. 4, 12)

Material		Direct Q_{11} m^4/C^2	Converse Q_{11} m^4/C^2
BaF_2	Q_{11}	-0.33	-0.31
	Q_{12}	-0.29	-0.29
	Q_{44}	1.46	1.48
Spodumene Glass ($Li_2O{\cdot}Al_2O_3{\cdot}4SiO_2$)		0.43	0.46
$KMnF_3$	Q_{11}	0.51	0.49
	Q_{12}	-0.09	-0.10
	Q_{44}	1.16	1.15
CaF_2	Q_{11}	-0.48	-0.49
	Q_{12}	-0.48	-0.48
	Q_{44}	1.99	2.01
LiF		0.79	0.57
888 VE Corning Glass Ceramic		0.081	0.079
MgO		0.33	0.34
BeO		1.45	1.48
SrF_2	Q_{11}	-0.33	-0.33
	Q_{12}	0.38	0.39
	Q_{44}	2.01	1.90
3% Ca / PMN-PT		0.00289	0.00333
Calcite		1.20	1.19

ELECTROSTRICTION AND POLARIZATION MECHANISMS

The basic mechanisms contributing to the polarization in dielectric materials have been identified and treated extensively[41]. Electrostriction is a polarization related effect defined as $x_{ij} = Q_{ijkl}P_kP_l$. An understanding of the mechanisms of polarization, especially the ionic and electronic can offer further insight into the underlying mechanisms, and is useful in discerning trends in the electrostrictive behavior. especially in low permittivity linear dielectrics. Electrostriction measurements on most crystalline materials have been performed only over limited frequency ranges (10^5Hz and below). Little variation of the Q coefficients with the frequency of measurement is seen for most crystalline ionic solids. Measurements over wider ranges of frequencies may be necessary to directly study the frequency dependence of electrostriction.

The variation of the low frequency dielectric constants with temperature and pressure has been a subject for analysis by physicists for several decades[42,20]. Several studies review the changes in refractive index of solids with pressure, and attempt to explain these changes in terms of the polarizabilities of ions[43,44]. These two sets of data may be combined to analyze the electronic and ionic contributions to electrostriction. The electronic and ionic contributions to electrostriction may be compared for some well characterized oxide and fluoride materials. Results from studies on hydrostatic Q_h electrostriction coefficients of low permittivity fluorides[45] are used in this analysis, along with measurements of the change of refractive index of solids with pressure[46,47].

The electrostrictive contribution from both ionic and electronic polarization mechanisms at low frequencyies is proportional to the ratio $1/\varepsilon_r\ (d\varepsilon_r/dp)$. Using the approximation $n^2 \sim \varepsilon_e$ where n is the refractive index of the material and ε_e the electronic or high frequency dielectric constant we may calculate $1/\varepsilon_r\ (d\varepsilon_e/dp) \sim 1/\varepsilon_r\ (dn^2/dp)$ from the dn/dp data. To compare the relative contributions of the electronic and ionic polarizations at low frequencies, the same low frequency (1kHz) value for ε_r was used in both $1/\varepsilon_r\ (d\varepsilon_e/dp)$ and $1/\varepsilon_r\ (d\varepsilon_r/dp)$ ratios. The data used here was measured at pressures of 1kbar and less so that no nonlinearity was apparent in dn/dp or $d\varepsilon_r/dp$. The results are listed in Table 4 for eight oxide and fluoride materials.

Table 4 : $1/\varepsilon_r\ (dn^2/dp)$ and $1/\varepsilon_r\ (d\varepsilon_r/dp)$ for some oxides and fluorides.

Material	$1/\varepsilon_r.d\varepsilon_r/dp)$ m^2/N	$1/\varepsilon_r\ (dn^2/dp)$ m^2/N
$KMnF_3$	-4.39×10^{-11}	8.79×10^{-13}
CaF_2	-3.42×10^{-11}	1.5×10^{-12}
BaF_2	-4.29×10^{-11}	3.8×10^{-12}
LiF	-5.08×10^{-11}	4.2×10^{-13}
MgO	-2.58×10^{-11}	-9.5×10^{-13}
$KTaO_3$	-1.38×10^{-10}	-6.7×10^{-14}
$SrTiO_3$	-2.74×10^{-10}	-2.9×10^{-14}
Silica Glass	-1.5×10^{-11}	1.03×10^{-13}

It may be seen that most of the oxides in this analysis show a decrease in refractive index with pressure. This is true also for α-Al_2O_3, ZnO, stoichiometric and nonstoichiometric $MgAl_2O_4$ spinels, α-ZnS and α-CdS[44]. Most fluorides on the other hand show an increase in n with pressure. Low frequency dielectric

constants decrease with pressure for both oxide and fluoride materials. The differing behaviors at different frequencies are caused by the relative magnitude of the electronic and ionic polarizations to electrostriction. In general the ionic contribution to electrostriction is at least two orders of magnitude greater than the electronic contribution, neglecting sign. The polarization effects caused by the relative shifting of the anion sublattice with respect to the cation sublattice in the crystal dominates the change in electronic polarizabilities of the various ions with pressure.

Both positive and negative values of dn/dp are observed. This holds out the tantalizing possibility of manipulating electrostriction values. By choosing materials with predominantly electronic polarizability contributions, and probably combining or doping them, it may be possible to achieve specific (especially zero) electrostrictive responses in materials. This would involve further research into the variaion of electrostrictive effects with frequency, and possible mixing rules for electrostriction. The possibility of achieving zero electrostriction through the manipulation of crystal anisotropy has been discussed in an earlier work[48].

ELECTROSTRICTION IN POLYMER DIELECTRICS

Piezoelectric and electromechanical coupling properties have been well characterized for ferroelectric polyvinylidene fluoride (PVDF) and its copolymers with trifluoroethylene (TRFE). Their applications have been limited mainly by their lower electromechanical activity when compared to conventional ceramic actuator materials. Recently, there has been renewed interest in nonferroelectric polyurethane elastomers because of their large field induced strain response, which is primarily electrostrictive. These materials could have promising applications in sensor, actuator and microelectromechanical systems technology[8,49,27].

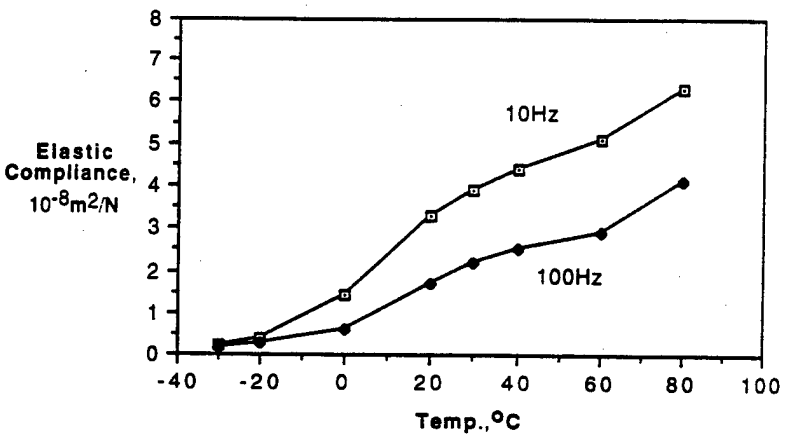

Fig. 12 : Elastic compliance vs. temperature curves for Dow 2105-80AE polyurethane elastomers at 10 and 100Hz (Ref. 50)

Some unusual effects have been observed in these polymer electrostrictors. The first is the large strain response. Strains of the order of 0.25% have reproducibly been achieved in these polymer systems for fields of the order of 1MV/m. In discussing these materials, it may be more practical to define an effective field induced strain coefficient R_e ($x = R_e E^2$), to calculate the large strains achieved in these materials.

A strong temperature effect is observed, as may be expected from the nonlinear temperature dependence of the compliance of this polymer (Fig.12). The Maxwell stress induced strain in these materials is given by :

$$x_M = - 0.5 \, s \, \varepsilon_0 \, K \, E^2$$

A Maxwell strain coefficient R_m similar to R_e can be defined to calculate the percentage of Maxwell stress contribution. Below the glass transition temperature T_g, the Maxwell stress contributions are fairly small (~10%) while above T_g, the Maxwell stress contribution to the field induced strain response increases to about 35-50% . A strong frequency dependence is also observed (Fig. 13a).

One effect that may help explain the large field induced strain in these materials is the thickness dependence of R_e. The induced strain and correspondingly, R_e , initially increased with increasing thickness and then decreases (Fig. 13b). Experiments with different electrode materials and thermally stimulated discharging current measurements support the hypothesis that effects related to charge injection, or interfacial charge may cause these dependencies.

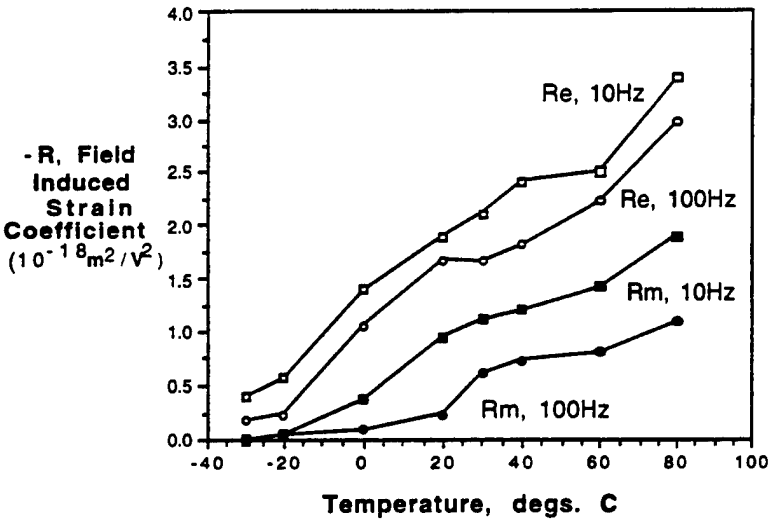

Fig. 13a : Field induced strain coefficient R_e and Maxwell strain coefficient R_m for unfiltered polyurethane thin films, at RT, 10 and 100Hz, through the glass transition for Dow 2105-80AE polyurethane elastomer (Ref. 50).

Some unusual effects have been observed in these polymer electrostrictors. The first is the large strain response. Strains of the order of 0.25% have reproducibly been achieved in these polymer systems for fields of the order of 1MV/m. In discussing these materials, it may be more practical to define an effective field induced strain coefficient R_e ($x = R_e E^2$), to calculate the large strains achieved in these materials.

A strong temperature effect is observed, as may be expected from the nonlinear temperature dependence of the compliance of this polymer (Fig.12). The Maxwell stress induced strain in these materials is given by :

$$x_M = - 0.5 \, s \, \varepsilon_0 \, K \, E^2$$

A Maxwell strain coefficient R_m similar to R_e can be defined to calculate the percentage of Maxwell stress contribution. Below the glass transition temperature T_g, the Maxwell stress contributions are fairly small (~10%) while above T_g, the Maxwell stress contribution to the field induced strain response increases to about 35-50% . A strong frequency dependence is also observed (Fig. 13a).

One effect that may help explain the large field induced strain in these materials is the thickness dependence of R_e. The induced strain and correspondingly, R_e , initially increased with increasing thickness and then decreases (Fig. 13b). Experiments with different electrode materials and thermally stimulated discharging current measurements support the hypothesis that effects related to charge injection, or interfacial charge may cause these dependencies.

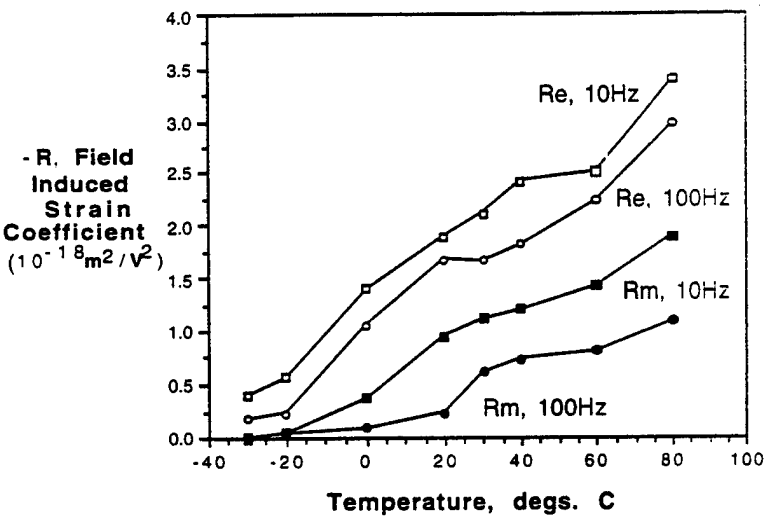

Fig. 13a : Field induced strain coefficient R_e and Maxwell strain coefficient R_m for unfilled polyurethane thin films, at RT, 10 and 100Hz, through the glass transition for Dow 2105-80AE polyurethane elastomer (Ref. 50).

When a polymer dielectric with metal electrodes is subjected to a high voltage, charge injection can occur in this material. Injected charges can then be trapped in various sites such as defects. interfaces etc., and their effects can show a strong thickness and frequency dependence. Filtering polyurethane polymers before solution casting markedly reduces the field induced strain observed in these materials (Fig. 13b) and the frequency dispersion as well, supporting the charge injection hypothesis. The dielectric and elastic properties are not significantly changed by filtering.

Injected charges can also cause enhanced nonuniform local electric fields, depending on the film thickness. The depth of the region of the polymer with enhanced local fields from charge injection is determined by the transport coefficients of the charges in the polymer film under an electric field. The volume fraction of the polymer with enhanced local fields increases with a decrease in sample thickness. After a critical thickness, though, charge neutralization and homogenization processes reduces the local field enhancement. The strain responses correspondingly decrease[50].

The nonlinear compliance behavior of these polyolyurethane elastomers, combined with unusual polarization behavior from interfacial charge effects, can make for large induced strains that are thickness dependent. Further work in this area may identify the specific chemistry responsible for the large strains associated with charge injection, and their applications in sensor and actuator areas.

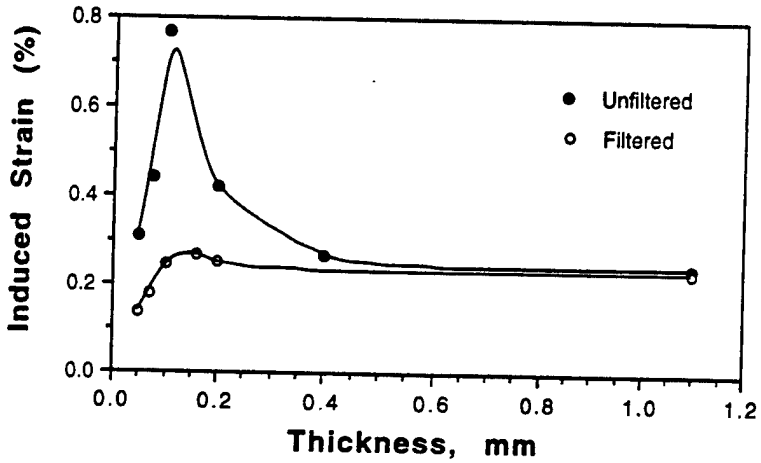

Fig. 13b : Induced strain as a function of thickness (using identical applied electric fields) for filtered and unfiltered electrostrictive polyurethane thin films, at RT, 10Hz (Ref. 50).

SUMMARY

As a summary, some common misconceptions about electrostriction to describe the key ideas set out in this paper are listed here.

1. *Electrostrictive strain is proportional to the square of the applied electric field* : For most low permitivity dielectrics, P is proportional to the applied field E, and therefore this statement is true. However, for high fields, polarization can saturate for high permittivity materials, especially in ferroelectric ceramics. A linear

relationship is observed when strain is plotted as a function of the square of polarization for these materials, but not as afunction of the electric field. So it is more accurate to say that electrostrictive strain is proportional to the square of the induced polarization.

2. *Large voltages are required to observe electrostriction* : Two factors have made this a misconception. The introduction of thick and thin film capacitors has enabled high field levels to be achieved even in low permittivity materials at low voltages. Also, the introduction of high dielectric constant relaxor ferroelectrics have raised polarization levels to new heights, further contributing to large electrostrictive strains with relatively modest voltages.

3. *Electrostriction constants are about the same size for all materials, and materials with larger electrostriction coefficients produce the largest strains* : Q constants measured for solids vary from the order of $10^{-3}m^4/C^2$ for relaxor ferroelectrics to 1 for low permittivity insulators. Larger Q values have been observed for polymer materials. The induced electrostrictive strain is proportional to the square of the polarization, which implies the square of the relative permittivity is introduced in the strain - electric field relation. For similar electric fields, materials with large dielectric constants produce the larger starins.

4. *Thermal expansion effects make electrostrictive micropositioners and stress gauges impractical* : This statement is true for low permitivity oxide ceramics but not relaxor ferroelectrics. For PMN type ceramics, $Q \sim 0.01m^4/C^2$, $K \sim 10{,}000$ and the thermal expansion cofficient $\alpha \sim 10^{-6}K^{-1}$. The electrostrictive strain in these ceramics for a field around 1MV/m is 10^{-3}, which corresponds to a 1000°C change in temperature! Relaxor ferroelectrics can also have abnormally low thermal expansion coefficients near their diffuse phase transitions, where K values are quite large.

In conclusion, though electrostriction effects can be very small in common materials, experimental techniques using phase and frequency selection can help in achieving accurate and reliable measurements of M and Q coefficients. Being a nonlinear effect, electrostriction may be applied smart systems requiring tunable properties. Electrostriction is a significant electromechanical coupling mechanism in many high field situations. Investigating the variation of electrostriction with frequency can reveal the contributions of various polarization mechanisms to electrostrictive effects. In areas such as polymer thin films, the effects of charge injection and defects can produce anomalously large strains that are worth further investigation. Electrostriction still poses a range of problems and challenges in the areas of modeling, and in terms of a fundamental understanding of a well known effect.

ACKNOWLEDGMENTS

This study was sponsored by the National Science Foundation through contract DMR 9634101, Electrostriction in Ceramics and Glasses.

REFERENCES

[1]Jang, S.J. , Ph.D. Thesis, Pennsylvania State University, Univ. Park, PA, 1979.

[2]McCrum, N.G., Read, B.E., Williams, G., Anelastic and Dielectric Effects in Polymeric Solids, Dover Publications, Mineola, NY, 1991.

[3]Newnham, R.E., Chemistry of Electronic Ceramic Matlerials, Proc. Int. Conf., Jackson, WY, 1990; NIST Special Publication **804**, 39, 1991.

[4]Sundar, V., Li, J-F., Viehland, D., Newnham, R.E., Mat. Res. Bull., **31**, p555, 1996.

[5]Cross,L.E., Phil. Mag., **1**, 76, 1956.

[6]Devonshire, A.F., Adv. Phys., **3**, 94, 1954.

[7]Pan,W.Y., Cross,L.E., Rev. Sci. Instrum., **60**, 2701, 1989.

[8]Zhenyi, M., Scheinbeim, J.I., Lee, J.W., Newman, B.A., J. Polymer Sci. Part B: Polymer Phys., **32**, p2721, 1994

[9]Sundar, V., WaGachigi, K., McCauley, D., Markowski, K.A., Newnham, R.E., Proc. ISAF 1994.

[10]Landolt-Bornstein, Num. Data on Func. Relns. in Sci. and Tech., New Srs., Gp. III. **24**, Springer-Verlag, New York, NY, 1990.

[11]Uchino, K., Cross, L.E., Jpn. J. Ap. Phys., 19, L171, 1980

[12]Sundar, V., Newnham, R.E., Mat. Res. Bull., **31**, p545, 1996.

[13]Simmons, G., Wang, H., Single Crystal Elastic Consts. and Calculated Aggregate Properties: A Handbook, MIT Press, Cambridge, MA, 1971.

[14]Sun, Y., Cao, W.W., Cross, L.E., Mater. Lett., **4**, p329, 1986.

[15]Furukawa, T., Seo, N., Jap. J. Appl. Phys., **29**, p675, 1990

[16]Brandrup, J., Immergut, E.H., Polymer Handbook, Interscience Pub., New York, NY, 1966.

[17]Roentgen, W., Annalen der Physik, **11**, p780, 1880.

[18]Hamann, S.D., Rvw. Phys. Chem. of Japan, **50**, p147, 1980.

[19]Srinivasan R., and Srinivasan, K., J. Phys. Chem. Solids, **33**, p1079, 1971

[20]Woods, A.D.B, Cochran,W., Brockhouse,B.N., Phys. Rev., **119**, p980, 1960.

[21]Zhang, Q.M., Zhao, J., Shrout, T., Kim, N., Cross, L.E., Newnham, Amin, A., and Kulwicki, B.M., J. Ap. Phys., **77**, p2549, 1995.

[22]Uchino, K., Oh, K.Y., J. Am. Ceram. Soc., **74**, p1131, 1991.

[23]Nakajima, Y., Hayashi, T., Hayashi, I., Uchino, K., Jpn. J. Appl. Phys., **24**, p235, 1985.

[24]Nomura, S., Tonooka, K., Kuwata, J., Cross, L.E., Newnham, R.E., Proc. 2nd Mtg. on Ferroelectric Matrls. and Applications, Kyoto, p133, 1979.

[25] Sundar, V., Newnham, R.E., Ferroelectrics, **135**, p31, 1992.

[26]Cady, W.G., in "International Critical Tables", **6**, p207, 1929

[27]Elhamy, K., Gauthier-Manuel, B., Manceau, J.F., Bastien, F., J. App. Phys., **77**, p3987, 1995.
[28]Burkard, H., Kanzig, W., Rossinelli, M., Helvetica Physica Acta, **49**, p12, 1976
[29]Legg, G.J., Lanchester, P.C., J.Phys. C, Sol. State Phys., **13**, p6547, 1980.
[30]Osterberg, H., and Cookson, Rev. Sci. Instrum., **6**, p347, 1935.
[31]Luymes,B.J. , Rev. Sci. Instrum., **54**, p90, 1983.
[32]van Sterkenburg, S.W.P., J. Phys D., App. Phys., **25**, p996, 1992.
[33]Li, J-F, Moses,P., Viehland, D., Rev. Sci. Instrum., **65**, p1089, 1994.
[34]Su, J., Zhang,Q.M., Kim, C.H., Ting, R.Y., Capps, R., in print, J. Appl. Polym. Sci.,1997.
[35]Juretschke, H.J., Am. Jl. Phys., **45**, p277, 1977.
[36]Bohaty, L., Hassuhl, S., Acta Cryst., **A 33**, p114, 1977
[37]Balakrishnan, G., Srinivasan, K., Srinivasan, G., J. App. Phys., **54**, p2875, 1983
[38]Meng, Z.Y., Sun, Y.M., Cross, L.E., Mater. Letters, **2**, p544, 1984
[39]Hruska, C.K., Brendel, R., J. Appl. Phys., **67**, p1676, 1990.
[40]Kittinger, E., Tichy, J., Freidel, W., J. Appl. Phys., **60**, p1465, 1986.
[41]von Hippel, A.R., Dielectrics and Waves, John Wiley & Sons, New York, NY, 1956.
[42]Shanker, J, Dixit, S., Phys. Stat. Sol. (a), **123**, p17, 1991.
[43]Bogardus, E.H., J. Appl. Phys., **36**, p2504, 1965.
[44]Vedam, K., Davis,T.A., J. Appl. Phys., **33**, p4555, 1967.
[45]Rittenmyer, K., Ph.D. Thesis, Pennsylvania State University, Univ. Park, PA 1984.
[46]Vedam, K., Schmidt, E.D.D. , Kirk, J.L. , Schneider,W.C.,Mat. Res. Bull., **4**, p573, 1969.
[47]Vedam, K., Schmidt, E.D.D. , Phys. Rev., v146, p548, 1966.
[48]Sundar, V., Newnham, R.E. , J. Mat. Sci. Lett., **13**, p799, 1994.
[49]Wang, H., Zhang, Q.M., Cross, L.E., Ting, R., Coughlin, C., Rittenmyer, K., Proc. Int. Symp. Appl. Ferroelectrics, **9**, p182, 1994.
[50]Su, J., Zhang, Q.M., , in print, Appl. Phys. Lett., 1997.

APPENDIX 80

Pergamon

Materials Research Bulletin, Vol. 33, No. 9, pp. 1307–1314, 1998

0025-5408/98 $19.00 + .00

PII S0025-5408(98)00125-1

STRUCTURE–PROPERTY RELATIONSHIPS IN THE ELECTROSTRICTION RESPONSE OF LOW DIELECTRIC PERMITTIVITY SILICATE GLASSES

V. Sundar[1,2]*, R. Yimnirun[1]*, B.G. Aitken[3], and R.E. Newnham[1]
[1]IMRL, The Pennsylvania State University, University Park, PA 16802 USA
[2]Ceramco, Burlington, NJ 08016 USA
[3]Corning Inc., Corning, NY 14831 USA

(Refereed)
(Received February 9, 1998; Accepted February 18, 1998)

ABSTRACT

Some of the polarization mechanisms that affect the dielectric and electrostrictive responses of low dielectric permittivity glasses are examined in this work. Electrostriction is the basic electromechanical coupling mechanism in all insulators. It is defined as $x_{ij} = Q_{ijkl}P_kP_l$, where x_{ij} is the strain tensor, Q_{ijkl} the electrostriction tensor, and P_k the induced polarization. The electrostriction constant Q_{11} (in Voigt notation) for glasses containing sodium was found to decrease with frequency in the range 0.1–10 kHz. Q_{11} decreased with frequency from 0.95 to 0.55 m^4/C^2 for sodium trisilicate glass and from 0.6 to 0.45 m^4/C^2 for sodium aluminosilicate glass. In contrast, the Q_{11} for two samples of silica glass remained nearly constant at ~0.4 m^4/C^2 in this frequency range. The role played by the Na^+ ion and that of silicate coordination shells in effecting the different electrostrictive responses of these glasses was analyzed. © *1998 Elsevier Science Ltd*

KEYWORDS: A. glasses, D. dielectric properties

INTRODUCTION

The basic mechanisms contributing to the polarization in dielectric materials have been identified and treated extensively [1]. Their individual contributions are illustrated by the

*Corresponding authors: Dr. V. Sundar, Ceramco, Six Terri Lane, Burlington, NJ 08016, and Dr. R. Yimnirun, 245 Materials Research Lab, Penn State University, University Park, PA 16802. Reprint requests should be sent to Dr. Yimnirun.

frequency dispersion of the linear dielectric response, which separates the contributions from the different mechanisms. Space charge effects and defects contribute to interfacial polarization, which typically has a frequency regime of 10^5 Hz and below. Orientation or dipolar polarization may be seen in the range 10^5–10^{10} Hz in materials that have permanent dipoles. Ionic or atomic polarization occurs in the range 10^{10}–10^{13} Hz, due to the relative displacement of the ions in the material. Electronic polarization arises from the distortions of the charge distributions around the ions of the material, in the optical frequency range of 10^{14} Hz and above.

Electrostriction is a polarization-related effect defined as $x_{ij} = Q_{ijkl}P_kP_l$. An understanding of the mechanisms of polarization that contribute to electrostrictive strain is of fundamental interest. Of the mechanisms outlined above, the effects of the ionic and electronic contributions are of primary concern. The separation of the contributions arising from these effects offers further insight into the underlying mechanisms and is useful in discerning trends in the electrostrictive behavior, especially in low-permittivity linear dielectrics.

Electrostriction measurements on most crystalline materials have been performed only over limited frequency ranges (10^5 Hz and below) [2]. Little variation of the Q coefficients with the frequency of measurement is seen for most crystalline ionic solids. Measurements over wider ranges of frequencies may be necessary to directly study the frequency dependence of electrostriction. However, by choosing materials and methods carefully, it may be possible to gain more insight into the contributions of polarization to electrostriction.

The amorphous structure and metastability in glasses make them interesting for study. Random but continuous networks of $(SiO_4)^{4-}$ tetrahedra make up the basic silica glass structure. Some silicate glasses show dielectric relaxations in the 10 Hz to10 kHz frequency range. The effects of ion vibrations and the silicate "cage" structures can affect the electrostrictive response of these materials.

In this study, the contribution of polarization mechanisms to electrostriction was examined. The effect of Na^+ ion response to electric fields was analyzed for four different glasses: two silicate glasses and two silica glasses. The dielectric and electrostrictive properties of these glasses were measured at various frequencies and are discussed in this article.

EXPERIMENTAL

Glass Samples. Sodium trisilicate ($Na_2O{\cdot}3SiO_2$) and sodium aluminosilicate glass samples obtained from the R&D Division of Corning Glass Works were the two silicate glasses studied. For comparison, a sample of Corning 7940 silica glass and a sample of fused silica (General Electric) were used for measurements. The samples were in the form of disks 22–25 mm in diameter and 1.5–3.2 mm in thickness, polished to an optical finish. Aluminum electrodes were evaporated onto these samples. Guard gaps 0.1 mm wide and 16–17 mm in diameter were scribed on the low electrodes. The compositions of the glasses are given in Table 1.

Electrostriction Measurements. A General Radio 1621 capacitance bridge with a resolution of 0.1 aF (10^{-19} F) in capacitance was used to measure the dielectric and electrostrictive properties of the glasses. The compressometer cell shown schematically in Figure 1 was used for electrostriction measurements.

The compressometer is designed for the application of a homogeneous pressure on the

TABLE 1
Compositions of Glasses Studied, in wt%

Glass	SiO_2	Al_2O_3	Na_2O	Other
Trisilicate	74.4	0	25.6	0
Aluminosilicate	65	25	10	0
Corning 7940	99.9	0	0	0.1% H_2O
Fused silica	98–99	0	0	~1% CaO

Source: refs. 3 and 4.

sample surface from a completely uniaxial loading with tilt and thrust bearings in the load line. The error in load measurement is less than 0.5%. The dielectric susceptibility changes linearly with applied stress, and inhomogenieties in applied stress are averaged out by a comparatively large sample diameter and further diluted by the linear relationship. The thermal mass of the compression jig is large enough to smooth out minor drifts in ambient temperature. The drift in the fractional change in capacitance is less than 3 ppm/min. under quiet conditions.

The electrical stability of the system is also of a high order. The capacitance of the sample holder itself is less than 20 aF. Care is taken to ensure that the only capacitance path is through the sample itself, and all signal leads are coaxial and electrically guarded. The capacitance measurements were carried out in a 3-terminal mode using a General Radio 1621 Capacitance Measurement System capable of measuring down to 0.1 aF. The capacitance resolution with this system is on the whole better than 1 ppm, and the resolution in change in capacitance is less than 2 aF, even as estimated in a worst case analysis. This system is a powerful technique to establish the signs and magnitudes of the electrostriction constants of even low permittivity, low Q value materials.

RESULTS AND DISCUSSION

Dielectric Properties. A plot of the real and imaginary parts of the dielectric constant for the sodium aluminosilicate glass is shown in Figure 2. At low frequencies, the real part is expected to approach a fairly constant value, K_0. However, interfacial (electrode) polarization effects can dominate at frequencies of 40 Hz and below. To eliminate this, the inverse dielectric constants G′ and G″ are plotted as a function of frequency. The inverse dielectric constants are defined by $G^* = 1/K^* = 1/(K' - iK'') = G' + iG''$. As may be seen in Figure 3, the G″ vs. frequency plots show a peak maximum at about 100 Hz for both glasses. This

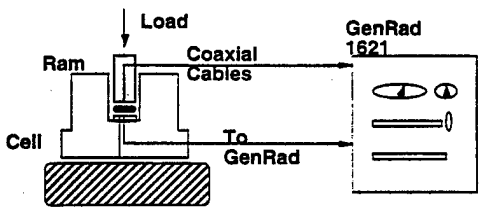

FIG. 1
Schematic of compressometer cell design.

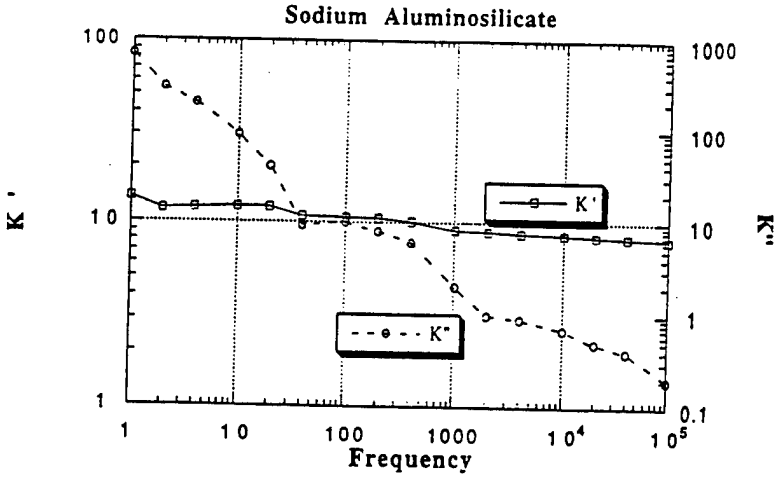

FIG. 2
Real and imaginary parts of the dielectric permittivity of sodium aluminosilicate glass.

is an ionic relaxation peak arising from Na^- ion movements in the various silicate cages. The peak is too broad to be a single dipole relaxation and is also asymmetric with respect to the peak maximum. In contrast, the dielectric constants of the Corning 7940 glass ($\epsilon_r = 3.842$) and the fused silica ($\epsilon_r = 3.861$) are constant in the frequency range 10 Hz to 10 kHz.

Typically, glasses show loss curves as shown in Figure 4. Curve A shows the overall loss vs. frequency plot. Losses arising from dc conduction losses (B), localized conduction (C), vibration of heavy ions (D), and IR vibration modes (E) are possible. The mechanisms postulated to be associated with these loss curves are illustrated in Figure 5.

The dc conduction by alkali ions moving through the silicate channels is a common

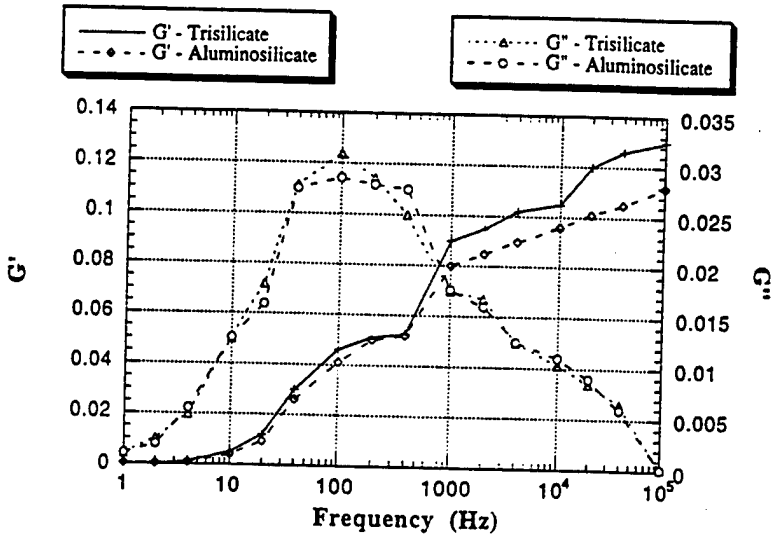

FIG. 3
G′ and G″ as functions of frequency for sodium trisilicate and aluminosilicate glasses.

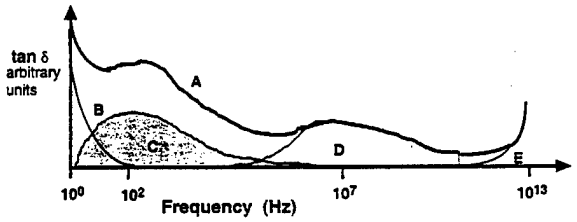

FIG. 4
Dielectric loss in glasses.

low-frequency loss mechanism in the 1–100 Hz frequency range. Localized conduction is associated with space charge effects in the $1–10^5$ Hz frequency range, which is the range of interest in this study. Alkali ions can move by "hopping" between positions in network coordination shells.

Losses associated with the vibrations of heavy ions such as Ba^{2+} or Pb^{2-} against the network cages are observed at even higher frequencies, centered around 107 Hz. Infrared frequency vibration modes of the silicate groups themselves contribute to losses at 10^{10} Hz and above. The trisilicate and aluminosilicate glasses do not have any such heavy ions in them. Thus, the resonance effects seen are most likely due to the localized movement of alkali ions. This behavior of the alkali ions was also seen to affect the variation of the Q coefficients with frequency.

Electrostriction Results. For parallel plate capacitors such as the disks used in this study, the capacitance, C, is given by the following equation, where A is the area of the sample and t its thickness.

$$C = \varepsilon_0 \varepsilon_r A/t$$

The change of permittivity with uniaxial applied stress X is related to both the change in capacitance and the capacitance change, Σ, due to geometric deformation under stress.

$$d\ln\varepsilon_r/dX = (C^{-1}dC/dX - \Sigma)$$

where Σ is given by $\Sigma = -(s_{11} - 2s_{12}) = (1/9\ K - 2/3\ \mu)$ for isotropic glasses. The bulk modulus, K, and the shear modulus, μ, are of the order of 10^8 N/m^2 for these glasses. Elastic data were taken from Karapetyan et al. [5].

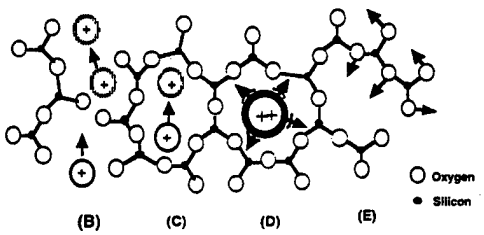

FIG. 5
Mechanisms associated with dielectric loss in glasses. B: dc conduction losses, C: localized conduction, D: vibration of heavy ions, and E: IR vibration modes.

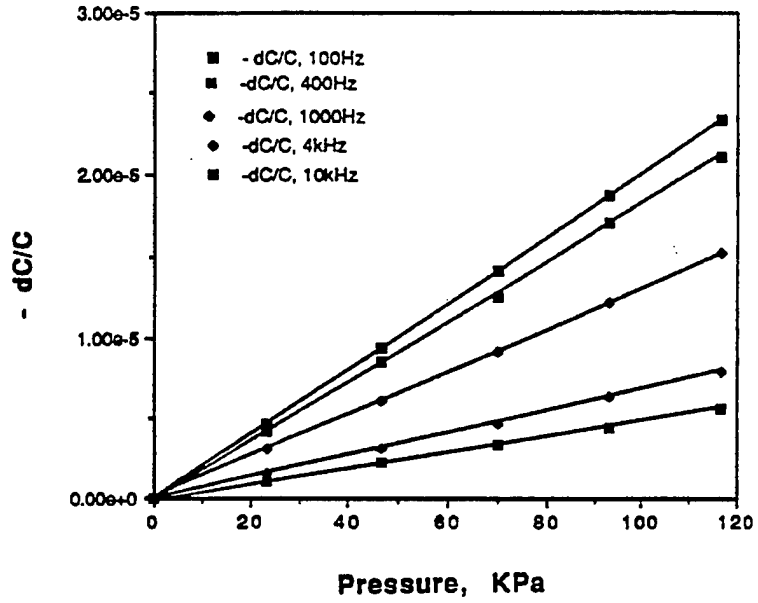

(a)

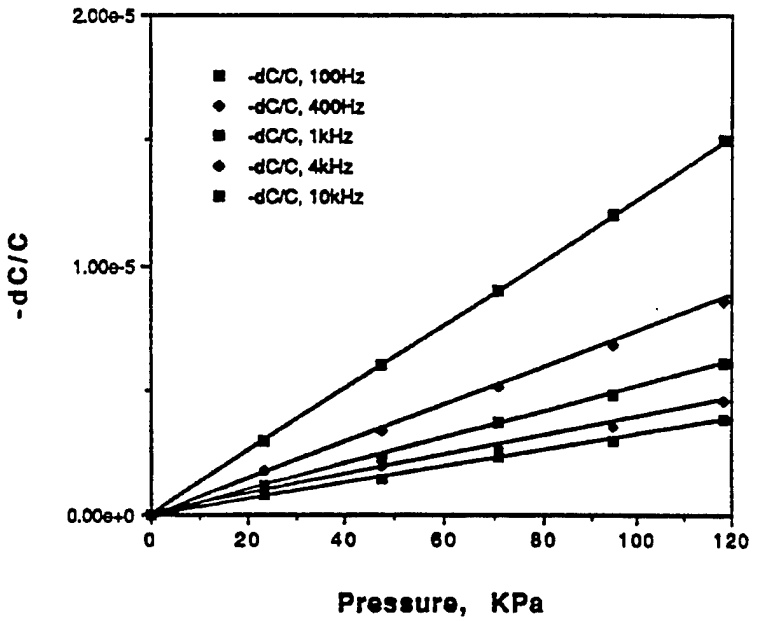

(b)

FIG. 6

(a) Variation of fractional capacitance with stress for sodium trisilicate glass for frequencies from 100 Hz to 10 kHz. (b) Variation of fractional capacitance with stress for sodium aluminosilicate glass for frequencies from 100 Hz to 10 kHz.

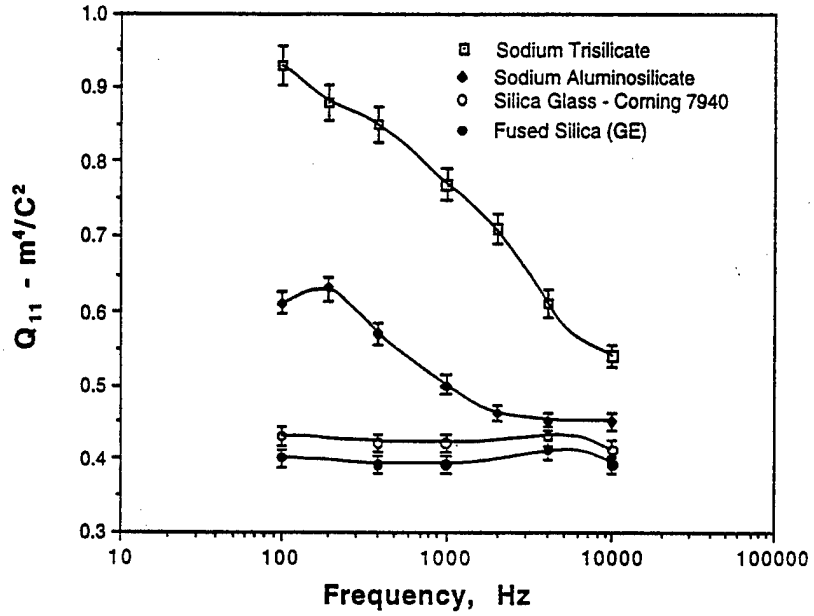

FIG. 7
Variation of electrostriction coefficients Q_{11} with frequency for four glasses, 0.1–10 kHz.

The fractional change in capacitance $\Delta C/C$ was plotted as a function of stress to measure electrostriction. The results for the sodium trisilicate and sodium aluminosilicate glasses are shown in Figures 6a and 6b, respectively.

Corrections were made for the change in capacitance due to the elastic shape change of the samples. A typical correction for sodium trisilicate glass is given as an example as follows: At 1 kHz, $\epsilon_r = 11.3$, $K = 365 \times 10^8$ N/m^2 and $\mu = 252 \times 10^8$ N/m^2. This gives a fractional change in permittivity with applied stress of -2.339×10^{-11} m^2/N. $C^{-1}dC/dX$ is 10.4×10^{-11} m^2/N for sodium trisilicate glass at 1 kHz. It is very important to correct for geometric changes in capacitance for glasses and other low-permittivity materials.

Q_{11} vs. frequency plots are shown for all four glasses in Figure 7. The Q value for the trisilicate glass was within 5% of that obtained by Meng et al. [3]. The fused silica and Corning 7940 silica glass samples showed a fairly constant Q_{11} vs. frequency trend in the 100–10,000 Hz range. The Q_{11} value at 100 Hz for the Corning 7940 glass sample was 0.44 m^4/C^2 and for the fused silica sample 0.38 m^4/C^2. The Q values for these silica glasses represent the electrostrictive response of the unmodified silicate network.

For the sodium trisilicate and aluminosilicate glass samples, the largest observed values of Q_{11} occurred at 100 Hz, where the ionic relaxation was observed. Q_{11} decreased with frequency from 0.95 to 0.55 m^4/C^2 for the sodium trisilicate glass sample and from 0.6 to 0.45 m^4/C^2 for the sodium aluminosilicate glass sample. This reflects the decreasing response of the Na^+ ion oscillations with increasing frequency. Around 10^5 Hz, the Q_{11} values for both silicate glasses tended toward the values for the silica glasses. It can safely be inferred that the Na^+ ion polarizability caused the larger (nearly doubled at 100 Hz) electrostrictive response of the sodium trisilicate glass sample, compared to that of the silica glass samples.

The Q values of the aluminosilicate glass were smaller than those of the trisilicate glass at all frequencies. The extra oxygen introduced by Na_2O is nonbridging in the sodium trisilicate structure. Sodium aluminosilicate glass has far fewer nonbridging oxygen atoms than trisilicate glass. A reduction in the nonbridging oxygen content causes an expansion in the silicate network coordination shell around the Na^- ion. This change in volume may be electrostatic in origin [6]. An expanded silicate cage around the Na^- ion in the aluminosilicate glass is distorted less by the Na^+ ion "hopping" in response to electric fields. Under these circumstances, the Na^- ion polarizability contributes less strongly to the total electrostriction for these glasses.

The contributions of Na^+ and other network modifiers to electrostriction are apparently very important for glasses. Studies on a wider variety of glasses such as borates or phosphates may reveal additional trends in their electrostrictive responses.

CONCLUSIONS

By choosing appropriate materials and methods, it is possible to analyze the ionic polarization contribution to electrostriction in low-permittivity dielectrics. Measurements on four glasses show that the "hopping" of alkali ions inside network cages has a significant effect on electrostriction at low frequencies. With increasing frequency, the effect of this localized conduction mechanism decreases. The network cage also has a significant effect on the electrostrictive response.

ACKNOWLEDGMENTS

The authors would thank Drs. K. Vedam, L.E. Cross, and K. Uchino of the IMRL, Penn State for useful discussions and suggestions. This study was sponsored by the National Science Foundation through contract DMR 9634101.

REFERENCES

1. A.R. Von Hippel, *Dielectrics and Waves*, Wiley & Sons, New York (1956).
2. V. Sundar and R.E. Newnham, *Ferroelectrics* **135**, 431 (1992).
3. Z.Y. Meng, Y.M. Sun, and L.E. Cross, *Mater. Lett.* **4**, 5329 (1988).
4. D.C. Boyd and D.A. Thompson, in *Kirk-Othmer Encyclopedia of Chemical Technology*, Vol. 11, p. 807, Wiley, New York (1980).
5. G.O. Karapetyan, Y.V. Lifshitz, and D.G. Tennison, *Sov. J. Glass Phys. Chem.* **7**, 131 (1981).
6. J.O. Isard, *Trans. Soc. Glass Tech.* **43**, 113 (1959).